University of Heidelberg
Department of Physics and Astronomy

FLUENCE-BASED DOSIMETRY

USING FLUORESCENT NUCLEAR TRACK DETECTORS

MASTER'S THESIS IN
EXPERIMENTAL PHYSICS

carried out by
Grischa M. Klimpki

at the
German Cancer Research Center

under the supervision of
Prof. Dr. Oliver Jäkel
Prof. Dr. Peter Bachert

— August 2014 —

Fluence-based dosimetry using fluorescent nuclear track detectors

Carbon ion radiotherapy offers conformal dose coverage of deep-seated tumors and an enhanced radiobiological effectiveness compared to conventional photon treatment. Since the clinical outcome depends on both energy deposition and particle field composition, spectroscopic beam information is imperative for treatment planning and verification. Current fluence-based dosimeters have the potential to measure required quantities, but because of their size and electronic components, the majority of them is not suitable for *in vivo* applications.

Fluorescent nuclear track detectors (FNTDs) are small and biocompatible aluminum oxide plates. Their superior spatial resolution allows for track-by-track characterization of heavy charged particle fields at clinically relevant fluences. Thus, their fluence-based dosimetry performance has been investigated within this thesis.

Fluence assessment in multidirectional fields was realized by ion track reconstruction through the detector volume. The angular distribution could be measured accurately within 2° uncertainty. This translated into less than 5% overall fluence deviation from the chosen irradiation reference. Combination of this novel routine with an improved energy loss calibration curve based on 90 FNTD irradiations enabled fluence-based dose determination for mixed heavy ion fields. The analysis of a detector irradiated in Bragg peak proximity of a $270\,\mathrm{MeV/u}$ carbon ion field resulted in 85% dose agreement with treatment planning software prediction.

Fluenzbasierte Dosimetrie mit fluoreszierenden Kernspurdetektoren

Die Strahlentherapie mit Kohlenstoffionen ermöglicht eine hochpräzise Dosisabdeckung von tief liegenden Tumoren und bietet zusätzlich eine erhöhte biologische Wirksamkeit im Vergleich zu konventioneller Photonentherapie. Da das Behandlungsergebnis sowohl von der Energiedeposition als auch von der Zusammensetzung des Teilchenfeldes abhängt, sind spektroskopische Strahlinformationen unerlässlich für Therapieplanung und Verifikation. Gängige fluenzbasierte Dosimeter können die geforderten Größen zwar messen, eignen sich aufgrund ihrer Größe und Elektronik jedoch kaum für *in vivo* Anwendungen.

Fluoreszierende Kernspurdetektoren (FNTDs) sind kleine, biokompatible Aluminiumoxidplättchen. Ihre hohe Ortsauflösung schafft die Voraussetzungen dafür, Schwerionenfeldern klinischer Fluenzen anhand einzelner detektierter Teilchenspuren zu charakterisieren. Deshalb wurde innerhalb dieser Arbeit die Leistungsfähigkeit von FNTDs bezüglich fluenzbasierter Dosimetrie untersucht.

Die Fluenz multidirektionaler Felder wurde über die rekonstruierten Spurlängen im Detektorvolumen ermittelt. Die Winkelverteilung konnte bis auf 2° genau bestimmt werden. Daraus ergibt sich eine Fluenzabweichung von weniger als 5% von der Bestrahlungsreferenz. Zusammen mit einer verbesserten Kalibration des Energieverlustes anhand von 90 bestrahlten FNTDs eröffnete dies die Möglichkeit, die Dosisdeposition gemischter Schwerionenfelder fluenzbasiert zu berechnen. Die Auswertung eines Detektors, der nahe des Bragg-Peaks eines $270\,\mathrm{MeV/u}$ Kohlenstoffionenfeldes platziert wurde, ergab eine Dosisübereinstimmung von 85% mit dem zugehörigen Bestrahlungsplanungswert.

CONTENTS

APPENDICES

1 INTRODUCTION

Radiotherapy with heavy charged particles offers high dose conformity while having the ability to spare surrounding healthy tissue from undesired and potentially harmful radiation exposure. Especially those deep-seated tumors, which are usually not treated with photons or electrons, can be covered homogeneously with acceptable doses to neighboring organs at risk [1]. Because of their high linear energy transfer (LET) around the Bragg peak, carbon ions can be more effective against hypoxic or locally advanced tumors usually resistant to photon or low-LET proton irradiations [2]. However, this enhanced relative biological effectiveness (RBE) comes at a price: the quantity absorbed dose to water is no longer the essential predictor for clinical outcome [3]. The same physical energy deposition can vary drastically in RBE depending on the particle field composition. Thus, the characterization of carbon ion beams must provide additional spectroscopic information such as energy loss and ion type besides overall particle fluence. This calls for sensitive detectors capable of measuring these quantities in clinical environments and preferably *in vivo*.

Biocompatible fluorescent nuclear track detectors (FNTDs) are promising fluence-based dosimeters. They are cut from single aluminum oxide crystals doped with carbon and magnesium [4] into small rectangular plates and do not require any electronics during irradiation. The formation of color centers in the course of crystal growth enables subsequent trapping of secondary electrons liberated by traversing ions [5]. Triggered radiochromic transformation alters optical crystal properties in close track proximity and yields bright fluorescent features during non-destructive confocal readout [6]. Because of their superior spatial resolution and excellent detection efficiency [7], single particle tracks can be visualized in the detector material. Thus, FNTDs allow for track-by-track investigation of heavy charged particle fields.

This distinctive property can be exploited for the spectroscopic analysis of swift ion beams with clinically relevant fluences. In radiotherapy with carbon ions, information on particle fluence, energy loss and ion type would enable both dose calculation and advanced beam characterization desired to estimate the biological effect. All fluence [7] and LET measurements [5, 8] conducted prior to this thesis were performed in unidirectional, orthogonal and monoenergetic particle fields. In addition to such artificial setups, current correlations between track intensity and LET have been established on a different readout device [5] or face large fluctuations [8]. But since angular offsets of fragments and scattered ions in therapeutically decisive Bragg peak proximity directly translate into a change in detected intensity and number of particles, this thesis investigated fluence-based dosimetry in complex, multidirectional heavy ion fields using fluorescent nuclear track detectors.

For this purpose, detector performance was examined under particle field conditions predominant around the Bragg peak based on the following experiments: (1) A set of conventional FNTDs has been irradiated at the Heidelberg Ion-Beam Therapy Center under various different angles. A novel approach on the characterization of multidirectional fields was developed and validated on this set of detectors (section 4.1). (2) In order to improve LET assessment, 90 background-reduced FNTDs were irradiated with protons, helium, carbon and oxygen ions over the entire accessible energy range (section 4.2). (3) Furthermore, energy loss straggling along single ion trajectories was investigated on the set of background-reduced FNTDs (section 4.3). Analysis results entered into the establishment of a robust LET determination routine for complex heavy ion fields including uncertainty quantification. Ultimately, dosimetry accuracy was tested on a conventional FNTD irradiated just in front of the Bragg peak of a homogeneous carbon ion field (chapter 6).

Fundamental quantities of relevance for the measurements conducted are introduced in chapter 2. Chapter 3 contains a description of Al_2O_3:C,Mg crystals, an overview on the irradiation facility and the confocal microscope as well as an explanation concerning used data acquisition, evaluation software and analysis routines. All experimental setups are outlined in chapter 4. Obtained results (chapter 5) are being discussed at the example of a clinically relevant irradiation in chapter 6, before a final conclusion is drawn in chapter 7.

2 FUNDAMENTAL QUANTITIES

This chapter summarizes and explains necessary background information on the quantities of interest for the conducted study. The ionization of matter by heavy charged particles (HCPs) and the related energy transfer plays a central role in hadron therapy. Different forms of energy loss are being summarized in section 2.1. The particle fluence Φ is introduced in section 2.2. Additional knowledge on the LET of a HCP (section 2.3) allows for energy deposition calculation. The mean energy imparted by ionizing radiation to matter is generally quantified as absorbed dose (section 2.4). Because of their superior spatial resolution, FNTDs can visualize single ion trajectories and their stochastic energy deposition behavior. Thus, the basic principles and models of energy loss straggling are outlined in section 2.5.

2.1 Heavy Charged Particle Interactions in Matter

2.1.1 Ionizing radiation

The International Commission on Radiation Units and Measurements (ICRU) defines ionization as the liberation of one or more electrons in collision of particles with matter [9]. This process can be triggered by charged (e.g. light electrons or heavy ions) and uncharged particles (e.g. photons or neutrons). They either produce ionization in a medium themselves or initiate transformations that then cause ionization or produce ionizing radiation. Incident HCPs transfer a small fraction of their kinetic energy in each electron collision. As they gradually slow down, ionization probability decreases. Excitation (transfer of electrons to higher energy levels) and elastic scattering become the primary process of energy dissipation. Originally ionizing HCPs can, thus, be considered non-ionizing near the end of their range.

2.1.2 Stopping of swift HCPs

Swift HCPs possess kinetic energies E much larger than those of thermal agitation ($E_{th} < 1\,\mathrm{eV}$). Their stopping in matter results from collisions with atomic electrons and target nuclei. Hence, it can be described based on the laws of electromagnetic and strong interaction. The quantity of interest is the linear stopping power S, which considers electromagnetic interactions only. It is defined as the mean energy lost by the charged particle $\mathrm{d}E$ in traversing a distance $\mathrm{d}x$. According to the ICRU [9], S can be written as a sum of three independent components:

$$S = S_{el} + S_{rad} + S_{nuc} = \left(\frac{\mathrm{d}E}{\mathrm{d}x}\right)_{el} + \left(\frac{\mathrm{d}E}{\mathrm{d}x}\right)_{rad} + \left(\frac{\mathrm{d}E}{\mathrm{d}x}\right)_{nuc} \tag{2.1}$$

S_{el} denotes the linear electronic stopping power due to inelastic interactions with atomic electrons. S_{rad}, the linear radiative stopping power, results from emission of bremsstrahlung in the electric fields of atomic nuclei or electrons. The linear nuclear stopping power S_{nuc} originates from elastic Coulomb interactions, in which recoil energy is imparted to atoms. It does not refer to strong nuclear interactions generally being discussed outside of the context of linear stopping power.

The impact parameter b, defined as the perpendicular distance between the projectile's trajectory and a scattering center, is commonly used to differentiate between different forms of electronic and radiative stopping. Their major characteristics are outlined in the following. Additionally, a brief description of nuclear stopping is provided at the end of this section.

inelastic collisions with electrons

Inelastic collisions of incident HCPs with atomic electrons can be distinguished in two different types according to the impact parameter b:

- soft collisions: For impact parameters much greater than the atomic radius ($b >> r_{atom}$), the particle's Coulomb force field distorts the electron cloud of target atoms. As a result, electrons can be excited into higher states or (with less probability) ejected if they occupy outer shells. Furthermore, polarization can occur in liquids and solids. The net kinetic energy transferred is very small ($\sim 1\,\mathrm{eV}$). But because large impact parameters hold for most interactions, soft collisions account for approximately 50% [10] of the total energy loss and give rise to a continuous slowing down of traversing ions.

- hard collisions: For impact parameters in the order of the atomic dimension ($b \sim r_{atom}$), HCPs will primarily interact with single bound atomic electrons. A substantial amount of kinetic energy can be transfered in knock-on collisions. The ejection of inner-shell electrons ionizes and excites target atoms simultaneously. Characteristic X-rays and/or Auger electrons are emitted. Although hard collisions have a much smaller probability compared to soft collisions, they account for a comparable total energy loss [10].

Both kinds of inelastic collisions with electrons can be described analytically by the Bethe-Bloch equation [11]. The linear electronic stopping power depends on the electron density n_e and the mean excitation energy I of the target material as well as the projectile charge Z and its relativistic velocity β:

$$\left(\frac{\mathrm{d}E}{\mathrm{d}x}\right)_{el} = -K\frac{n_e Z^2}{\beta^2}L(\beta, I) \qquad (2.2)$$
$$\text{with } K = 51\,\mathrm{MeV\,fm^2}$$

The leading term $L_0(\beta, I)$ of the stopping number $L(\beta, I)$ causes the relativistic rise of S_{el} for high projectile velocities β, since

$$L_0(\beta, I) \cong \ln\left(\frac{2m_e c^2\beta^2}{I(1-\beta^2)}\right) - \beta^2 - \frac{C}{Z} - \frac{\delta}{2}. \qquad (2.3)$$

The shell correction C/Z has a significant contribution to $L_0(\beta, I)$, when the particle velocity is of the order of the bound electron velocities. The assumption of atomic electrons at rest breaks down and capture processes have an increased probability. The density-effect correction $\delta/2$ considers the density-dependent polarization of the target. At high velocities, polarization shields the electrical field far from the particle path cutting off its long-range contribution and, hence, decreasing S_{el}. Further correction factors can be added to $L_0(\beta, I)$, e.g. Barkas $ZL_1(\beta)$ and Bloch correction $Z^2L_2(\beta)$ [11].

The Bethe-Bloch equation (2.2) states that the linear electronic stopping power increases with decreasing velocity accelerating the stopping of ions in matter. HCPs, therefore, show a drastic decline in velocity as well as a drastic rise in S_{el} at the very end of their track. This effect is compensated around $\beta \sim 0$ by charge screening. Z will drop down to zero just before HCPs come to rest. Projectiles with $Z > 1$ will gradually bind atomic electrons along their trajectory leading to a decreased effective charge. Z_{eff} can be quantified by the electronic stopping power ratio

$$Z_{eff}^2 = \left(\frac{\mathrm{d}E}{\mathrm{d}x}\right)_{el}^{Z>1} \Bigg/ \left(\frac{\mathrm{d}E}{\mathrm{d}x}\right)_{el}^{Z=1} \qquad (2.4)$$

at the same velocity β. The combination of $S_{el} \propto \beta^{-2}$ and $Z \longrightarrow Z_{eff}$ yields the characteristic Bragg peak.

Inelastic collisions with electrons are of particular importance for all conducted measurements, since the detection principle of FNTDs is based on secondary electron trapping. Liberated charges trigger radiochromic transformation of the crystal in close track core proximity. This process enables the visualization of single ion trajectories and the direct measurement of S_{el}.

elastic collisions with electrons

In elastic collisions with atomic electrons, energy and momentum are conserved. Thus, the energy transfer is typically less than the lowest excitation potential of bound electrons. Such collisions only occur for low-energy incident electrons ($E < 100\,\mathrm{eV}$) with large impact parameters ($b >> r_{atom}$) [12]. Therefore, their contribution to the stopping of HCPs in matter can be neglected.

inelastic collisions with nuclei

For very small impact parameters ($b << r_{atom}$), incident particles can encounter electromagnetic interactions with a target nucleus. If they are inelastic, charged particles are most likely deflected in the Coulomb field of the nucleus under emittance of bremsstrahlung. The probability of nuclear excitation is generally much smaller. The corresponding linear stopping power S_{rad} depends on the following projectile parameters:

$$\left(\frac{\mathrm{d}E}{\mathrm{d}x}\right)_{rad} \propto \frac{Z^2 E}{m^2} \tag{2.5}$$

Since the radiative contribution to the total linear stopping power decreases quadratically with increasing mass m, it is negligible for protons and heavier ions at clinical energies. This kind of interaction is most important for comparably light incident electrons.

elastic collisions with nuclei

Elastic collisions with atomic nuclei, in which incident particles are deflected without emitting radiation or exciting the nucleus, have a minor contribution to S when considering HCPs. The recoil energy imparted to atoms conserves momentum and yields projectile deflection. Although the energy transfer S_{nuc} is small, elastic collisions with nuclei are the main source for the lateral heavy ion beam spread [3].

2.1.3 Strong nuclear interactions

The previous section shows that stopping processes in thick absorbers are governed by inelastic collisions with atomic electrons for high-energy ions. In contrast to electromagnetic interactions, strong nuclear interactions can result in a complete disintegration of both projectile and target nucleus [3]. For impact parameters b in the order of the nuclear radius r_{nuc}, peripheral collisions are most probable. They yield partial fragmentation commonly described by the abrasion-ablation model [13]. In radiotherapy with carbon ions, fragmentation causes a loss of primary particles and a buildup of lower-Z fragments, mostly forward directed. Although primary ion and secondary fragment velocities are comparable, large range differences occur because of the decreased charge ($S_{el} \propto Z^2$). This causes the characteristic dose tail behind the Bragg peak.

2.2 Particle Fluence

2.2.1 Formal definitions

A fundamental scalar quantity of a radiation field is its particle fluence Φ. The ICRU advises the following areal definition:

$$\Phi_A := \frac{\mathrm{d}N}{\mathrm{d}A}, \tag{2.6}$$

where $\mathrm{d}N$ denotes the total number of particles incident on a sphere of cross-sectional area $\mathrm{d}A$. But since every radiation field has a finite particle density, the infinitesimal definition suffers from statistical fluctuations. Thus, particle fluence must be considered a macroscopic concept with lower $\mathrm{d}A$ limit defined by the graininess of the field itself [14]. Figure 2.1 illustrates the formal ICRU definition.

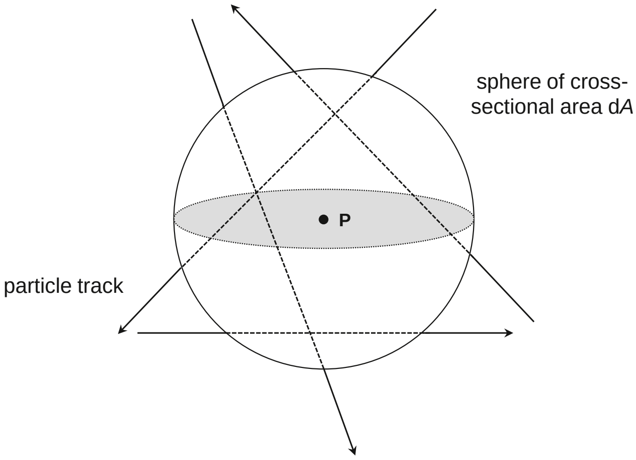

Figure 2.1: *The ICRU formally defines the particle fluence Φ at a point P on an elementary sphere around P with cross-sectional area dA intersected by dN particles.*

Papiez and Battista (1994) proposed a generalized volumetric definition, in which the sum of track length segments $\mathrm{d}\ell_i$ contained within any sampling volume $\mathrm{d}V$ can be used to calculate Φ [15]:

$$\Phi_V := \sum_{i=1}^{N} \frac{\mathrm{d}\ell_i}{\mathrm{d}V}, \tag{2.7}$$

They proved equivalence when considering straight-line trajectories and, in this case, advise against the use of the ICRU definition [16].

2.2.2 Fluence in FNTD measurements

Fluorescent nuclear track detectors described in section 3.1 enable the possibility of measuring both Φ_A and Φ_V of a heavy charged particle field. Confocal sectioning of the crystal explained in section 3.3 yields N_z readout areas separated axially by the step size Δz. The areal ICRU definition of the particle fluence requires counting the total number of ion tracks N intersecting the readout area A and correcting for their polar angle $\vartheta_i \in [0, \pi]$, which is defined as the angle between ion track and z-axis. The azimuthal angle $\varphi_i \in (-\pi, \pi]$ is measured from the x-axis to the orthogonal projection of the ion track on the xy-plane. Both conventions are sketched in figure 2.2 (left).

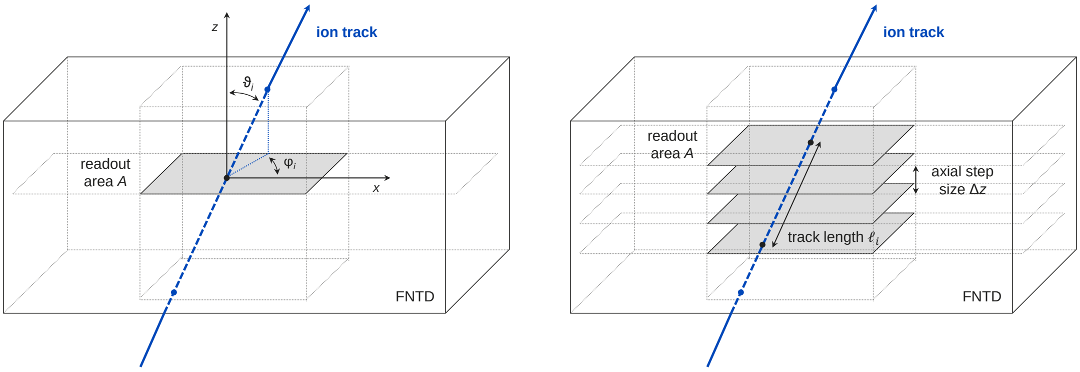

Figure 2.2: *Ion track intersecting the readout area A under the polar angle ϑ_i (left); acquiring multiple image slices in depth enables track length measurements (ℓ_i) in the regarded readout volume V (right); V is determined by the readout area A, the number of image slices N_z and their axial distance Δz*

Since multiple image slices can be obtained along the z-axis, FNTD technology allows for measuring the ion track length ℓ_i in the readout volume $V = A(N_z - 1)\Delta z$ as depicted on the right side of figure 2.2. Mathematically, both approaches result in the same fluence according to [15]:

$$\Phi_A = \sum_{i=1}^{N} \frac{1}{A \cos \vartheta_i} = \sum_{i=1}^{N} \frac{\ell_i}{V} = \Phi_V . \tag{2.8}$$

2.3 Linear Energy Transfer

The ionization density along a particle's trajectory influences its radiobiological impact in hadron therapy [14]. Large amounts of energetic secondary electrons that carry away kinetic energy from the track core diminish the local ionization density. The restricted linear energy transfer L^δ – a predictor of radiation quality

– is, therefore, defined as the difference of linear electronic stopping power S_{el} and the mean sum of the kinetic energies E^{δ}_{kin} in excess of δ of all the electrons released by the charged particle [9]:

$$L^{\delta} := S_{el} - \frac{\mathrm{d}E^{\delta}_{kin}}{\mathrm{d}x}. \tag{2.9}$$

Thus, the restricted LET can be interpreted as that fraction of S_{el}, which includes all soft collisions and those hard collisions resulting in secondary electrons with energies less than δ. The unrestricted LET, denoted as L^{∞} or simply L, is equal to the linear electronic stopping power S_{el} (cf. equation 2.2). FNTDs visualize the LET in Al_2O_3 ($L_{Al_2O_3}$) of individual ion tracks in form of fluorescence intensity (cf. section 3.6).

2.4 Absorbed Dose

2.4.1 Physical dose

The absorbed dose D_{phys} is the most important physical quantity in radiotherapy [3]. It considers all energy deposits ε_i resulting from N single interactions of ionizing radiation in a given volume V of homogeneous density ρ. In order to compensate for statistical fluctuations in energy deposition, the ICRU defined absorbed dose as the mean energy imparted per mass element $\mathrm{d}m = \rho \mathrm{d}V$:

$$D_{phys} := \frac{1}{N} \sum_{i=1}^{N} \frac{\mathrm{d}\varepsilon_i}{\mathrm{d}m} = \frac{1}{\rho} \frac{1}{N} \sum_{i=1}^{N} \frac{\mathrm{d}E_i}{\mathrm{d}x} \frac{\mathrm{d}\ell_i}{\mathrm{d}V} \tag{2.10}$$

For monoenergetic and unidirectional heavy charged particle fields incident on a thin slice of absorber material, this expression simplifies to

$$D_{phys} = \frac{1}{\rho}\, S\, \Phi \cong \frac{1}{\rho}\, L^{\infty}\, \Phi. \tag{2.11}$$

Both equations show a strong material dependency. In radiation therapy, water is used as a tissue-equivalent reference medium. Dose measurements performed with air-filled ionization chambers or alumina-based FNTDs have to be converted using the corresponding stopping power ratios.

2.4.2 Biological dose

In radiotherapy with X-rays, the absorbed dose D_{phys} serves as an estimator of clinical outcome. This attribution is hampered in hadron therapy due to a higher ionization density in the track core. Irradiation plans show enhanced LET distributions in the tumor volume, especially in carbon ion therapy, which can lead to an increased biological effect. In order to transfer knowledge gathered in conventional radiotherapy to hadron therapy, the biological dose D_{biol} is introduced. It can be calculated by applying a quality factor, commonly referred to as relative biological effectiveness (RBE), to D_{phys}:

$$D_{biol} = \mathrm{RBE} \times D_{phys} \tag{2.12}$$

The RBE is formally defined as the ratio of ^{60}Co dose D_γ to ion dose D_{ion} required to achieve the same biological effect ζ_0 (e.g. cell survival or tumor control):

$$\mathrm{RBE} := \left.\frac{D_\gamma}{D_{ion}}\right|_{\zeta=\zeta_0} \tag{2.13}$$

Besides considered biological effect, the RBE depends on dose, particle type and energy as well as target tissue composition. Thus, it differs throughout the entire treatment field calling for careful planning [3]. The local effect model (LEM) [17] enables analytical calculation of the RBE at any position in the radiation field from the parameters Φ, E and Z. It is based on a large set of experimental cell and tissue response data linking biological effects of ion radiation to photon radiation. Ion traversals within the cell nucleus form a microscopic local dose distribution, which determines the calculated effectiveness of particles. LEM is used at HIT for treatment planning.

2.5 Energy Loss Straggling

The electromagnetic interactions of charged particles with electrons and nuclei of target atoms are subject to two sources of fluctuations: The number of collisions and the energy loss in each collision vary statistically following a Poissonian-like behavior. In the theoretical description of energy loss straggling, collisions yielding ionization and secondary electrons are distinguished from collisions where the atomic structure is excited [18]. The number of collisions N_{coll}^{Δ} with low energy transfer is usually estimated by

$$N_{coll}^{\Delta} = K \frac{Z^2 n_e u}{\beta^2 I} \delta x \qquad \text{with } K = 153.5\,\mathrm{MeV}\,{}^{\mathrm{cm}^2}\!/_{\mathrm{g}}. \tag{2.14}$$

The electron density n_e and the mean excitation energy I characterize the target material of thickness δx. u denotes the atomic mass unit. If $N_{coll}^{\Delta} \geq 50$, the number of low energy transfer collisions is considered high compared to the number of collisions resulting in ionization. Thus, a detailed description of the atomic structure may be irrelevant to describe observed energy loss straggling distributions. However, for $N_{coll}^{\Delta} < 50$, the detailed nature of the atomic structure gains importance and needs to be implemented in model calculations.

2.5.1 Landau, Vavilov and Gaussian theory

Three different models can be used to calculate energy loss fluctuations in thin slices if the number of low-energy collision is large ($N^{\Delta}_{coll} \geq 50$) [18]. The κ value distinguishes between the three regimes:

$$\kappa := N^{\Delta}_{coll} I / E^{ion}_{max} \, . \tag{2.15}$$

E^{ion}_{max} is the maximum transferable energy in a single collision with an atomic electron. For heavy ions, it can be approximate by

$$E^{ion}_{max} \cong \frac{2 m_e c^2 \beta^2}{1 - \beta^2} . \tag{2.16}$$

Landau theory ($\kappa < 0.01$) assumes that the typical energy loss is small compared to E^{ion}_{max}. This restriction is removed in the Vavilov theory ($0.01 < \kappa < 10$), which introduces a kinematic limit on E^{ion}_{max}, rather than using $E^{ion}_{max} \longrightarrow \infty$ for $\beta \longrightarrow 1$. It can be shown that the distribution of the Vavilov parameter λ_V approximates the distribution of the Landau parameter λ_L for small κ. For $\kappa \geq 10$, the Vavilov distribution tends to a Gaussian distribution with variance

$$\sigma^2 = N^{\Delta}_{coll} E^{ion}_{max} I \left(1 - \beta^2/2\right) . \tag{2.17}$$

2.5.2 Urbán model

The number of low-energy collisions typically decreases with decreasing material thickness δx. The Urbán model ($N^{\Delta}_{coll} < 50$) provides a method for calculating restricted energy losses with significant secondary electron production. The energy loss distribution approaches the Landau form for $N^{\Delta}_{coll} \longrightarrow 50$ and $\kappa \longrightarrow 0.01$. Based on both macroscopic cross-sections of excitation and ionization, the Urbán model is implemented in the GEANT Monte Carlo algorithm [18].

3 MATERIALS AND METHODS

This chapter outlines and characterizes all measurement principles, device specifications and analysis tools required for data generation, acquisition and evaluation. Fluorescent nuclear track detectors are described in section 3.1. They have been irradiated at the Heidelberg Ion-Beam Therapy Center (HIT) (section 3.2) and read out using a Zeiss LSM 710 ConfoCor 3 confocal microscope (section 3.3). FNTD evaluation involved the use of image and data processing software delineated in section 3.4. Written algorithms concerning fluence and intensity measurements are explained in section 3.5 and 3.6. Data modeling techniques are sketched out in section 3.7.

3.1 Fluorescent Nuclear Track Detectors

Fluorescent nuclear track detectors (FNTDs) have originally been developed for high-capacity volumetric optical data storage at Crystal Growth Division of Landauer Inc. (Stillwater, Oklahoma, USA). They are cut from single aluminum oxide crystals doped with carbon and magnesium (Al_2O_3:C,Mg). High concentrations of enclosed color centers disturb the periodic crystal potential due to local charge imbalances. Valence electrons liberated by traversing particles can be trapped permanently in such color centers triggering radiochromic transformation. FNTDs show excellent detection efficiency of fast neutrons and swift heavy ions [4]. All detectors used in this study were cut along the optical c-axis of the doped alumina crystal into small rectangular plates ($4.0 \times 8.0 \times 0.5\,\text{mm}^3$). One of their large sides was polished to obtain an optically transparent surface.

Figure 3.1: *Fluorescent nuclear track detector (FNTD) in comparison to a one cent coin; crystals are cut in $4 \times 8\,mm^2$ plates of 0.5 mm thickness*

3.1.1 Crystal structure and color centers

Aluminum oxide (α-Al_2O_3) is an inorganic wide-gap dielectric ($E_g = 9.5\,\mathrm{eV}$) with physical density $\rho = 3.98\,\mathrm{g/cm^3}$ [19]. It adopts a trigonal Bravais lattice, in which the oxygen ions form a slightly distorted hexagonal close-packed sublattice. Aluminum ions occupy two out of every three octahedral interstices and are, therefore, surrounded by six nearest-neighbor O^{2-} ions. This is depicted on the left side of figure 3.2.

FNTDs are drawn from the melt in a highly reduced atmosphere using the Czochralski method [20]. Low oxygen partial pressure in combination with carbon doping creates aggregate oxygen vacancy defects denoted as F^{2+} color centers. The majority of these color centers contains one electron (F^+). The remaining charge imbalance of +1 is compensated by a magnesium ion (Mg^{2+}) substituting an aluminum ion (Al^{3+}). Landauer Inc. claims that two one-electron F^+ color centers are always surrounded by two Mg^{2+} ions forming a two-electron $F_2^{2+}(2Mg)$ color center [20] as sketched on the right side of figure 3.2.

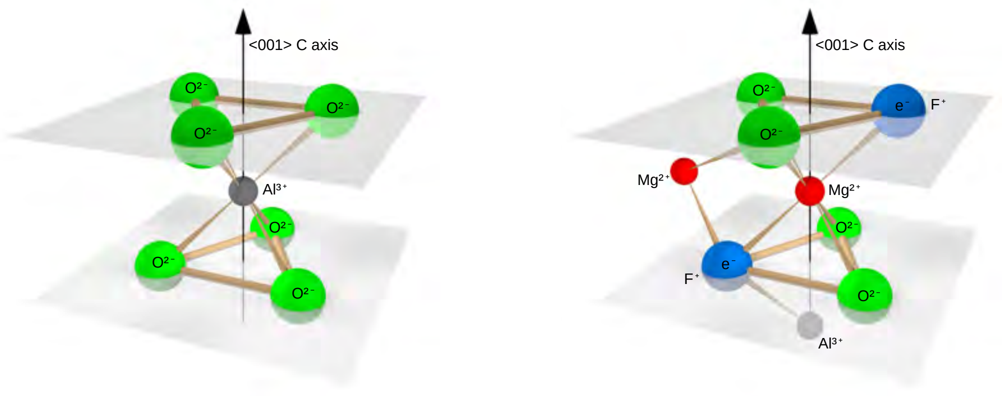

Figure 3.2: *Aluminum oxide crystal structure before (left) and after doping with carbon and magnesium (right); aggregate oxygen vacancy defects lead to the formation of* $F_2^{2+}(2Mg)$ *color centers; reprinted from [21] according to [20]*

3.1.2 Band structure

Heavy charged particles liberate secondary electrons along their track through solid matter. In case of aluminum oxide, the transferred kinetic energy is high enough, to create holes in the valance band and free charges in the conduction band. As color centers form local minima in the crystal potential, they exert an attractive force on liberated secondary electrons. One-electron trapping yields three-electron $F_2^{+}(2Mg)$ color centers:

$$F_2^{2+}(2\mathrm{Mg}) + e^- \longrightarrow F_2^{+}(2\mathrm{Mg}). \tag{3.1}$$

This process changes absorption and emission properties of color centers and slightly raises their ground state energy (cf. figure 3.3).

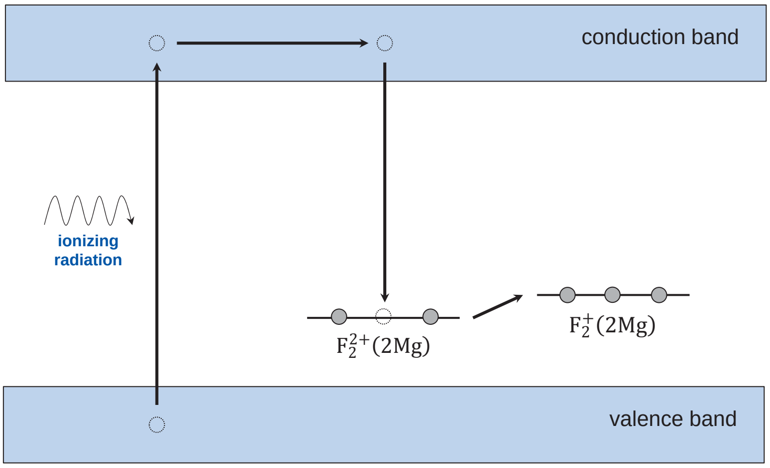

Figure 3.3: *Ionizing radiation can liberate electrons from the valence into the conduction band; when trapped in* $F_2^{2+}(2Mg)$ *color centers, they induce radiochromic transformation yielding an energetically higher state; reproduced according to [19]*

Spectroscopic properties of FNTDs were investigated in [5]. Findings show that transformed $F_2^+(2Mg)$ color centers possess three excited states at 260 nm, 335 nm and 620 nm. They all produce fluorescence at 750 nm under optical excitation with high quantum yield and short lifetime $\tau = (75 \pm 5)$ ns. Untransformed $F_2^{2+}(2Mg)$ color centers, on the other hand, show only one absorption line in the blue at 435 nm. They emit 520 nm photons giving the as-grown crystals their green-yellow coloration. Figure 3.4 depicts these spectroscopic differences and table 3.1 summarizes them quantitatively.

crystal defect	**λ excitation [nm]**	**λ emission [nm]**
F_2	300	500
$F^+(Mg)$	240, 255	325
$F_2^{2+}(2Mg)$	435	510
$F_2^+(2Mg)$	260, 335, 620	750
$F_2^+(Mg)$	350	385

Table 3.1: *Excitation and emission lines of color centers contained in FNTDs; the 620/750 band was used within this study for detector readout; results are reprinted from [5]*

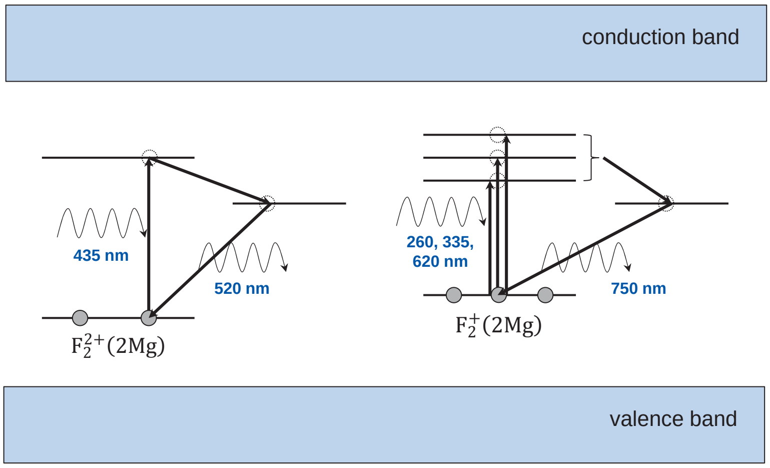

Figure 3.4: *Untransformed $F_2^{2+}(2Mg)$ color centers absorb light with a wavelength of 435 nm and yield 520 nm fluorescence (left); transformed $F_2^{+}(2Mg)$ color centers possess three absorption bands with a short-lifetime fluorescence at 750 nm (right); reproduced according to [19]*

3.1.3 Detector readout

FNTD readout is based on laser-induced fluorescence. Transformed color centers along incident particle tracks appear as bright fluorescent features on dark background when stimulated with a red laser. Because of their superior spatial resolution, FNTDs allow for imaging individual ion tracks by using a confocal laser scanning microscope. Since excited states are still located deep within the band gap, non-destructive detector readout can be repeated multiple times without significant signal loss.

The excitation laser of the confocal microscope is scanned over the focus plane laterally. The acquisition time for $135 \times 135\,\mu m^2$ images is in the order of minutes due to high-yield and short-lifetime fluorescence. Shifting the focal plane in axial direction allows for reconstruction of full 3D track images through the detector volume. The actual diameter of the track penumbra is in the order of several µm (determined by the lateral width of the confocal point spread function). Thus, randomly distributed tracks can be imaged without significant overlap at track densities up to $10^7\,{}^1\!/\!_{cm^2}$.

FNTDs possess a wide-range LET sensitivity demonstrated in [5]. Furthermore, the track detection efficiency for protons and heavy ions lies at nearly 100% [7]. Their potential in terms of fluence-based dosimeters has, therefore, been investigated in this thesis. The methods behind fluence and LET assessment using FNTDs are described in sections 3.5 and 3.6.

3.2 Heidelberg Ion-Beam Therapy Center

The Heidelberg Ion-Beam Therapy Center (HIT) is the first combined treatment facility in Europe offering both protons and carbon ions for radiation therapy [22]. Additionally, helium and oxygen ions can be accelerated to therapeutic energies for experimental purposes. Ion sources are in gaseous state (hydrogen, helium and carbon dioxide). After injection into a linear accelerator, swift heavy charged particles ($7\,{}^{\mathrm{MeV}}\!/\!{}_{\mathrm{u}}$) are fully ionized at a $100\,{}^{\mu\mathrm{g}}\!/\!{}_{\mathrm{cm}^2}$ carbon stripper foil [S. Scheloske, pers. comm., 2014] and coupled into the synchrotron ($\varnothing \cong 20\,\mathrm{m}$). High frequency electric fields achieve a final velocity of up to $\beta = 0.76$. The particle beam is guided to the treatment (or quality assurance) rooms in vacuum tubes and deflected by strong quadrupole magnets. Beam focus is optimized at isocenter – 142.5 cm cm behind the vacuum window [S. Brons, pers. comm., 2014] – and depends on the particle type and its respective energy. Lateral intensity-controlled raster scanning allows for generation of isoenergy slices homogeneous in fluence and dose deposition. 255 ion energies are available for irradiation. Their total range is listed in table 3.2.

ion type	**energy range [$^{\mathrm{MeV}}\!/\!_{\mathrm{u}}$]**	**velocity range [c]**	**water depth range [cm]**
^{1}H	48.12 – 221.06	0.31 – 0.59	2.1 – 30.8
^{4}He	50.57 – 220.51	0.32 – 0.59	2.3 – 30.7
^{12}C	88.83 – 430.10	0.41 – 0.73	2.1 – 30.8
^{16}O	103.77 – 514.82	0.44 – 0.76	2.1 – 30.6

Table 3.2: *Accessible ion energies at HIT for protons as well as helium, carbon and oxygen ions; corresponding penetration depths in water have been calculated with the libamtrack package [23] in R based on the continuous slowing down approximation (CSDA)*

3.3 ZEISS LSM 710 ConfoCor 3

The ZEISS LSM 710 ConfoCor 3 laser scanning microscope [24] was used for FNTD readout in this study. The light microscopy facility at DKFZ provides both LSM hardware and 2012 ZEN (black) control software. The principles of confocal microscopy and LSM 710 characteristics are presented in this section.

3.3.1 Light path, filters and detectors

FNTDs are optically sectioned using confocal laser scanning microscopy (CLSM). Excitation of radiochromically transformed color centers is stimulated with a 633 nm helium-neon laser line (5 mW nominal output power, 100 µW at the sample [25]). As depicted in figure 3.5, the laser beam is laterally deflected using scanning mirrors attached to piezoelectric crystals and then focused onto the specimen by a Plan-Apochromat 63×/1.40 Oil DIC M27 objective lens [26]. An additional motor driven microscope stage allows for axial focal plane shifts and realizes full 3D imaging. 750 nm fluorescence is separated from excitation laser light reflected back with a multi-band beam splitter (MBS488/561/633) and a single longpass emission filter (LP655) [27]. The confocal pinhole arranged in front of the detector unit reduces fluorescence originating from above or below the focal plane and, therefore, limits the axial detection volume. But because of its finite diameter ($43.6\,\mu\text{m} \mathrel{\hat{=}} 1.0\,\text{AU}^1$), an effective slice thickness of δ_z remains. Two fiber-coupled, actively quenched avalanche photo diodes (APDs) detect stimulated fluorescence in photon counting (Geiger) mode. Their quantum efficiency in the red is much higher compared to photomultiplier tubes (PMTs) used to detect laser light transmitted by the specimen. Because of FNTD transparency, these transmission photomultiplier tubes (T-PMTs) allow for online laser power monitoring.

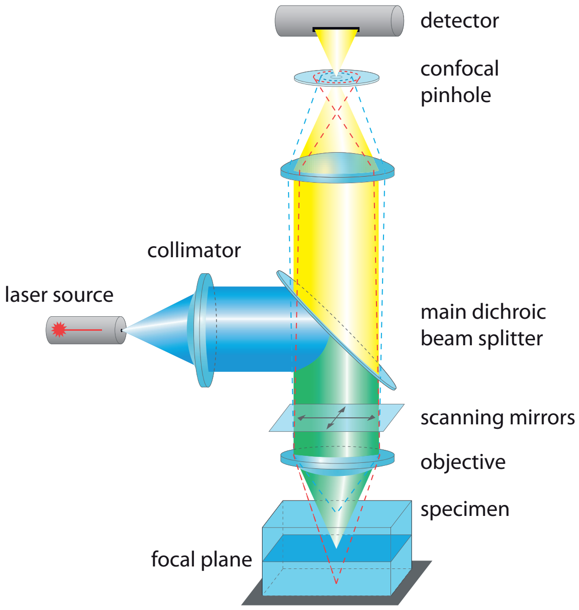

Figure 3.5: *Schematic light path in a confocal laser scanning microscope (CLSM); an objective lens focuses the laser light onto the specimen, where fluorescence is excited; confocal sectioning in combination with lateral scanning enables full 3D image acquisition; fluorescent radiation is directed onto the detector via a dichroic beam splitter blocking the excitation laser line; the confocal pinhole arranged in front of the detector obstructs light rays off focus; reprinted from [27]*

---

[1] 1 AU is defined as the optimal focus spot diameter that a perfect lens with circular aperture can achieve when facing diffraction of light. For a pinhole diameter of 1 AU, an optimized compromise between contrast and intensity is granted concerning the microscope image.

3.3.2 Point spread function

Confocal microscopy is based on illumination and observation of single points. But because of the imaging properties of the optical system, truly point-like objects will appear blurred or spread. This effect is quantitatively described by the point spread function [24] mapping the intensity distribution in image space. Its axial expansion is larger than its lateral one as depicted in the following two PSF sections (figure 3.6). As a result, a single pixel value will hold fluorescence information of an entire volume illuminated by the microscope excitation laser.

Figure 3.6: *Computed sections through a 3D PSF in lateral (left) and axial (right) direction; the central maximum in the lateral section is called Airy disk; its diameter is defined by the greatest core diameter in (x, y)-direction; reprinted from [24]*

3D Gaussian approximation

According to [28], 3D Gaussian approximations of PSFs are "nearly perfect" for confocal laser scanning microscopes with typical pinhole sizes ($\sim 1\,\mathrm{AU}$). The axial decreasing speed is very high, because the PSF is given by a product of excitation and emission PSF:

$$\mathrm{PSF}_{\mathrm{LSM}} = \mathrm{PSF}_{ex} \times \mathrm{PSF}_{em}. \tag{3.2}$$

Calculating the axial and lateral Gaussian parameters for the 3D approximation of $\mathrm{PSF}_{\mathrm{LSM}}$ using the MosaicSuite for ImageJ (see section 3.4.2) based on the analytical model derived in [28] yields:

$$\begin{gathered}\sigma_{lat} = 100.57\,\mathrm{nm} \text{ and } \sigma_{ax} = 365.87\,\mathrm{nm} \\ \text{with an axis ratio of } \varepsilon = \sigma_{ax}/\sigma_{lat} = 3.6.\end{gathered} \tag{3.3}$$

aberrations induced by refractive index mismatch

The refractive index of FNTDs ($n_{FNTD} = 1.76$) is larger than the refractive index of the immersion oil ($n_{oil} = 1.51 \cong n_{dish}$). At the boundary between the media, laser light is partially reflected and partially refracted. The consequences of this refraction have been studied in [29] and can be summarized to:

- The axial focus position (AFP) will be shifted towards larger depths compared to the refraction-free nominal focus position (NFP). Analytical models for the axial scaling factor ASF = AFP/NFP for high-aperture objective lenses are derived in [30]. Concerning FNTD readout between 30 µm and 70 µm depth, a constant ASF of 1.20 was assumed, which is slightly larger than the lower ASF limit of $n_{FNTD}/n_{oil} = 1.17$.
- Integration over all light rays results in an increased confocal observation volume. The PSF is mainly distorted in axial direction and not laterally. But since fluorescence far off focus is blocked by the confocal pinhole, a decreased z-response is observed (cf. figure 3.11). The correction of this intensity loss with readout depth is outlined in section 3.6.4.

3.3.3 Control parameters

control parameter	**functional description**
laser wavelength λ_{ex}	wavelength of the microscope excitation laser
relative laser power p	relative strength of excitation laser during readout
pixel matrix	lateral pixel resolution of one image
image size l_x, l_y	lateral image dimensions in µm
zoom	relative size of centered image section
dwell time τ	illumination duration on one spot
rescans R	number of images to sum up or average over
axial readout range	axial position of the focal plane
axial step size Δz	axial distance between two images in a stack
digital gain g and offset Δg	grayscale variables within ZEN

Table 3.3: *Control parameters of the LSM 710 confocal microscope accessible via ZEN 2012 (black) software; digital gain and offset were kept constant at 0.2 and 0.0, respectively, for all readouts*

During FNTD readout, all detectors were placed in MatTek glass bottom microwell dishes (P35G-1.5-20C). But in contrary to standard procedure, the glass bottom dishes were filled with a thin layer of ZEISS immersion oil Immersol™ 518 F ($n_{oil} = 1.51$) to ensure maximal laser light coupling into the FNTD by reducing refractive index jumps. Confocal microscope settings were controlled via ZEN 2012 (black) software. Table 3.3 outlines the most important parameters and describes their function.

3.3.4 Microscope characterization

relative laser power *p*

Fluctuations of the excitation laser power can be monitored using the built-in T-PMT of the confocal microscope. Figure 3.7 validates that relative T-PMT signal (normalized to the maximum image mean) increases linearly from 1% to 100% with increasing laser power p. Besides, readout of 22 detectors over 16 days shows T-PMT signal variations of approximately 2% on average. Variations are more pronounced, when the relative laser power p was small ($< 20\%$) during readout. The excitation laser strength was, therefore, assumed to be stable for all FNTD readouts.

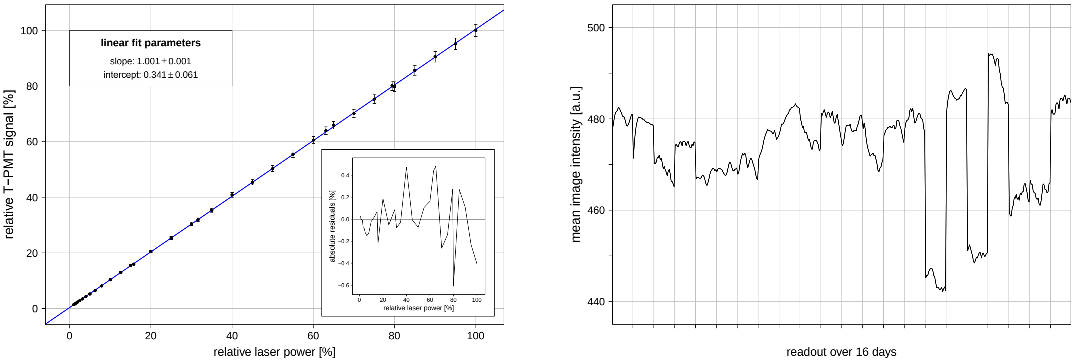

Figure 3.7: *Linear correlation between the relative laser power p and the relative T-PMT signal (image mean) measured on hm2126 with enclosed regression residuals (left); absolute T-PMT signal measured over 16 days during readout of 22 FNTDs separated by vertical gray lines (right)*

Relative laser power correction has to be considered, when reading out FNTDs with different p values because of nonlinearities in track response. Perhaps, an additional triplet state in the band structure is populated when laser excitation is high, yielding a delayed fluorescence and, thus, decreased track intensity. This effect has partly been investigated in [21] for background-reduced FNTDs. The following correction factor f_p was proposed in [31] to normalize chosen laser powers p to a standard reference p_{ref}:

$$f_p = \left(\frac{p}{p_{ref}}\right)^{\xi} \tag{3.4}$$

In order to determine ξ, intensities $I(p_1)$ obtained from readouts with decreased laser power $p_1 < 100\%$ are plotted against the corresponding intensities $I(p_2)$ at full laser power $p_2 = 100\%$. A universal correction factor f_p would yield the following equality:

$$\begin{aligned} f_{p_1}\ p_2\ I(p_1) &= f_{p_2}\ p_1\ I(p_2) \\ \Leftrightarrow \qquad I(p_2) &= p_1^{1-\xi}\ I(p_1) \end{aligned} \tag{3.5}$$

This comparison was carried out for two different irradiations and readouts as depicted in figure 3.8. Fitting the linear relation derived above to both data sets simultaneously yields $\xi = 0.165 \pm 0.002$. The dashed lines represent linear fits performed separately for the two sets of detectors.

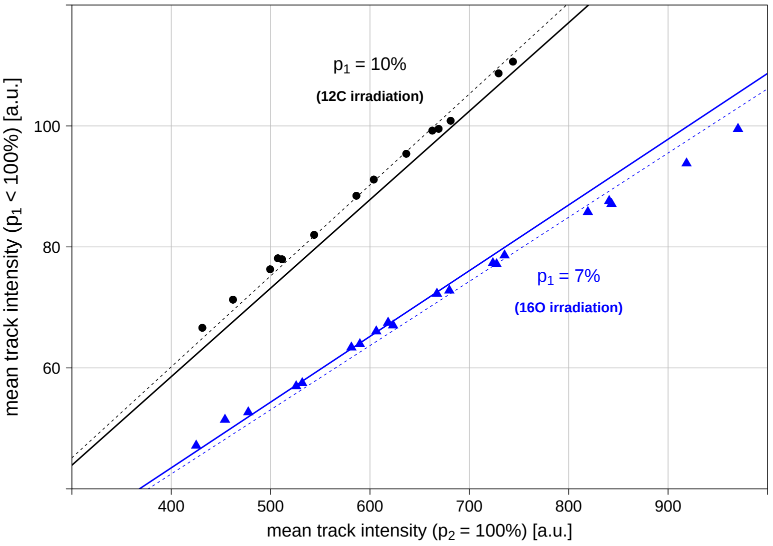

Figure 3.8: *Determination of the laser power correction factor based on two different sets of background-reduced FNTDs: irradiation with* ^{12}C *ions and readout at* $p_1 = 10\%$ *(black dots) vs. irradiation with* ^{16}O *ions and readout at* $p_1 = 7\%$ *(blue triangles); both data sets can be fitted simultaneously (solid lines) to equation 3.5 yielding* $\xi = 0.165 \pm 0.002$*; separate linear regressions (dashed lines) result in* $\xi^{12C}_{10\%} = 0.177$ *and* $\xi^{16O}_{7\%} = 0.157$

The multiplicative factor f_p influences all measured intensities directly. The mean μ and the standard deviation σ of an intensity sample, therefore, scale with f_p. But the laser power correction does not affect relative standard deviations $\sigma_{rel} = \sigma/\mu$.

APD saturation

Two fiber-coupled, actively quenched avalanche photo diodes (APDs) are used in the ConfoCor 3 module to detect color center fluorescence around 750 nm. Since they are operated in photon counting (Geiger) mode with a dead time of 40 ns, APDs show significant saturation at count rates above 1 MHz. This saturation has been quantified in [25]:

$$\eta_{det} = \eta_{max}\left(1 - e^{-\eta_{exp}/\eta_{max}}\right) \quad \text{with } \eta_{max} = (16.2 \pm 1.4)\,\text{MHz}. \tag{3.6}$$

Since this is the first thesis based on FNTD readout in oil, the saturation characteristic was double-checked on a probe irradiated with 150 $^{\text{keV}}/_{\mu\text{m}}$ oxygen ions. The same image was acquired with 34 different laser powers p between 1% and 100% yielding 34 different expected count rates η_{exp} when assuming linearity between η and p. Figure 3.9 confirms results presented in [25] and classifies observed saturation as a pure APD-intrinsic property.

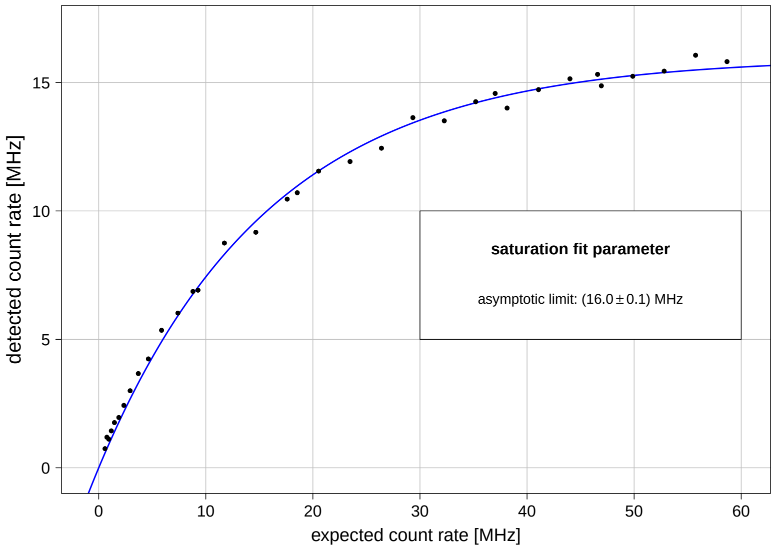

Figure 3.9: *APD saturation measured on hm2126 irradiated with 150* $^{\text{keV}}/_{\mu\text{m}}$ *oxygen ions; the expected count rate was calculated from the corresponding relative laser power; results are in good agreement with previous saturation characterization [25]*

Each pixel value in obtained microscope images holds information on the total photon counts over the dwell time τ. This quantity is denoted as raw intensity I [a.u.]. The photon count rate η [MHz] can be determined when dividing I by τ. The inverse of equation 3.6 was applied pixel by pixel to the detected count rates η_{det} in order to correct for saturation effects directly in the image.

3.4 Data Acquisition and Evaluation

3.4.1 ZEN

The confocal microscope is controlled by the single user interface Zeiss Efficient Navigation (ZEN) [24]. Within ZEN 2012 (black), microscope hardware was controlled adjusting the parameters listed in table 3.3. The free version ZEN 2012 (black) light is able to open acquired .lsm files and retrieve control parameter information stored in the image header. A color depth of 16 bit was chosen preserving the maximum dynamic range (0 to $2^{16} = 65{,}536$ photon counts).

3.4.2 ImageJ and MosaicSuite

Microscope images were imported into ImageJ[2], a public domain Java image processing program [32], and saved in .tiff format. ImageJ can display, edit and process images using a broad variety of customized macros and plugins. The MosaicSuite [33] for ImageJ developed by the MOSAIC Group (formerly ETH Zürich, now MPI-CBG Dresden) was found to be a powerful plugin fulfilling most requirements of FNTD analysis. Frequently used functions embedded in the plugin are described in the following.

background subtractor

The background subtractor is able to reconstruct the inhomogeneous noise level of analyzed FNTDs due to pre-transformed color centers. The total size of bright track objects in the foreground must be small compared to the unirradiated area, since the background subtractor algorithm is histogram-based. A sliding window with adjustable side length l is moved across the image in steps of $l/2$. At every iteration, a histogram of the pixel intensities within the sliding window is generated. The maximum frequency (most abundant pixel value) determines the background at the position of the sliding window center. Bilinear interpolation between the four nearest background intensities fills up the background image. More detailed information can be found under [34].

particle tracker

The particle tracker [35] provides a two-dimensional point-tracking tool, which can be applied to determine the lateral particle positions on orthogonally irradiated FNTDs. Furthermore, the algorithm enables automated computation of particle trajectories as long as the lateral displacement is small between two images in a stack. Point locations are estimated based on local intensity maxima. The linking algorithm minimizes a trajectory cost function considering all identified positions.

---

[2] Author Wayne Rasband is at the Research Service Branch, National Institute of Mental Health, Bethesda, Maryland, USA.

More detailed information on the particle matching algorithm using graph theory technique can be found under [36].

Five important parameters can be adjusted to optimize particle tracking: (1) The track radius in unit of pixels should be slightly larger than the visible particle radius, but always smaller than the smallest inter-particle separation in order to avoid over- and under-detection. (2) The cut-off value determines the score for non-particle discrimination, whereas (3) the percentile [%] defines, which upper image intensities are considered particle candidates. (4) The link range sets the number of subsequent slices for trajectory generation and (5) the displacement restricts the maximum number of laterally traversed pixels between two images in a stack. Obtained trajectory information can be exported as a single .txt file.

Squassh segmentation

Trajectory reconstruction for FNTDs irradiated under arbitrary angles faces the difficulty of object distortion. Particle tracks will no longer appear as round spots but as elongated ellipses with a decreased mean intensity. Since the particle tracker algorithm is optimized for point-tracking, many circular positions will be accounted to one track ellipse yielding a falsely larger fluence. Such images can be analyzed using Squassh segmentation. Pixel values above a specified threshold (minimum object intensity) are identified, clustered and outlined as single regions. The intensity-weighted center of mass determines the lateral position of these objects. The regularization parameter and prior background subtraction help reducing segmentation of noise-induced small intensity peaks. More detailed information on Squassh segmentation are provided under [37].

Object masks and tracking tables can be saved after image stack analysis. Calculation time strongly depends on the number of images per stack and tracks per image. Large fluences can easily exceed several hours of computation. Trajectory generation is achieved by linking object positions throughout the stack with the particle tracker. Additional forces weigh the importance of object position (spatial), shape (feature) and motion (dynamic). Optimized parameters were found to be $(0.01, 6, 6)$[3].

3.4.3 R

Intensity measurements and tracker table analysis were performed in R 3.0.2 [38], a language for statistical computing and graphics. RStudio versions 0.97 and later [39] were used as an integrated development environment. The FNTD package [40]

---

[3] Linking Squassh tables with the particle tracker is a customized enhancement of the MosaicSuite kindly provided by P. Incardona (MPI-CBG Dresden). The forces option was additionally included to improve tracking of elongated ellipses. Stated values are based on optimizations and his tracking experience.

for R features a 2D symmetric Gaussian fit routine that is able to measure the intensities of circular track spots on microscope images directly within RStudio. A more detailed description of this algorithm is given in section 3.6.1. The HITXLM package [41] was used to create irradiation plans requesting ion type, beam energy, focus width, field size and particle fluence from the accelerator unit at HIT. All plots were created with the lattice package [42].

3.4.4 SRIM

Discreet stopping power values in aluminum oxide and water were taken from J.F. Ziegler's and J.P. Biersack's Stopping and Range of Ions in Matter (SRIM). Version 2013.00 is available for download under [43].

3.5 Trajectory Reconstruction

3.5.1 Particle tracking

Particle fluence analysis using FNTDs is based on ion trajectory reconstruction through obtained image stacks. MOSAIC particle tracking introduced in the previous section (3.4) was used to determine the (x, y, z) coordinates for each track spot. Furthermore, it links objects of similar dynamics and shape across image slices to generate a set of ion trajectories. For irradiations with polar angles $\vartheta > 10°$, Squassh image segmentation was used to identify non-circular track objects.

3.5.2 Track selection

High-energetic delta electrons can leave bright signatures in the detector crystal. Although they move on curved paths, they could falsely be registered in the particle tracking stage and linked with true ion tracks. In order to minimize this uncertainty, only tracks visible in at least three image slices were considered in fluence measurements. Squassh segmentation faces the additional difficulty of outlining a large number of small detector background objects. But since the intensity sum over all pixels in these objects is much smaller than the intensity sum in true ion tacks, they can be filtered out by a simple threshold criterion prior to the linking stage.

3.5.3 Linear regression

High-energetic heavy ions will most likely traverse the FNTD on unaltered paths. Thus, trajectory reconstruction can be realized by applying linear regressions on the particle tracker tables. The axial position z was scaled by a factor of 1.2 due to refractive index mismatch during readout (cf. section 3.3.2). The slopes of the lines can then be used to calculate the polar and azimuthal angles, the entrance and exit points, as well as the ion track lengths ℓ. Assuming

$$\begin{gathered} x(z) = m_x z + b_x \text{ and } y(z) = m_y z + b_y \\ \text{with } m_x, m_y > 0 \text{ (w.l.o.g.)} \end{gathered} \tag{3.7}$$

the polar (ϑ) and azimuthal angle (φ) are given by

$$\begin{aligned} \tan\varphi &= m_y/m_x \\ \cos\vartheta &= \left(m_x^2 + m_y^2 + 1\right)^{-1/2} . \end{aligned} \tag{3.8}$$

The full R script on trajectory reconstruction can be found in appendix D.1.

3.5.4 Trajectory filter function

Crossing ion tracks cause errors in the linking stage. Both trajectories could be split up at the point of intersection resulting in four short and not two long trajectories. But since all trajectories are extrapolated to the entire readout volume for fluence calculation, this track splitting yields a locally doubled fluence. Therefore, a filter function was introduced after trajectory reconstruction. It compares all obtained tracks with one another in order to remove duplicates. The full R script on this trajectory filter can be found in appendix D.2. The following criteria are implemented in the algorithm:

- Duplicate candidates cannot be visible in the same image slice.
- Their azimuthal angle ϑ and extrapolated track length L cannot differ significantly.
- They must have the same slopes m_x and m_y within statistical regression uncertainty.
- And they must agree in their x, y, z-positions in the readout volume.

Identified duplicates are grouped in pairs. The track with the fewest entries in the original particle tracker table is eliminated from the reconstructed set of trajectory.

3.5.5 Fluence calculation

volume definition

Calculating the particle fluence via its volumetric definition is achieved by dividing the sum of all trajectory lengths ℓ_i in the reconstructed set by the total readout volume V. The Poisson uncertainty on Φ_V is governed by the total number of analyzed trajectories N_ℓ:

$$\begin{aligned} \Phi_V &= \frac{1}{V}\sum_{i=1}^{N_\ell} \ell_i \\ \sigma_P(\Phi_V) &= \frac{\Phi_V}{\sqrt{N_\ell}} \end{aligned} \tag{3.9}$$

area definition

Determining the particle fluence via its areal definition requires an additional step of calculation. Adjacent track spots are often identified as one object. This decreases the number of tracks spots N_A per area A and yields a falsely decreased fluence. Track spot reconstruction in each image plane exploits obtained trajectory information. Compare appendix D.3 for the full R script. Assuming homogeneous particle fields allows for averaging Φ_A over the total number of image slices N_z in the stack:

$$\begin{aligned} \Phi_A &= \frac{1}{N_z}\sum_{i=1}^{N_z} \Phi_A^{(i)} \text{ with } \Phi_A^{(i)} = \frac{1}{A}\sum_{j=1}^{N_A^{(i)}} \frac{1}{\cos\vartheta_j} \\ \sigma_P(\Phi_A) &= \frac{\Phi_A}{\sqrt{N_A}} \text{ with } N_A = \frac{1}{N_z}\sum_{i=1}^{N_z} N_A^{(i)}. \end{aligned} \tag{3.10}$$

In this case, the Poisson uncertainty $\sigma_P(\Phi_A)$ is governed by the mean number of track spots per image slice N_A.

3.6 Intensity Measurements

Fluorescent nuclear track detectors enable the possibility of energy loss determination by measuring the fluorescence intensity of individual track spots. Particles with a high ionization density will liberate many secondary electrons on their (mostly unaltered) path through the detector. This translates directly into a large number of transformed color centers, which produce a high fluorescence signal during readout. Thus, energy loss and track intensity directly correlate as already demonstrated in [5] and [8]. Due to confocal sectioning, fluorescence from an image plane of finite axial width (FWHM ≅ 860 nm) is gathered. Hence, the total track signal can be regarded as an electronic energy loss per path length. Since the energy deposition varies stochastically, only an intensity average along multiple image slices in depth will yield an estimate of ion LET. Alternatively, one can average over many track intensities in just one image slice in order to estimate the LET, provided monoenergetic irradiation.

3.6.1 2D symmetric Gaussian fit

It is important that APD saturation is corrected on the raw images prior to any intensity determination (cf. section 3.3.4). Measurements of circular track spots can then be performed directly in R using the FNTD package described in section 3.4.3. Required are particle tracker tables containing position and trajectory information. The measurement algorithm draws a disk of given radius around each listed track position and performs a 2D symmetric Gaussian fit on the contained pixel values according to equation 3.11. Output parameters are normalized track amplitude I_0, track width $\sigma_{x,y}$ and local background offset B_0 as well as mean, minimum and maximum pixel values contained in the regarded disk.

$$I(x,y) = \frac{I_0}{2\pi\sigma_{x,y}^2} \exp\left[-\frac{(x-x_0)^2+(y-y_0)^2}{2\sigma_{x,y}^2}\right] + B_0 \tag{3.11}$$

The peak amplitude $\hat{I} = I_0 / 2\pi\sigma_{x,y}^2 + B_0$ and the maximum pixel value I_{max} were found to be equivalent and robust intensity measures for orthogonal irradiations. The latter was chosen for simplicity reasons in all intensity examinations.

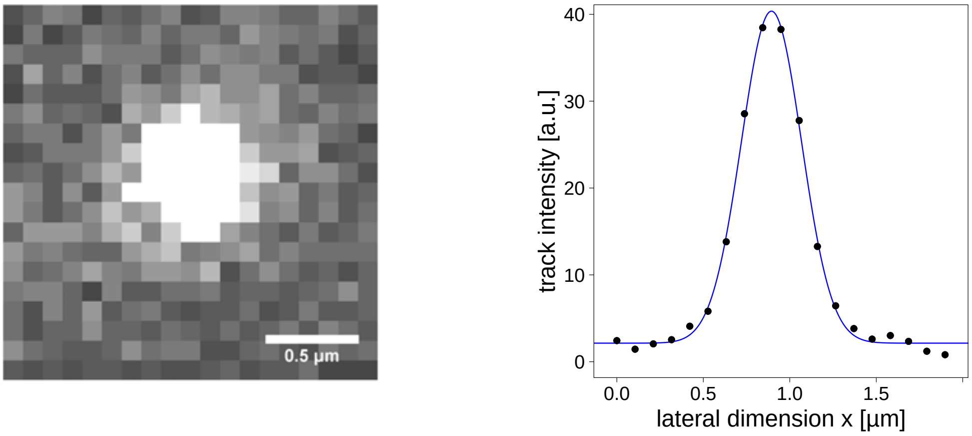

Figure 3.10: *Exemplary 1D Gaussian intensity fit for a circular carbon ion track spot (left); the fit was performed along the central x-axis of the intensity blob (right)*

3.6.2 Background subtraction

The MOSAIC package enables automated background intensity determination from obtained microscope images (cf. section 3.4). Mean local background offsets B were determined for each track spot by applying the intensity measurement algorithm (with identical tracker tables) on calculated background images. This methods works well for track intensities larger than the detector background, i.e. the set of background-reduced FNTDs. The fitted background value B_0 of equation 3.11

could not be used for local background subtraction, since they largely depend on the variable disk radius and peak intensity $\hat{I}$.

3.6.3 Adjusted count rate

Obtained maximum pixel values I_{max} were transformed to comparable adjusted count rates accounting for different laser powers p and dwell times τ during readout. Non-linearities in laser power normalization result in a correction factor f_p introduced in section 3.3.4. Additionally, the local background offset was subtracted from I_{max} for all analyzed background-reduced FNTDs yielding:

$$\eta_{adj} = \frac{1}{p\tau}\left(f_p I_{max} - B\right). \tag{3.12}$$

3.6.4 Intensity correction in depth

The readout-induced intensity loss in depth z due to observation volume broadening (cf. section 3.3.2) can be corrected via the mean fluorescence amplitudes of the images contained in a stack. Different detectors show a highly comparable relative intensity-loss behavior depicted in figure 3.11. Thus, it is feasible to correct measured track intensities in depth by dividing them by the corresponding relative mean image intensity.

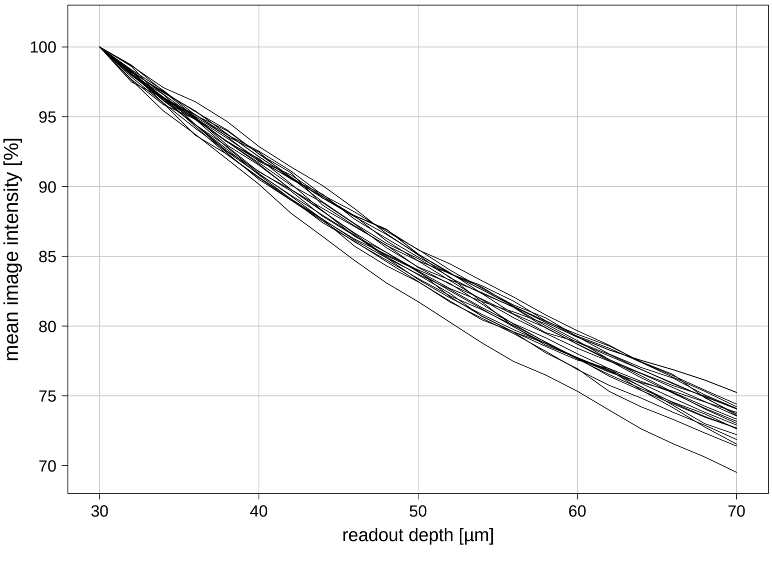

Figure 3.11: *Measured mean image intensities for 22 irradiated FNTDs with increasing readout depth z; obtained profiles are comparable in shape and independent of chosen laser power and irradiation type*

3.6.5 Determination of intensity straggling

The principle of intensity straggling measurements is depicted in figure 3.12. Following single ions in depth through the detection volume and correcting η_{adj} for axial readout-induced intensity loss yields information on the stochastic energy deposition behavior. All analyzed image stacks contain 21 slices and, hence, allow for mean $\mu(\eta_{adj})$ and standard deviation $\sigma(\eta_{adj})$ calculation along individual particle trajectories. The relative standard deviation

$$\sigma_{rel}(\eta_{adj}) = \sigma(\eta_{adj})/\mu(\eta_{adj}) \tag{3.13}$$

is independent from the multiplicative laser power correction factor f_p, since it scales $\mu(\eta_{adj})$ and $\sigma(\eta_{adj})$ equally.

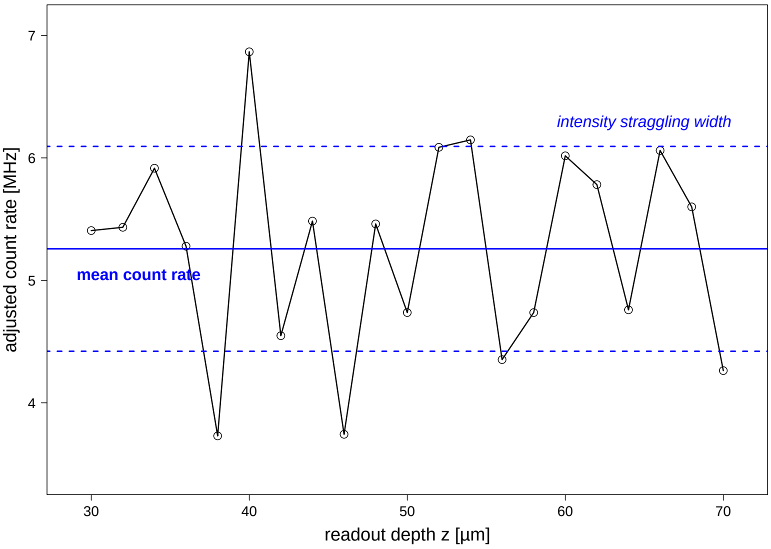

Figure 3.12: *Exemplary stochastic energy deposition along an individual ion track after intensity-depth correction; the intensity straggling width is determined by the standard deviation of the set of measured intensities*

3.6.6 Mean intensity of segmented objects

Ion tracks with polar and azimuthal angles $\vartheta, \varphi \neq 0°$ do not posses a circular track signature on the FNTD. They appear as elongated ellipses. Therefore, one needs to enhance the Gaussian fit routine allowing for asymmetric profiles. However, a more robust approach would be to use the mean object intensity provided in Squassh segmentation (cf. section 3.4), since it takes multiple pixel values into account. This requires a parameterization of the track area and its mean intensity with respect to the angle of incidence ϑ. Figure 3.13 schematically outlines image sectioning and color center excitation based on a 3D Gaussian approximation of the microscope PSF. Following model derivations are based on these simple geometric assumptions.

track area

The track area A increases with increasing ϑ. For a 3D Gaussian PSF of axial spread σ_{ax}, confocal sectioning yields

$$A(\vartheta) = \frac{\pi r}{\cos\vartheta}\left(r + \sigma_{ax}\sin\vartheta\right), \tag{3.14}$$

where r denotes the track radius under orthogonal irradiation ($\vartheta = 0°$).

mean intensity

The mean track intensity $\bar{I}$ decreases with increasing ϑ. A simple geometric model introduced in [44] links the length in the Gaussian illumination volume to the mean intensity obtained after readout, thus

$$\bar{I}(\vartheta) = \frac{\bar{I}(\vartheta = 0)}{\sqrt{\cos^2\vartheta + \varepsilon^2\sin^2\vartheta}} \tag{3.15}$$

with the PSF axis ratio $\varepsilon = \sigma_{ax}/\sigma_{lat}$.

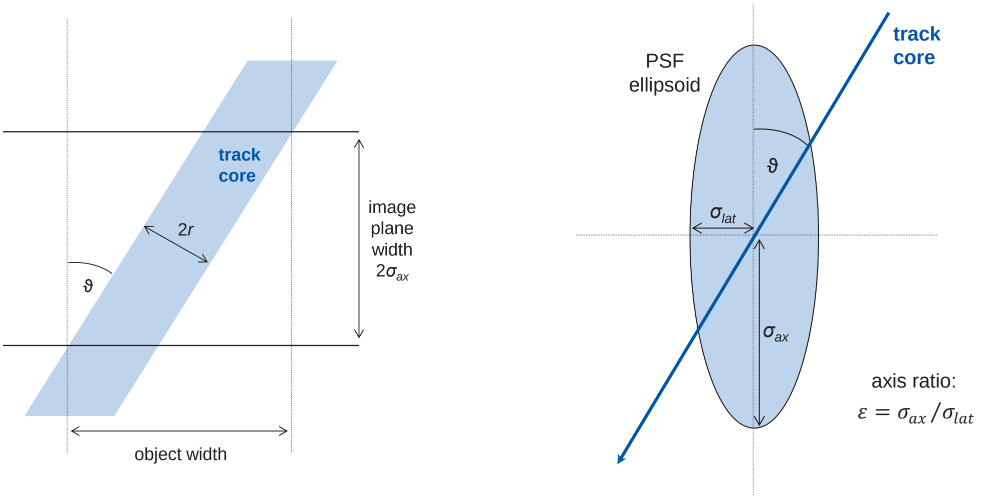

Figure 3.13: *Ion track intersecting the image plane under the polar angle ϑ (left); PSF ellipsoid stimulates fluorescence in its entire volume intersected by an ion track (right)*

3.7 Data Modeling

This section outlines the fitting routines applied to condense obtained measurement data $\{(x_1, y_2), \ldots, (x_n, y_n)\}$ in a common functional relation f, such that $y_i = f(x_i; \boldsymbol{\psi})$ for all $i \in \{1, \ldots, n\}$. The basic approach is simple [45]: In a first step, the model function f is designed interpolating data points based on the choice of free parameters $\boldsymbol{\psi} = \begin{pmatrix}\psi_1 & \cdots & \psi_p\end{pmatrix}^\top$. The second step involves choosing a figure-of-merit function X, which measures the agreement between model function and data. Small values mostly represent close agreement. The best-fit parameters minimize X in p-dimensional space.

Fitting is applied to establish an analytical correlation between fluorescent intensity and linear energy transfer (cf. section 5.2). It is also used to described the dependency of measured energy loss straggling on LET (cf. section 5.3).

3.7.1 Non-linear least squares

The figure-of-merit function chosen for this thesis is based on the method of non-linear least squares [45]. Additionally, a weighting factor is introduced, accounting for the differences in measurement uncertainty $\sigma(y_i)$:

$$\chi^2 := \sum_{i=1}^{n} r_i^2 = \sum_{i=1}^{n} \left[\frac{y_i - f(x_i; \boldsymbol{\psi})}{\sigma(y_i)}\right]^2, \tag{3.16}$$

with the weighted residual r_i. The reduced chi-squared

$$\chi^2_{red} = \frac{\chi^2}{n-p} = \frac{\chi^2}{\nu} \tag{3.17}$$

estimates the goodness of the fit statistic. As a rule of thumb, $\chi^2_{red} \approx 1$ indicates accordance between estimates and observations within error variance, whereas $\chi^2_{red} > 1$ indicates that the fit has not fully captured measurement data. The difference between the number of data points n and the number of free parameters p is denoted as ν and referred to as the number of degrees of freedom.

The standard errors of the fit parameters ψ_i lie on the diagonal of the variance-covariance matrix $\boldsymbol{\Sigma}$. Defining

$$\alpha_{kl} := \sum_{i=1}^{n} \frac{1}{\sigma^2(y_i)} \left[\frac{\partial f(x_i; \boldsymbol{\psi})}{\partial \psi_k} \frac{\partial f(x_i; \boldsymbol{\psi})}{\partial \psi_l}\right] \tag{3.18}$$

yields

$$\boldsymbol{\Sigma} = \chi^2_{red}\, \boldsymbol{\alpha}^{-1}, \tag{3.19}$$

with $\Sigma_{kk} = \mathrm{Var}(\psi_k) = \sigma^2(\psi_k)$ and $\Sigma_{kl} = \Sigma_{lk} = \mathrm{Cov}(\psi_l, \psi_k)$.

3.7.2 Confidence intervals

In all FNTD application, it will be of particular interest to determine the LET x_λ from a measured count rate $y_i = \lambda$. Furthermore, its standard error is desired to estimate measurement accuracy. For this purpose, it is necessary to invert the model function. The asymptotic variance of $f^{-1}(x_\lambda; \boldsymbol{\psi}) := h(\boldsymbol{\psi})$ can be approximated based on Taylor series expansion. Equation 3.20 is derived in [46] and commonly referred to as the delta method [47]:

$$\mathrm{Var}\left[h(\boldsymbol{\psi})\right] \cong \boldsymbol{\nabla} h(\boldsymbol{\psi})^\top \; \boldsymbol{\Sigma} \; \boldsymbol{\nabla} h(\boldsymbol{\psi}), \tag{3.20}$$

where

$$\boldsymbol{\nabla} h(\boldsymbol{\psi}) = \begin{pmatrix} \frac{\partial h(\boldsymbol{\psi})}{\partial \psi_1} \\ \vdots \\ \frac{\partial h(\boldsymbol{\psi})}{\partial \psi_p} \end{pmatrix} \tag{3.21}$$

is the vector of first order partial derivatives. Calculation of the best-fit parameters $\boldsymbol{\psi}$ and the variance-covariance matrix $\boldsymbol{\Sigma}$ allows for variance estimation of x_λ. Based on a q confidence interval, the delta method yields:

$$\sigma(x_\lambda) = t_\nu(q) \sqrt{\mathrm{Var}\left[h(\boldsymbol{\psi})\right]}. \tag{3.22}$$

$t_\nu(q)$ is the q quantile of a Student's t-distribution with ν degrees of freedom.

A full R script on confidence interval calculation can be found in appendix D.4.

4 EXPERIMENTS

In order to investigate the potential of FNTDs in terms of fluence-based dosimeters, two sets of detectors – conventional and background-reduced FNTDs – have been irradiated at HIT. Conducted measurements aimed towards advanced beam characterization based on fluence Φ, stopping power S and energy loss straggling $\sigma(S)$ assessment. Monoenergetic helium and carbon ion beams have been used to set up a fluence determination routine for multidirectional fields (section 4.1). The investigations concerning stopping power (section 4.2) and energy loss straggling determination (section 4.3) additionally involved irradiations with protons and oxygen ions. All FNTDs have been placed in homogeneous, monoenergetic particle fields of large lateral dimensions. This chapter outlines the different experimental setups and irradiation parameters as well as detector readout procedures (section 4.4).

4.1 Particle Fluence Determination

All FNTDs were placed precisely at isocenter (142.5 cm behind the vacuum window of the QA beam line at HIT) during irradiation. Fixed to the front of a large poly(methyl methacrylate) (PMMA) block, positioning via in-room lasers was feasible. Generation of multidirectional particle fields on individual detectors was realized by superimposing single $5 \times 5\,\mathrm{cm}^2$ unidirectional fields. The fluence of each sub-irradiation was chosen to be $\phi_{sub} = 0.2 \times 10^6\ 1/\mathrm{cm}^2$. Prior to the next sub-irradiation, the FNTD was rotated by $\Delta\vartheta = 15°$ against the beam axis. Figure 4.1 depicts the experimental setup. Radiochromic films (Kodak PPL) covering the detectors were used to monitor field homogeneity.

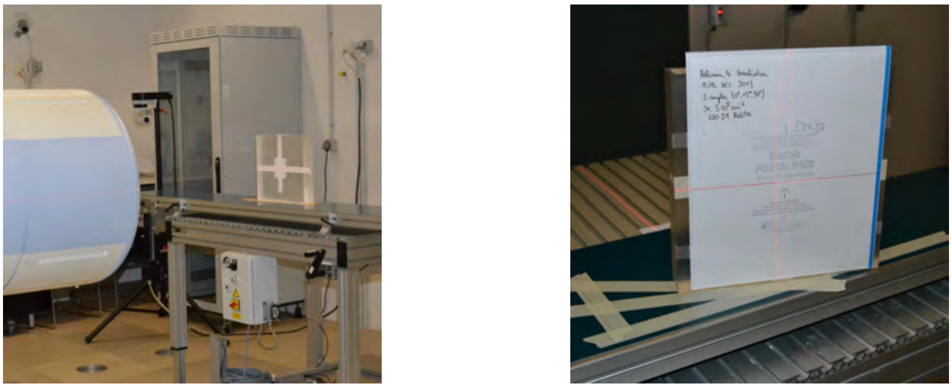

Figure 4.1: *FNTD fixed to the front of a large PMMA block and positioned at isocenter in the QA room (left); FNTD covered with Kodak PPL film and rotated 15° with respect to the unaltered beam direction (right)*

4.1.1 Simple multidirectional fields

The level of complexity of analyzed particle fields is determined by the number of sub-irradiations on one detector. Simple fields consist of three polar angles $\vartheta \in \{0°, 15°, 30°\}$. Table 4.1 shows that irradiations have been performed with both high-LET carbon ions and low-LET helium ions on two different days. In the following, FNTDs will be referred to according to their given ID.

	gk5007	**gk5150**
ion type	^{12}C	^{4}He
energy [MeV/u]	88.83	220.51
LET in Al_2O_3 [keV/µm]	92.02	5.56
total fluence [1/cm²]	0.6×10^6	
polar angles ϑ	0°, 15°, 30°	
azimuthal angle φ	0°	
date of irradiation	12/03/13	12/15/13

Table 4.1: *Irradiation parameters for the detectors gk5007 (high-LET carbon ion field) and gk5150 (low-LET helium ion field) both positioned at isocenter*

4.1.2 Complex multidirectional fields

Complex multidirectional fields consisted of six different polar angles $\vartheta \in \{0°, 15°, 30°, 45°, 60°, 75°\}$, thus having a total fluence of $\Phi = 1.2 \times 10^6$ 1/cm².

Figure 4.2: *Fixation of FNTDs gk5003 ($\varphi = 0°$, left), gk5004 ($\varphi = +90°$, top), gk5005 ($\varphi = \pm 180°$, right) and gk5006 ($\varphi = -90°$, bottom)*

Figure 4.2 shows, how an additional azimuthal angle variation was included.

FNTDs gk5003, gk5004, gk5005 and gk5006 have been rotated clockwise by 90° in the xy-plane yielding four detectors identical in ϑ but different in φ. Table 4.2 summarizes high-LET carbon ion irradiation parameters.

	gk5003	**gk5004**	**gk5005**	**gk5006**
ion type	^{12}C			
energy [$^{MeV}/_{u}$]	88.83			
LET in Al_2O_3 [$^{keV}/_{\mu m}$]	92.02			
total fluence [$^{1}/_{cm^2}$]	1.2×10^6			
polar angles ϑ	0°, 15°, 30°, 45°, 60°, 75°			
azimuthal angle φ	0°	+90°	±180°	−90°
date of irradiation	11/06/13			

Table 4.2: *Irradiation parameters for the detectors gk5003, gk5004, gk5005 and gk5006 utilizing high-LET carbon ions impinging the FNTDs under six polar and four detector-specific azimuthal angles*

4.2 Stopping Power Determination

FNTDs record energy loss is form of color center transformation. A high transformation density along a particle's trajectory corresponds to a high LET and yields bright fluorescent features in the obtained image stack. In order to investigate the correlation between track intensity and LET, FNTDs were fixed to a PMMA block and irradiated orthogonally at isocenter ($\vartheta = \varphi = 0°$). Monitoring field homogeneity with Kodak PPL films was omitted, since the precise particle fluence is of secondary interest for the following measurements.

4.2.1 Relative LET spectroscopy

Qualitative, relative LET spectroscopy using FNTDs involved irradiation of one detector with both low-LET protons and high-LET carbon ions with a total fluence of $\Phi = 6 \times 10^6\ ^{1}/_{cm^2}$. The fluence ratio was chosen to be 5:1 mimicking typical fragmentation fields in carbon ion therapy.

	gk5002	
ion type	^{1}H	^{12}C
energy [MeV/u]	221.06	88.83
LET in Al_2O_3 [keV/µm]	1.39	92.02
sub-fluence [1/cm²]	5×10^6	1×10^6
date of irradiation	11/06/13	

Table 4.3: *Irradiation parameters for the detector gk5002 irradiated with both low-LET protons and high-LET carbon ions at isocenter ($\vartheta = \varphi = 0°$)*

4.2.2 Absolute LET spectroscopy

calibration curve for conventional FNTDs

Quantitative, absolute LET spectroscopy refers to translating measured fluorescent intensity into LET. In order to calibrate utilized FNTDs, nine detectors were irradiated orthogonally at isocenter with monoenergetic ion fields including protons as well as helium and carbon and ions. The irradiation parameters for the calibration curve of conventional FNTDs are listed in table 4.4. The investigated $L_{Al_2O_3}$ range lies between 1 and 92 keV/µm.

	gk5001	**gk5140**	**gk5130**	**gk5120**	**gk5110**	**gk5101**	**gk5000**
ion type	^{1}H	^{4}He	^{4}He	^{4}He	^{4}He	^{4}He	^{12}C
energy [MeV/u]	220.42	220.51	177.16	143.52	106.55	50.57	88.83
LET in Al_2O_3 [keV/µm]	1.39	5.56	6.39	7.37	9.12	16.05	92.02
total fluence [1/cm²]	5×10^6	1×10^6					
date of irradiation	11/06/13	12/15/13					11/06/13

Table 4.4: *Irradiation parameters for the absolute LET calibration curve; detectors positioned at isocenter and orthogonal to beam direction ($\vartheta = \varphi = 0°$)*

Additionally, two FNTDs irradiated within a previous Bachelor's thesis [48] could be included in the calibration, since they were cut from the same crystal and their experimental setup was identical to the one used for this Master's thesis. Table 4.5 summarizes their properties.

	lb2000	**lb1000**
ion type	^{1}H	^{12}C
energy [MeV/u]	142.66	270.55
LET in Al_2O_3 [keV/µm]	1.85	43.12
total fluence [1/cm²]	5×10^6	3×10^6
date of irradiation	02/19/13	

Table 4.5: *Irradiation parameters for the detectors lb2000 and lb1000 positioned at isocenter and orthogonal to beam direction ($\vartheta = \varphi = 0°$) [48]*

calibration curve for background-reduced FNTDs

A more detailed study including the uncertainties of LET calibration was conducted within a supplementary Bachelor's thesis [21]. The investigated set of FNTDs shows largely reduced background signal in comparison to previously irradiated conventional FNTDs. For each LET level, three different detectors were irradiated simultaneously with a $5 \times 5\,\mathrm{cm}^2$ monoenergetic ion field yielding $3 \times 30 = 90$ irradiated FNTDs in total. The experimental setup was identical to the one describe at the beginning of this section. However, oxygen ions have been included increasing the upper $L_{Al_2O_3}$ range limit to approximately 150 keV/µm. All irradiation and readout specifications can be found under [21], whereas table 4.6 summarizes the essential parameters.

ion type	**$L_{Al_2O_3}$ range**	**# irradiated FNTDs**	**date of irradiation**
^{1}H	1.39 – 4.17 keV/µm	$3 \times 5 = 15$	05/05/14
^{4}He	5.62 – 10.02 keV/µm	$3 \times 5 = 15$	05/05/14
^{4}He	8.99 – 27.58 keV/µm	$3 \times 6 = 18$	08/01/14
^{12}C	33.91 – 90.16 keV/µm	$3 \times 6 = 18$	05/05/14
^{16}O	61.34 – 148.2 keV/µm	$3 \times 8 = 24$	04/20/14

Table 4.6: *Summarized irradiation parameters for novel background-reduced detectors (hm ID) positioned at isocenter and orthogonal to beam direction ($\vartheta = \varphi = 0°$); highlighted helium irradiation was partly performed with an energy degraded beam to achieve $L_{Al_2O_3}$ values between 16 and 34 keV/µm (accelerator limitation); compare appendix C for a detailed irradiation protocol*

4.3 Energy Loss Straggling

4.3.1 Energy loss straggling and atomic number

Irradiations conducted to investigate the influence of atomic number Z on energy loss straggling involved exposure of one detector to two sub-fields nearly identical in LET but different in ion type. Accelerator limitations at HIT allowed for combination of protons and helium ions as well as carbon and oxygen ions (see table 4.7). Sub-fluences were chosen to be identical yielding a total particle fluence of $\Phi = 2 \times 10^6\,{}^{1}/_{\mathrm{cm}^2}$ on each FNTD.

	gk6201		**gk6202**		**gk6203**	
ion type	^{1}H	^{4}He	^{12}C	^{16}O	^{12}C	^{16}O
energy [$^{\mathrm{MeV}}/_{\mathrm{u}}$]	48.12	220.51	155.26	430.32	118.52	294.58
LET in Al_2O_3 [$^{\mathrm{keV}}/_{\mathrm{\mu m}}$]	4.17	5.56	61.47	61.34	74.29	74.49
sub-fluence [$^{1}/_{\mathrm{cm}^2}$]	1×10^6		1×10^6		1×10^6	
date of irradiation	05/05/14		05/05/14	04/20/14	05/05/14	04/20/14

Table 4.7: *Irradiation parameters for the detectors gk6201, gk6202, gk6203 irradiated with two monoenergetic ion fields of same LET but different Z ($\vartheta = \varphi = 0°$)*

4.3.2 Energy loss straggling and LET

The dependency of energy loss straggling on LET was analyzed using background-reduced FNTDs irradiated within the absolute LET calibration study (cf. table 4.6 in section 4.2.2). Additional experiments were not required for this investigation.

4.4 Detector Readout

Irradiated detectors were read out with the Zeiss LSM 710 confocal microscope introduced in section 3.3. Within this thesis, image acquisition was conducted with the 63×/1.40 Oil DIC M27 objective lens. The pinhole diameter was set to 1.00 AU at all times. FNTD readout always involved acquisition of z-stacks except for the analysis concerning absolute LET calibration. Here, single images at 30 µm readout depth were sufficient. The relative laser power p was varied according to measured track intensities and/or desired signal-to-noise ratios (SNRs) [31]. It is specified in chapter 5 whenever of particular importance. Table 4.8 summarizes all common readout parameters.

laser wavelength λ_{ex}	633 nm
pixel matrix	1280 × 1280
image size	134.8 × 134.8 µm
dwell time τ	40.34 µs
zoom	1.0
axial readout range	30 − 70 µm
axial step size Δz	2 µm
slices per z-stack	21

Table 4.8: *Microscope readout parameters universal for all images acquired with the* Zeiss *LSM 710 confocal microscope*

Figure 4.3 shows two exemplary microscope images at 30 µm readout depth. One can see a complex multidirectional carbon ion field on the left and a detector irradiated with both low-LET protons and high-LET carbon ions on the right. Respective grayscales were adjusted for optimal visualization contrast.

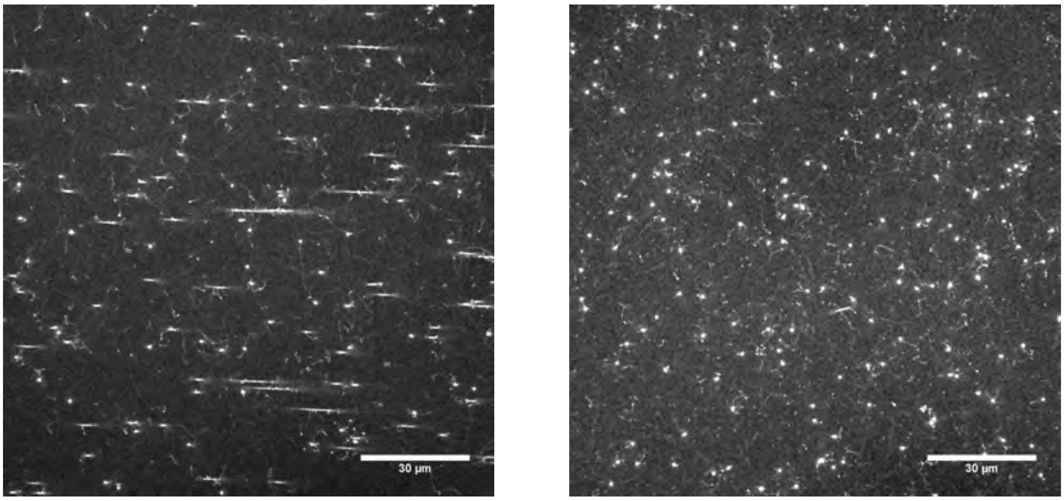

Figure 4.3: *Microscope readout results for the detectors gk5003 (left) and gk5002 (right) obtained at 30 µm depth with 100% relative laser power; one can see bright individual ion tracks on relatively low detector background; small polar angle tracks appear circular while large polar angle tracks appear ellipsoidal in multidirectional fields (left); irradiation with low and high-LET particles shows large intensity differences that convey the impression of track size variations (right)*

5 RESULTS

This chapter outlines the analysis results of all conducted measurements. Fluence determination of simple and complex multidirectional fields is presented in section 5.1. LET calibration curves for conventional and background-reduced FNTDs are displayed in section 5.2. Furthermore, a correlation between polar angle ϑ and mean track intensity is introduced in this section. The analysis of energy loss straggling $\sigma(S)$ was based on intensity straggling measurements $\sigma(\eta)$ along individual ion tracks. Dependencies of $\sigma(\eta)$ on detector background, atomic number and LET are investigated in section 5.3.

5.1 Particle Fluence Determination

Particle fluence determination is based on image segmentation elucidated in section 3.5. For each detector, a single z-stack was acquired with 100% relative laser power ensuring optimal SNR. Linear trajectory reconstruction and fluence calculation were implemented in automated R routines with universal parameters for all FNTDs analyzed in this section.

5.1.1 Simple multidirectional fields

Table 5.1 summarizes fluence determination results for FNTDs irradiated with three high-LET carbon ion (gk5007) and three low-LET helium ion fields (gk5150), respectively (cf. table 4.1 for explicit irradiation parameters).

	gk5007	**gk5150**
# trajectories	125	126
azimuthal angle φ	$+(1.3 \pm 3.0)^\circ$	$+(1.3 \pm 3.0)^\circ$
fluence Φ_A [10^6 $^1/_{\mathrm{cm}^2}$]	0.71 ± 0.06	0.71 ± 0.06
fluence Φ_V [10^6 $^1/_{\mathrm{cm}^2}$]	0.71 ± 0.06	0.71 ± 0.06

Table 5.1: *Fluence determination results for the detectors gk5007 and gk5150; fluence definitions introduced in section 2.2 are equivalent for the conducted measurements; fluence errors are governed by the Poisson uncertainty on the number of detected tracks in the readout volume; calculated azimuthal angles φ agree with the experimental setup*

The obtained azimuthal angles agree with the experimental setup ($\varphi = 0°$). Both fluence definitions Φ_A and Φ_V are equivalent, when applying track spot reconstruction explained in section 3.5.5. The propagated statistical regression errors ($\sim 0.001 \times 10^6$ ¹/cm²) are much smaller than the Poisson uncertainty on the total number of detected ion trajectories in the regarded readout volume. Thus, this uncertainty was considered to be negligible. For both ion fields, the deduced fluence is 18% above the expected value of $\Phi_{ref} = 0.6 \times 10^6$ ¹/cm².

The characterization of the angular distribution on gk5007 is shown in figure 5.1. All three polar angles $\vartheta = 0°, 15°, 30°$ could clearly be reproduced and distinguished. Ion tracks with intermediate angles are rare. The slight positive offset observed appears to decrease with increasing ϑ.

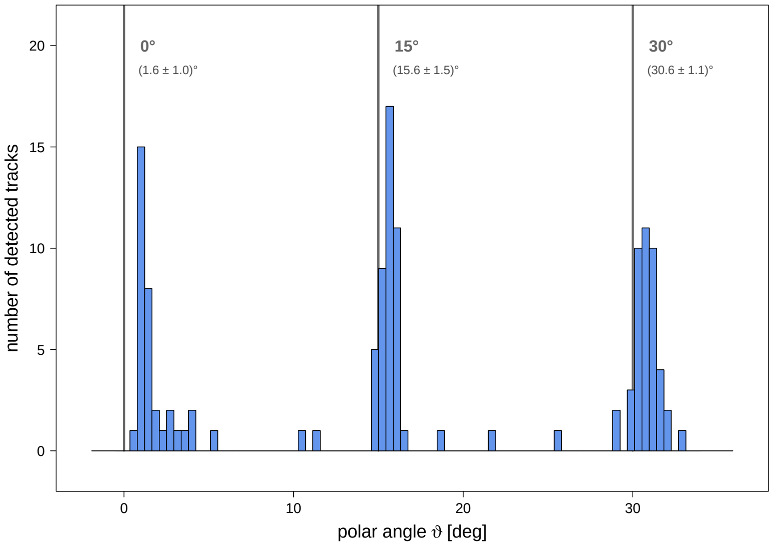

Figure 5.1: *Result of particle field analysis (125 detected tracks) based on image segmentation and linear trajectory reconstruction for gk5007 irradiated with high-LET carbon ions under three different polar angles ($\vartheta = 0°, 15°, 30°$); stated means have been averaged over the interval* $[\vartheta - 7.5°; \vartheta + 7.5°)$

5.1.2 Complex multidirectional fields

Complex multidirectional fields were generated with six sub-irradiations from different polar angles. In addition, the azimuthal angle was rotated for each investigated FNTD. The analysis routine is identical to the one described in the previous section (5.1.1).

Figure 5.2 shows that all six irradiation angles could be reproduced and distinguished in the automated evaluation routine. Furthermore, the number of detected tracks decreases with increasing ϑ as expected according to the fluence definition.

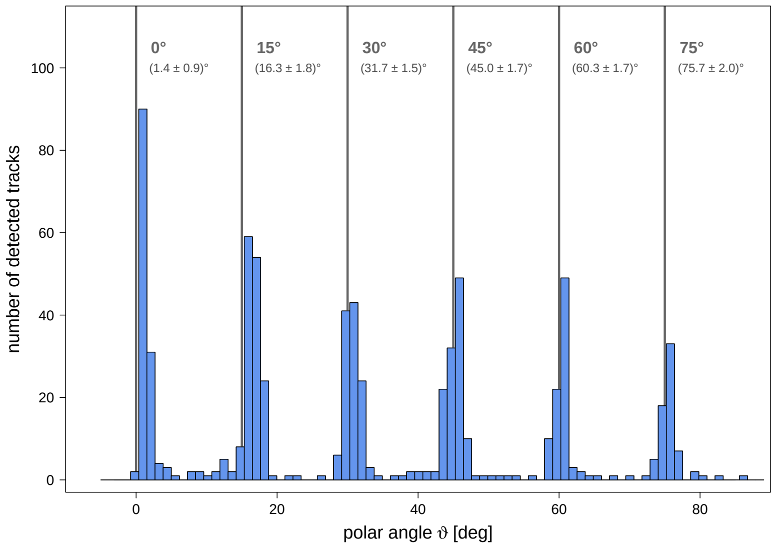

Figure 5.2: *Result of particle field analysis (701 detected tracks) based on image segmentation and linear trajectory reconstruction for gk5003, gk5004, gk5005 and gk5006 irradiated with high-LET carbon ions under six different polar angles ($\vartheta = 0°, 15°, 30°, 45°, 60°, 75°$); stated means have been averaged over the interval $[\vartheta - 7.5°; \vartheta + 7.5°]$*

The correlation between polar and azimuthal angles emphasizes that φ determination is robust for $\vartheta \geq 15°$. For $\vartheta = 0°$, the azimuthal angle falls into geometrical insignificance.

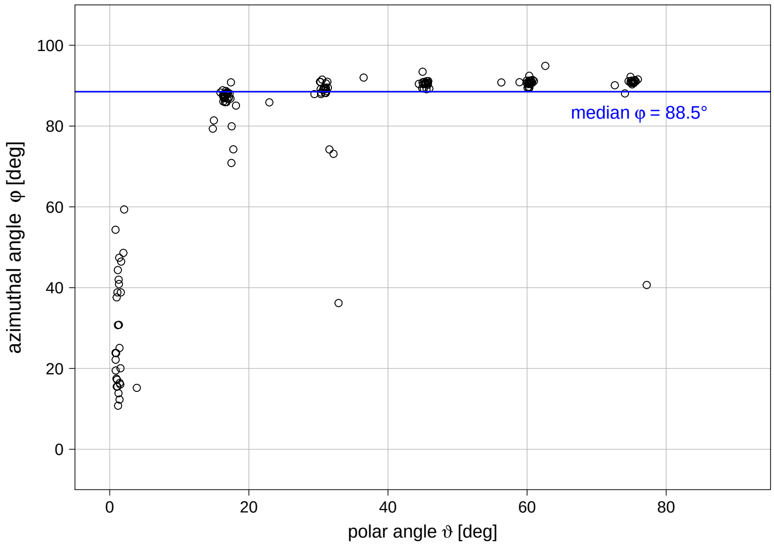

Figure 5.3: *Dependencies in polar and azimuthal angle determination for gk5004 ($\varphi = 90°$) irradiated with high-LET carbon ions under six different polar angles ($\vartheta = 0°, 15°, 30°, 45°, 60°, 75°$); 189 detected tracks*

Final fluence results stress the equivalence of Φ_A and Φ_V once again. Obtained polar angles ϑ are in high agreement with the experimental setup. Comparing the four detectors emphasizes Poisson fluctuations on the total number of detected trajectories, which directly influence fluence determination.

	gk5003	**gk5004**	**gk5005**	**gk5006**
# trajectories	179	160	196	166
azimuthal angle φ	$+(2.5 \pm 1.9)^\circ$	$+(84.7 \pm 2.3)^\circ$	$+(169.2 \pm 2.8)^\circ$	$-(86.6 \pm 1.1)^\circ$
fluence Φ_A $[10^6\ {}^{1}/_{\mathrm{cm}^2}]$	1.12 ± 0.10	1.07 ± 0.09	1.36 ± 0.10	1.05 ± 0.09
fluence Φ_V $[10^6\ {}^{1}/_{\mathrm{cm}^2}]$	1.12 ± 0.08	1.07 ± 0.08	1.33 ± 0.10	1.04 ± 0.08

Table 5.2: *Fluence determination results for the detectors gk5003, gk5004, gk5005 and gk5006; fluence definitions introduced in section 2.2 are equivalent for the conducted measurements; fluence errors are governed by the Poisson uncertainty on the number of detected tracks in the readout volume; calculated azimuthal angles φ agree with the experimental setup*

Averaging Φ_V and considering 701 ion tracks in total yields a final agreement of

$$\boldsymbol{\Phi_V / \Phi_{ref} = (95.0 \pm 3.6)\%} \tag{5.1}$$

with the chosen reference fluence of $\Phi_{ref} = 1.2 \times 10^6\ {}^{1}/_{\mathrm{cm}^2}$.

5.2 Stopping Power Determination

Both total particle fluence and stopping power spectrum are necessary to calculate the physical dose deposited by any heterogeneous heavy ion field (cf. equation 2.10). While the previous section provides a routine for calculating the particle fluence of complex multidirectional fields, this section presents the results of LET determination improvement using FNTDs. For this purpose, all detectors have been irradiated orthogonally and the maximum pixel value of a circular track spot was found to be a robust intensity measure. The dependency of fluorescence strength on irradiation angle (here ϑ) is investigated in section 5.2.3.

5.2.1 Relative LET spectroscopy

The irradiation of one detector (gk5002) with two ion fields differing in LET was conducted to verify the feasibility of LET assessment in heterogeneous particle fields. Figure 5.4 shows that the wide LET gap in irradiation (protons with 1.39 ${}^{\mathrm{keV}}/_{\mu\mathrm{m}}$ and carbon ions with 92.0 keV/µm) translates into a broad intensity gap in the corresponding histogram.

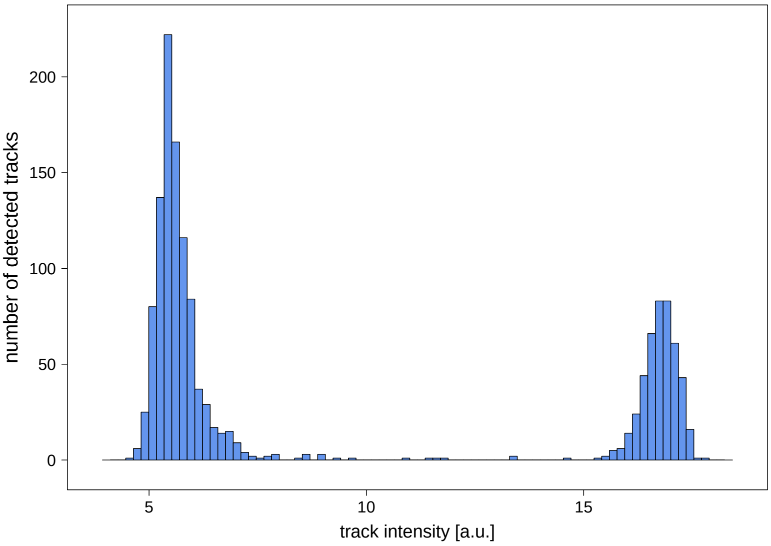

Figure 5.4: *Relative intensity spectroscopy on gk5002 irradiated with both low-LET protons (1.39 keV/µm) and high-LET carbon ions (92.0 keV/µm); the fluence ratio was determined to be 2:1 (expected 5:1) based on the analysis of 1,436 tracks*

The proton-carbon fluence ratio was expected to be 5:1. But since the signal of low-LET protons is only slightly above background level, their detection accuracy suffered, resulting in a measured ratio of 2:1. The carbon ion fluence deviates less than 10% from irradiation reference.

5.2.2 Absolute LET spectroscopy

Current LET calibration curves either hold for an LET range of clinical irrelevance [5] or suffer from large uncertainties [8]. This section presents the results of improvements in $L_{Al_2O_3}$ calibration between 1 and 150 keV/µm as well as a quantification of observed intensity fluctuations.

calibration curve for conventional FNTDs

This calibration curve is based on nine irradiations of conventional FNTDs described in section 4.2.2. The relative laser power was decreased from 100% to 7% according to the investigated LET to ensure comparable photon counts (~ 2.5 MHz) and minimized APD saturation. However, track intensities could not be normalized to a reference laser power p_{ref} according to equation 3.4, since the corresponding correction factor f_p was not investigated for this set of detectors. Therefore, Figure 5.5 depicts an f_p uncorrected correlation between η_{adj} and L:

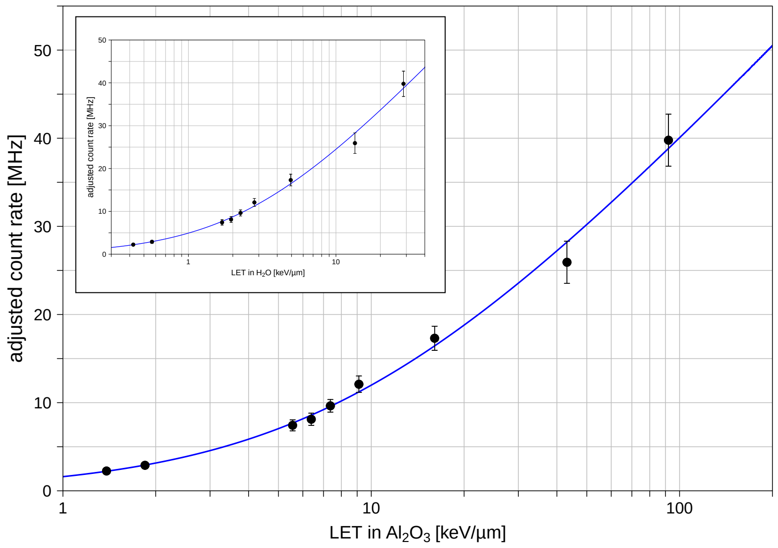

Figure 5.5: *Absolute LET calibration curve for conventional FNTDs based on nine irradiations with monoenergetic particle fields; measured count rates are not normalized to a reference laser power* p_{ref}*; depicted error bars represent the standard deviation of the mean intensity distribution; the blue line represents the logarithmic dependency of* η_{adj} *on* $L_{Al_2O_3}$*; the enclosed graphic shows the functional relation after conversion to LET in* H_2O

For absorbed dose to water calculations, desired in all clinical applications, one can simply convert $L_{Al_2O_3}$ to the corresponding linear energy transfer in water. The conversion factor is governed by the electron density ratio. Dependencies on mean excitation energy I and ion velocity β are considered, when converting stopping powers according to tabulated SRIM data. The functional relation between adjusted count rate η_{adj} and LET can in both cases be described by a simple power law, with $\eta_{adj} \propto \sqrt{L}$. In order to be able to compare conventional and background-reduced FNTDs, a more general logarithmic fit function with three free parameters a, b and c was chosen:

$$\boldsymbol{\eta_{adj} = a \log\left(L_{Al_2O_3} + b\right) + c} \tag{5.2}$$

$$\text{with } a = (36.9 \pm 3.7)\,\text{MHz},\ \ b = (8.9 \pm 1.6)\,{}^{\text{keV}}/_{\mu\text{m}} \text{ and } c = (-35.1 \pm 6.2)\,\text{MHz}.$$

calibration curve for background-reduced FNTDs[1]

Background-reduced FNTDs show a different LET response. Their fluorescence intensity η_{adj} is proportional to $\log(L)$. This can be seen in figure 5.6. The observed proportionality was enhanced by two additional free parameters in order to fit the same logarithmic function introduced in equation 5.2 to obtained data

---

[1] Results presented in this section have been obtained in a supplementary Bachelor's thesis [21].

points. Furthermore, laser power correction ($p_{ref} = 10\%$) was considered for this set of detectors.

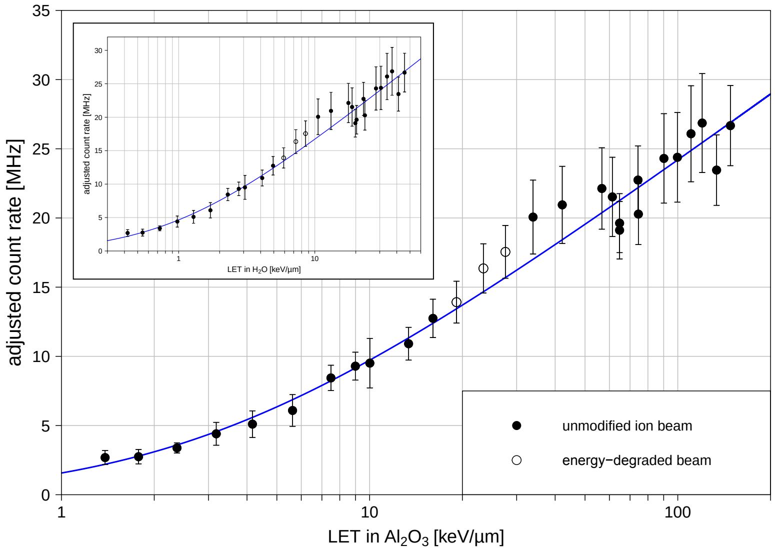

Figure 5.6: *Absolute $L_{Al_2O_3}$ (and L_{H_2O} for enclosed graphic) calibration curve based on 64 analyzed background-reduced FNTDs irradiated with monoenergetic particle fields; laser power normalization to $p_{ref} = 10\%$ was considered; depicted error bars include intra- and inter-detector variabilities; hollow circles represent irradiations with energy-degraded ^{4}He ion beams*

$$\boldsymbol{\eta_{adj} = a \log\left(L_{Al_2O_3} + b\right) + c} \tag{5.3}$$

with $a = (16.2 \pm 1.0)\,\text{MHz}$, $b = (3.1 \pm 0.8)\,{}^{\text{keV}}/_{\text{µm}}$ and $c = (-8.3 \pm 1.8)\,\text{MHz}$.

Dedicated investigations showed intra-detector related intensity variabilities of $(4.2 \pm 0.2)\%$ on average, meaning that the readout position on the FNTD can influence fluorescence measurements. Inter-detector related variabilities were, on average, determined to be even larger: $(18.7 \pm 1.8)\%$. Thus, sensitivity differences from one detector to another have a major impact on absolute intensity determination.

5.2.3 Influence of irradiation angles on mean track intensity

Presented calibration curves hold for particle fields impinging FNTDs orthogonally only. Since the illuminated focal plane is always parallel to the detector surface during readout, ion tracks with $\vartheta \neq 0°$ will have a decreased maximum intensity compared to perpendicular ion tracks of the same LET. Additionally, their track shape changes according to the angle of intersection, demanding a more robust intensity measure (e.g. mean object intensity). In section 3.6.6, two simple geometric approaches are outlined modeling both track area and mean intensity dependency on ϑ. They assume a 3D Gaussian PSF with axial and lateral spread σ_{ax} and

σ_{lat}, respectively. Figure 5.7 shows that the track area increases with increasing ϑ. The blue fit line of equation 3.14 to the data yields an axial PSF spread of $\sigma_{ax} = (550 \pm 28)\,\text{nm}$. Calculation according to [28] yielded $\sigma_{ax} = 366\,\text{nm}$.

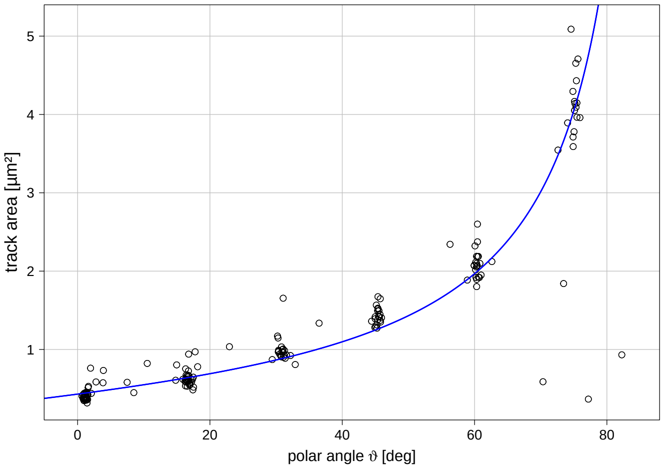

Figure 5.7: *Correlation between polar angle ϑ and segmented track area A for gk5004; the geometrical model interpolating measured data assumes an axial spread of the 3D Gaussian PSF of 550 nm and a mean 0° track radius of 0.37 µm*

Figure 5.8 shows that the mean intensity of outlined objects decreases with increasing polar angle ϑ. The blue fit line of equation 3.15 to the data yields a PSF axis ratio of $\varepsilon = \sigma_{ax}/\sigma_{lat} = (3.4 \pm 0.1)$. Calculation according to [28] resulted in $\varepsilon = 3.6$. A dependency of track area or mean track intensity on azimuthal angle φ was not observed.

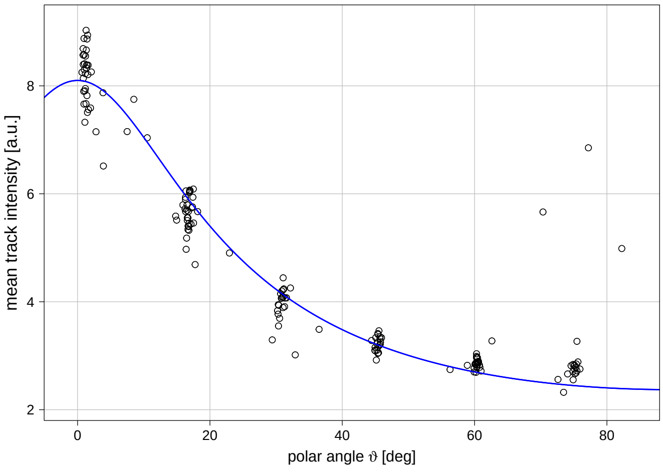

Figure 5.8: *Correlation between polar angle ϑ and mean track intensity $\mu(I)$ for gk5004; the geometrical model [44] interpolating measured data assumes a 3D Gaussian PSF with axis ratio $\varepsilon = 3.4$*

5.3 Energy Loss Straggling

The stochastic energy deposition of heavy charged particles can be monitored using FNTDs in terms of intensity straggling along individual ion trajectories. The analysis method applied is introduced in section 3.6.5. It exploits the 3D track information acquired from image segmentation and particle tracking. All measurements were performed on background-reduced FNTDs. Their background signal is largely decreased in comparison to conventional FNTDs, but relative background fluctuations remain of the same order of magnitude. Thus, section 5.3.1 investigates the influence of the detector background on relative intensity straggling $\sigma_{rel}(\eta_{adj})$, before sections 5.3.2 and 5.3.3 summarize dependencies of $\sigma_{rel}(\eta_{adj})$ on atomic number and LET.

5.3.1 Influence of detector background

The left plot in figure 5.9 displays adjusted count rates measured on three different detectors (hm1118, hm2118, hm4118) irradiated with the same particle field ($61.34\,^{\mathrm{keV}}/_{\mathrm{\mu m}}$ oxygen ions). Local background subtraction and laser power correction was applied. Each data point represents the maximum track intensity averaged over 21 image slices. One can observe large inter-detector variabilities originating from background differences. Furthermore, the microscope flat field is superimposed on measured intensities decreasing track signals at the outer edge of the confocal image. Determining the intensity straggling along observed ion tracks according to section 3.6.5 yields the right plot in figure 5.9. $\sigma_{rel}(\eta_{adj})$ is robust against detector sensitivity fluctuations and primarily governed by the stochastic energy deposition in the regarded image slices.

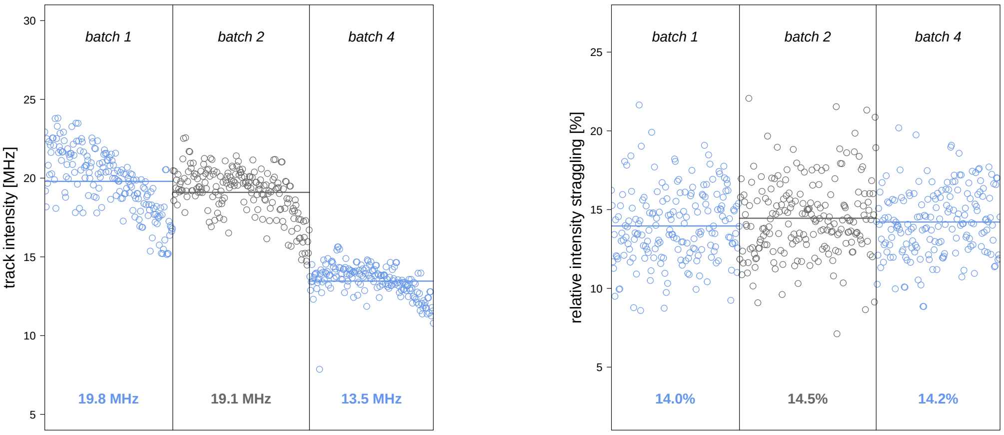

Figure 5.9: *hm1118 (batch 1), hm2118 (batch 2) and hm4118 (batch 4) all irradiated with $61\,^{\mathrm{keV}}/_{\mu m}$ oxygen ions yield very different count rates according to their sensitivity (left); the relative intensity straggling along individual ion tracks is scarcely influenced by these inter-detector variabilities (right)*

5.3.2 Energy loss straggling and atomic number

The influence of atomic number Z on relative intensity straggling was investigated on FNTDs irradiated with two particle fields of similar LET but different Z (cf. table 4.7). Plotting $\sigma_{rel}(\eta_{adj})$ over η_{adj} yields data clouds that show one limit point only. In order to exclude sample-size-related statistics, additional two z-stacks were analyzed for gk6201 resulting in $N = 911$ tracks. Based on the relative intensity straggling $\sigma_{rel}(\eta_{adj})$ along individual particle trajectories, the two ion species could not be distinguished.[2]

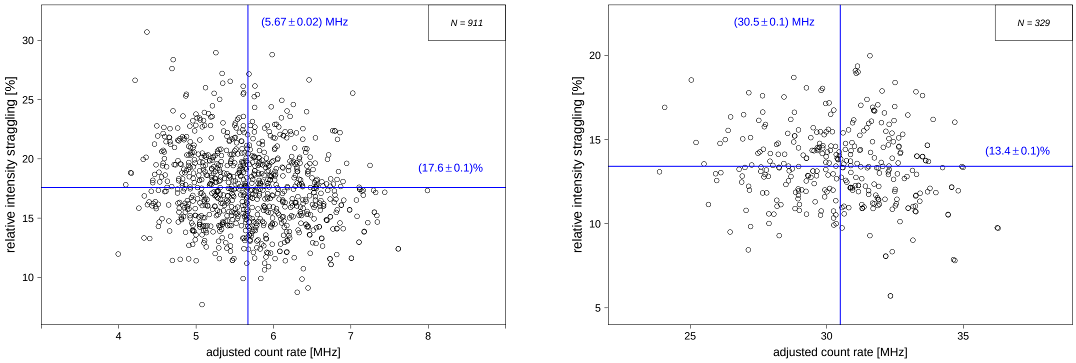

Figure 5.10: *Relative intensity straggling measurements for detectors irradiated with both protons and helium ions (left, gk6201) and carbon and oxygen ions (right, gk6203), respectively, having the same LET; both data sets show one limit point at the cross of the blue means*

5.3.3 Energy loss straggling and LET

The mean relative intensity straggling was determined for all FNTDs irradiated orthogonally and with monoenergetic particle fields (9 conventional and 22 background-reduced FNTDs). 1,775 + 6,183 = 7,958 ion tracks have been followed along 21 image slices in total. It is worth mentioning that intensity straggling values for both background-reduced and conventional FNTDs fall on the same hyperbolic curve parameterized by two parameters α and β:

$$\boldsymbol{\sigma_{rel}(\eta_{adj}) = \alpha + \beta / L_{Al_2O_3}} \qquad (5.4)$$

$$\text{with } \alpha = (13.4 \pm 0.1)\% \text{ and } \beta = (18.4 \pm 0.8)\,{}^{\text{keV}}/_{\mu\text{m}}.$$

Each data point in figure 5.11 represents a mean relative intensity straggling averaged over all trajectories visible in the corresponding z-stack. $\sigma_{rel}(\eta_{adj})$ decreases with increasing LET and levels off for $L_{Al_2O_3} \geq 20\,{}^{\text{keV}}/_{\mu\text{m}}$. A dependency of intensity straggling on particle type was not observed.

---

[2] The track width obtained by the symmetric 2D Gaussian fit is governed by the lateral spread of the microscope PSF. It remains constant over a wide LET and Z range [8]. Hence, it cannot be used to differentiate between particles.

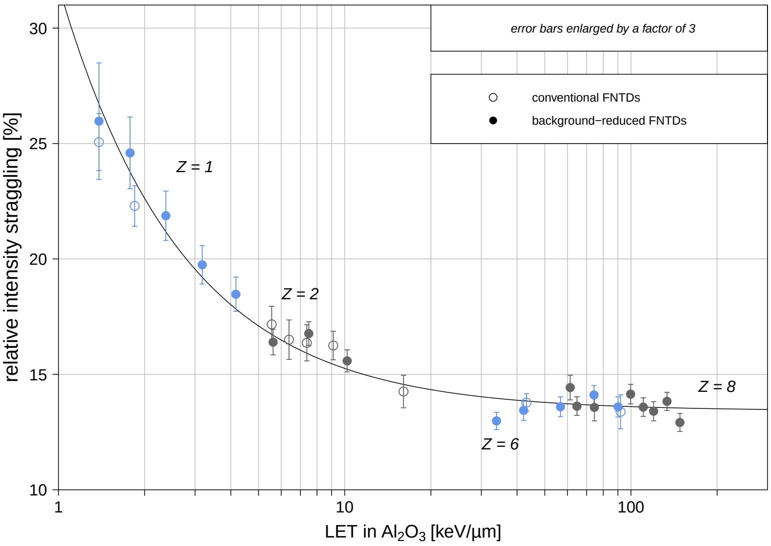

Figure 5.11: *The measured intensity straggling along individual ion tracks decreases with increasing LET following a hyperbolic curve; intensity straggling was determined for background-subtracted tracks; conventional (hollow circles) and background-reduced FNTDs (solid circles) show the same behavior; depicted error bars represent the standard error of the mean relative intensity straggling per LET data point; an influence of the particle type on* $\sigma_{rel}(\eta_{adj})$ *is not observed*

6 DISCUSSION AND OUTLOOK

This chapter discusses analysis results of all conducted measurements. The accuracy limiting factors of fluence and LET determination are outlined in section 6.1 and 6.2. Furthermore, two novel methods concerning quantification of and correction for detector sensitivity fluctuations are introduced in section 6.4. One of them utilizes background-independent energy straggling measurements discussed in section 6.3.

The established analysis routines are applied to a conventional FNTD positioned near the Bragg peak of a monoenergetic carbon ion field (cf. figure 6.1). As outlined in section 2.1.3, carbon ions will undergo fragmentation along their passage through matter, which causes a loss of primary particles and a build-up of lower-Z fragments. These fragments (mostly protons and helium ions) have a much lower LET because of their decreased charge. The heavy ion field near the Bragg peak is, therefore, mixed in particle type and energy. Calculated fluence and LET are compared to the reference values provided by the treatment planning software at HIT. The level of accuracy required for reliable fluence-based dosimetry using FNTDs is investigated in section 6.5.

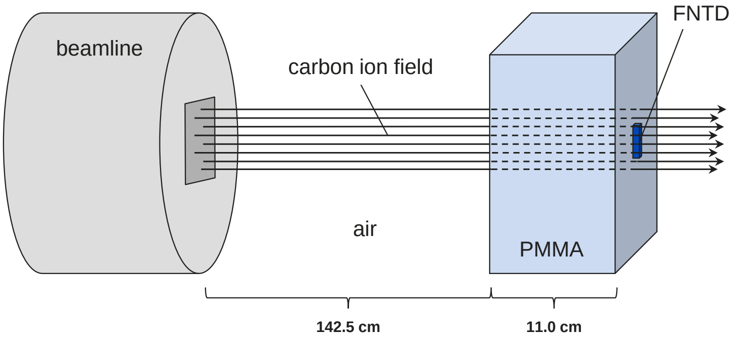

Figure 6.1: *Conventional FNTD (lb1006) placed behind 11 cm PMMA and irradiated with 270.55* $^{MeV}/_u$ *carbon ions at HIT [48]; build-up material accounts for a total water equivalent thickness of (13.1 ± 0.3) cm; stated error estimates positioning (±1 mm) and PMMA density uncertainties (±2%); Bragg peak position is at 14.1 cm water depth measured from isocenter*

6.1 Particle Fluence Determination

Particle fluence determination was successfully expanded to multidirectional fields by introducing novel image processing software (section 3.4.2) and data analysis routines (section 3.5). Reliable yet time-consuming Squassh segmentation yields reproducible trajectory sets after careful parameter tuning (e.g. regularization and minimum object intensity). Trajectory reconstruction by linear regression allows for track length and particle fluence determination. Furthermore, it enables track-by-track LET and energy straggling calculation. Observed deviations from the chosen reference fluence will be discussed in the following section.

6.1.1 Fluence uncertainty budget

Particle fluence determination in multidirectional fields faces a long list of accuracy limiting factors. They are ordered by decreasing impact:

- The image size (or number of evaluated image stacks) has the largest influence on fluence determination. Due to the finite graininess of the particle field and its statistical distribution, the relative fluence uncertainty can only be minimized by maximizing the readout area. A reference fluence of $1 \times 10^6\,{}^{1}\!/\!_{\mathrm{cm}^2}$ and a typical image size of $135 \times 135\,\mu\mathrm{m}^2$ would require 14 stacks (7 h readout time on current equipment) to achieve a relative measurement uncertainty less than 2%. This is not practicable.

- Positioning uncertainties in the beam, detector movement during readout or a readout-depth-dependent axial scaling factor can lead to false polar angles ϑ. The positive offset observed in figure 5.2 might originate from such systematic errors. ϑ is on average 0.7° larger than expected from the experimental setup. The offset decreases for increasing polar angles.

- Image segmentation works most effectively for high SNRs, since it detects all pixels above a given minimum intensity threshold. If the analyzed field contains a significant amount of fast (low-LET) particles, the minimum object intensity needs to be decreased, which inevitably yields high-energetic secondary electron detection. Although these electrons move on curved paths, they could be linked with true ion tracks challenging reliable trajectory reconstruction.

- When analyzing FNTDs irradiated under polar angles larger than 30°, crossing trajectories occur with significant frequency. Around the image slice of intersection, their track spots might be so close that they are outlined as one object. This typically results in four trajectory segments, which can partly be combined by the introduced trajectory filter function (section 3.5.4).

- The change of shape and loss of mean object intensity according to the angle of intersection (section 3.6.6) result in least significant uncertainties. Elongated ellipses could be split up in two (or more) objects in the segmentation stage. But since such splitting varies between image slices, the effect on the final fluence is negligible. The same holds for uncertainties in object position determination. The intensity-weighted center of mass is used as (x, y)-predictor. Linear regressions should, on average, compensate for fluctuations from image slice to image slice.

6.1.2 Fluence determination in mixed fields

The FNTD lb1006 (placed just in front of the Bragg peak) monitors a mixed particle field of random angular distribution. It was read out according to the standard protocol of this study (cf. section 4.4) with both 8% and 100% relative laser power. A high p value will, on the one hand, improve the SNR (especially for low-LET fragments) but, on the other hand, maximize APD saturation for high-LET primaries, which hampers precise LET attribution. Table 6.1 compares obtained fluence results to treatment planning data. The spectrum (SPC) file contains full Monte Carlo simulated ion spectra for 79 depth steps ranging from 0 to 28.3 cm in water.

	$p = 8\%$	$p = 100\%$
Φ_V [$^1/_{\text{cm}^2}$]	$(4.1 \pm 0.2) \times 10^6$	$(5.2 \pm 0.02) \times 10^6$
Φ_{ref} [$^1/_{\text{cm}^2}$]	$(6.21 \pm 0.03) \times 10^6$	
agreement [%]	66 ± 3	83 ± 3

Table 6.1: *Fluence determination results for lb1006 based on automated image segmentation and trajectory reconstruction; high laser powers improve the SNR and yield an improved fluence agreement with the SPC*

Table 6.1 clearly demonstrates the positive impact of high SNRs on fluence determination accuracy. Nevertheless, the agreement for $p = 100\%$ with the reference fluence is below 95% obtained for multidirectional high-LET carbon ion fields in section 5.1.2. The most probable reason for this deviation is the large number of low-LET fragments with large relative energy loss straggling. Their intensity might even drop below background level in some image slices making them invisible to the image segmentation algorithm. This challenges reliable track reconstruction, since it demands particle identification in at least three consecutive image slices for trajectory reconstruction and extrapolation.

The level of fluence accuracy required for reliable dosimetry can be discussed considering the contribution of fragments and primary ions to the total absorbed dose. According to the ablation-abrasion-model, fragment velocities are comparable to the velocity of the disintegrated primary ion. But because of their lower charge, they will have a decreased LET (and thus longer range) and a smaller dose contribution compared to stopping primary ions. In other words, the high-LET particle fluence must be accurate, whereas the overall fluence is less important. The following calculation shall emphasize this argument:

> When neglecting all particles with LET in H_2O smaller than $1\,{}^{\mathrm{keV}}/_{\mathrm{\mu m}}$ in the SPC file, the total fluence in 13.15 cm water depth drops down to 65%, whereas the total absorbed dose remains at 98%.

Fragment and primary ion fluence can be quantified according to the track intensity histogram depicted in figure 6.2. The mean adjusted count rates are measured along single ion tracks and plotted against their frequency. One observes three peaks different in width and height. The minimum of the three superimposed Gaussian distributions sets the intensity threshold for ion type discrimination. All ion tracks with mean adjusted count rates smaller than 26.2 MHz are considered to be particles with charge $Z \leq 2$. The attribution of atomic number according to measured intensity requires previous knowledge on the ion beam and target material. If this is provided and a large number of tracks is investigated, this method is claimed to be suitable and accurate [44].

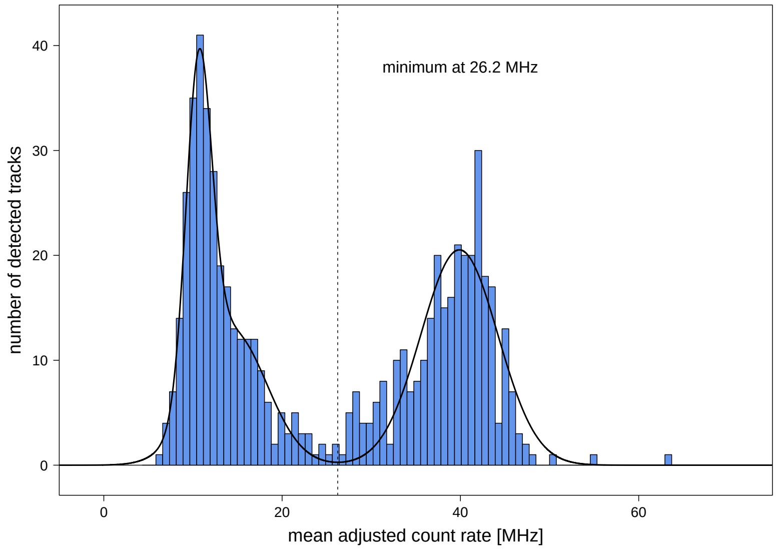

Figure 6.2: *Intensity histogram of lb1006 irradiated with 270 $^{\mathrm{MeV}}/_{\mathrm{u}}$ carbon ions at 13.1 cm water depth; adjusted count rates have been averaged along individual ion trajectories (624 in total); detected particles can be classified in low and high-LET subgroups; the minimum between the three superimposed Gaussian distributions lies at 26.2 MHz*

Particle fluence discrimination according to this criterion yields fluence estimates for different particle types. Table 6.2 indicates that nearly all high-LET trajectories are detected and reconstructed during image segmentation and analysis. Low-LET particles have a largely reduced fluence for detector readout at $p = 8\%$. By increasing the laser power, this value increases accordingly.

	$\eta_{adj} < \mathbf{26.2\,MHz}$	$\eta_{adj} > \mathbf{26.2\,MHz}$
Φ_V [1/cm²]	$(2.16 \pm 0.12) \times 10^6$	$(1.96 \pm 0.11) \times 10^6$
Φ_{ref} [1/cm²]	$(4.19 \pm 0.02) \times 10^6$	$(2.02 \pm 0.05) \times 10^6$
agreement [%]	52 ± 3	97 ± 5

Table 6.2: *Particle fluences of low and high-LET subgroups defined by the count rate histogram of figure 6.2; reference fluences are calculated from the corresponding SPC file with the following charge attribution: $\eta_{adj} < 26.2\,MHz \Leftrightarrow Z \leq 2$ and $\eta_{adj} > 26.2\,MHz \Leftrightarrow Z \geq 3$; detection and tracking efficiency for high-LET particles responsible for the major amount of deposited energy equal 100% within statistical uncertainty, whereas low-LET particle detection suffers from a small SNR*

6.2 Stopping Power Determination

The linear stopping power S (equivalent to LET for HCPs impinging FNTDs) is the second quantity of interest in fluence-based dosimetry. Conducted experiments yielded two calibration curves – one for conventional, one for background-reduced FNTDs – translating detected adjusted count rates directly into LET. Their accuracy is discussed and their applicability is tested in this section.

6.2.1 LET spectroscopy and APD saturation

Fluence-based dosimetry in heavy ion fields containing both high and low-LET particles was challenged by APD saturation. Section 6.1 showed that detector readout with high laser powers is essential for high SNRs and optimal fluence determination prerequisites. Conventional FNTDs especially call for large p values, since their background level can be in the order of fast proton intensities. The reduced fluence ratio of 2:1 instead of 5:1 observed in figure 5.4 emphasizes this conclusion. On the other hand, achieving high SNRs even for low-LET particles inevitably results in large saturation of high-LET track intensities. And because of the exponential form of the saturation function, adjusted count rates will have poor accuracy after saturation correction. But precise knowledge of their LET is essential for reliable dosimetry as they contribute most to the total energy deposition. Thus, the trade-off between high tracking efficiency and low APD saturation needs to be optimized for each irradiated detector. A dedicated FNTD reader developed by Landauer Inc. allows for APD operation in current mode, thus avoiding saturation effects. This could improve both fluence and absolute LET determination.

6.2.2 Inverse LET calibration curve

Established LET calibration curves must be inverted to calculate energy loss from adjusted count rates. Their logarithmic form yields:

$$L = 10^{(\eta_{adj}-c)/a} - b. \tag{6.1}$$

The fit parameters a, b and c for conventional and background-reduced FNTDs are stated in equations 5.2 and 5.3, respectively. The goodness of such an inverse calibration curve can be expressed in terms of confidence bands. They are calculated following the delta method elucidated in section 3.7. Figure 6.3 shows the result of inversion. An expected broadening of the confidence interval (CI) outside of the measurement range (1.5 – 150 $^{\mathrm{keV}}/_{\mu\mathrm{m}}$) is observed.

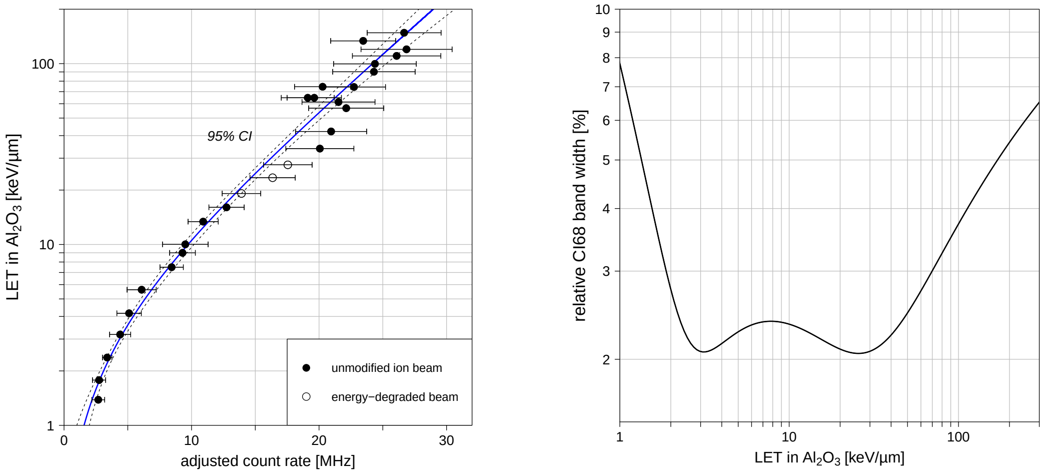

Figure 6.3: *Inverse LET calibration curve for background-reduced FNTDs showing 95% confidence bands around the interpolating fit line (left); relative 68% confidence interval width (measure for the standard fit error) plotted over LET (right); calculation according to the delta method accounting for uncertainties in measured adjusted count rates*

For background-reduced FNTDs, sensitivity-related fluctuations have the largest impact on measured count rates. The calculated relative 68% confidence interval is below 5%, when measuring approximately 3,600 tracks of the same LET distributed over three different detectors and four different readout areas per detector. Thus, the confidence bands represent the goodness of the logarithmic fit but they cannot function as error estimates for LET determination based on count rate measurements along single trajectories.

6.2.3 LET uncertainty budget

LET determination in mixed particle fields faces few but strong accuracy limiting factors. They are ordered by decreasing impact:

- Analysis of the background-reduced detector set showed intra-detector intensity variabilities of $(4.2 \pm 0.2)\%$ on average. Sensitivity fluctuations between different FNTDs resulted in even larger intensity variabilities: $(18.7 \pm 1.8)\%$ on average. In order to apply the calibration function on single count rate measurements, they have to be corrected for the local detector sensitivity. Two possible approaches are suggested in section 6.4.
- The influence of APD saturation on LET determination has already been discussed in section 6.2.1. It is unavoidable in mixed heavy ion fields, where tracks with a high LET could already be saturated to a large degree while low-LET particles might not even be visible in each image slice. APD operation in current mode would solve this issue.
- The influence of ϑ on η_{adj} characterized in section 5.2.3 calls for more robust intensity measures. Single maximum pixel values are no longer sufficient to describe the local energy deposition. Quantities such as integral areal or volumetric intensity might yield improvements. However, this source of uncertainty is considered to have the smallest impact, since most angular offsets from primary beam direction are well below 30° in clinical carbon ion fields. Furthermore, only light fragments will show large ϑ values and their LET and dose contribution is low. Thus, polar angle intensity correction will scarcely influence the total measured absorbed dose.

6.2.4 LET determination in mixed fields

When analyzing the mixed particle field on lb1006, detected count rates were averaged along single ion trajectories and converted into LET according to equation 6.1. Prior correction for laser power nonlinearities was omitted, since they have not been investigated on the set of conventional FNTDs. The fluence-weighted LET (fLET) L_Φ for each subgroup is compared to the reference SPC values in table 6.3. It can be calculated from the measured particle fluence Φ_V, obtained LET values L_i and calculated tracks lengths ℓ_i in the readout volume V:

$$L_\Phi = \frac{1}{\Phi_V} \sum_{i=1}^{N} L_i \, \frac{\ell_i}{V}. \tag{6.2}$$

Detector sensitivity fluctuations can cause large, systematic intensity shifts, which directly translate into LET uncertainties. The relative residuals of the conventional calibration curve are $(3.9 \pm 1.0)\%$ on average. The errors on fLET in H_2O are estimated from this variability. In order to achieve reliable and comparable LET determination, it will be of particular interest to quantify the sensitivity of each FNTD and to correct measured count rates accordingly.

	$\eta_{adj} < 26.2\,\mathrm{MHz}$	$\eta_{adj} > 26.2\,\mathrm{MHz}$
L_Φ in H_2O [keV/µm]	3.57 ± 0.29	30.3 ± 3.2
$L_{\Phi,ref}$ in H_2O [keV/µm]	1.66 ± 0.05	35.6 ± 3.2
agreement [%]	215 ± 17	85 ± 9

Table 6.3: *Fluence-weighted LETs of low and high count rate subgroups; stated errors are estimated from systematic intensity variabilities of 3.9%; $L_{\Phi,ref}$ is calculated from the corresponding SPC file with the same charge attribution used for table 6.2; stated errors result from detector positioning uncertainties; fluence-weighted LET for protons and helium ions is largely overestimated; sensitivity fluctuations have a significant impact on measurement accuracy*

The analyzed detector showed a mean background count rate of 4.3 MHz, which could partly be increased due to the high particle fluence. The background intensities of all investigated conventional FNTDs lie at (2.4 ± 0.8) MHz. Thus, it is reasonable to assume a slightly increased sensitivity. Table 6.3 suggests that low-LET particles could be affected stronger by sensitivity fluctuations than high-LET ions, since their fluence-weighted LET is largely overestimated.

6.3 Energy Loss Straggling

6.3.1 Comparison to calculation

Energy loss calculations according to Landau and Vavilov distributions show a decrease in relative energy loss straggling with increasing LET. Furthermore, they suggest that particles with the same LET can have a different straggling behavior according to their atomic number Z. This effect can be seen in figure 6.4. Ion type and energy were chosen according to the irradiation parameters summarized in table 4.6. In the Landau regime, relative energy loss straggling remains constant with increasing LET as long as the ion type is unaltered. But a jump in Z leads to a large jump in relative energy loss straggling. However, the relative intensity straggling of 4.2 keV/µm protons and 5.6 keV/µm helium ions does not show such a wide gap (cf. figure 5.10).

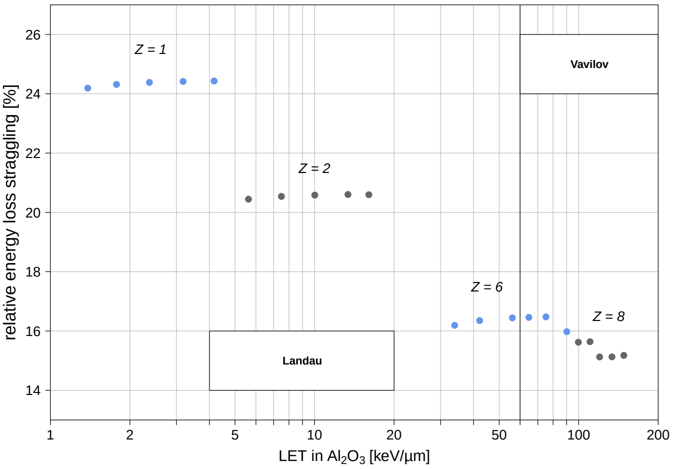

Figure 6.4: *Calculated energy loss distributions in 1 µm thin Al_2O_3 slices according to Landau and Vavilov distributions; $\sigma(S)/S$ decreases with increasing LET; particles with the same LET can have a very different straggling behavior according to their atomic number*

The dependency of energy loss straggling on particle type was not observed when measuring $\sigma_{rel}(\eta_{adj})$ on 31 different detectors. Reason for this might be the small axial thickness of microscope image slices below 1 µm. Although the κ value defined in equation 2.15 is within the demanded range, the number of collisions with low energy transfer N^{Δ}_{coll} is below 50 for all analyzed samples. Thus, ionization processes and secondary electron production have a significant contribution to the energy loss distribution and must be considered in the calculation. This could be achieved when simulating energy loss distributions in GEANT using the Urbán model.

6.3.2 Energy loss straggling and LET

The relative intensity straggling appears to be independent from detector sensitivity fluctuations, since data points obtained from conventional and background-reduced FNTDs fall on the same hyperbolic curve in figure 5.11. It might additionally be robust against small angular offsets. These findings suggest to determine LET from $\sigma_{rel}(\eta_{adj})$ rather than converting sensitivity-influenced count rates. However, calculated confidence intervals of the inverse curve drastically increase for $\sigma_{rel}(\eta_{adj}) < 15\%$, because straggling levels off[1] with increasing LET. This means that only $L_{Al_2O_3}$ values below 10 keV/µm can be accessed reliably via this method. Figure 6.5 depicts this circumstance. An approach to combine LET calibration with energy loss straggling to account for sensitivity fluctuations is sketched out in section 6.4.1.

---

[1] The asymptotic limit could be determined by photon detection noise. All z-stacks were read out at $\eta_{adj} \sim 2.5\,\text{MHz}$ (variable laser power) yielding $(90 \pm \sqrt{90})$ counts. The relative error (10.5%) is comparable to the fit parameter $\alpha = (13.4 \pm 0.1)\%$ of equation 5.4.

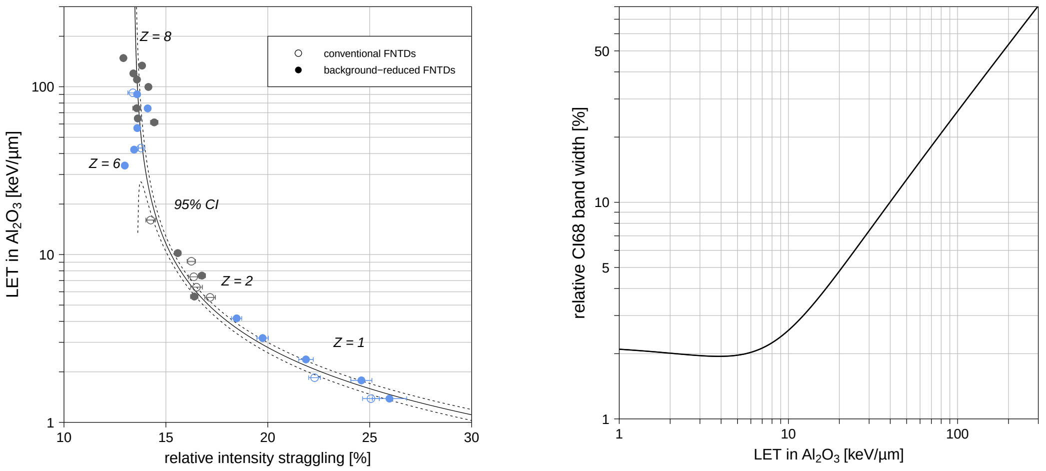

Figure 6.5: *Inverse relative intensity straggling for both conventional and background-reduced FNTDs showing 95% confidence bands around the interpolating fit line (left); relative 68% confidence interval width (measure for the standard fit error) plotted over LET (right); calculation according to the delta method accounting for uncertainties in intensity straggling; relative CI increases drastically for $\sigma_{rel}(\eta_{adj}) < 15\%$, which corresponds to $L_{Al_2O_3} > 10\,{}^{keV}/_{\mu m}$*

6.3.3 Energy loss straggling uncertainty budget

Uncertainties concerning energy loss straggling measurements in mixed particle fields are discussed in the order of decreasing impact:

- Information on energy loss straggling are blurred if APD saturation is high. Saturated tracks will always show decreased intensity straggling, which no longer represents the stochastic nature of energy deposition. Thus, all analyzed FNTDs have been read out with different laser powers p assuring comparable count rates around 2.5 MHz on raw microscope images. Such settings cannot be granted in the case of mixed particle fields, where an optimal trade-off between tracking efficiency and minimized saturation needs to be found. Thus, only the subgroup of low-LET particles will show unaffected intensity straggling.

- Furthermore, the polar angle ϑ changes straggling properties, since it decreases track intensities. Additionally, part of the large angle tracks will not be visible in all image slices in the stack (they exit the readout volume on one of its sides). Their relative straggling can, therefore, not be compared to straggling along orthogonal trajectories visible throughout the entire image stack.

- Energy loss straggling along single ion tracks is quantified in terms of relative intensity fluctuations $\sigma_{rel}(\eta_{adj}) = \sigma(\eta_{adj})/\mu(\eta_{adj})$. The uncertainty on $\sigma_{rel}(\eta_{adj})$ is much larger than the uncertainty on $\mu(\eta_{adj})$ [49]. In mixed fields, it is inevitable to obtain reliable results for each individual ion track. Averaging over a large population of particles identical in LET is not possible. Figure 6.6 compares the relative uncertainties on mean adjusted count rate and relative intensity straggling for particles with $L_{Al_2O_3} = (3.0 \pm 0.6)\,{}^{\mathrm{keV}}\!/\!_{\mu\mathrm{m}}$.

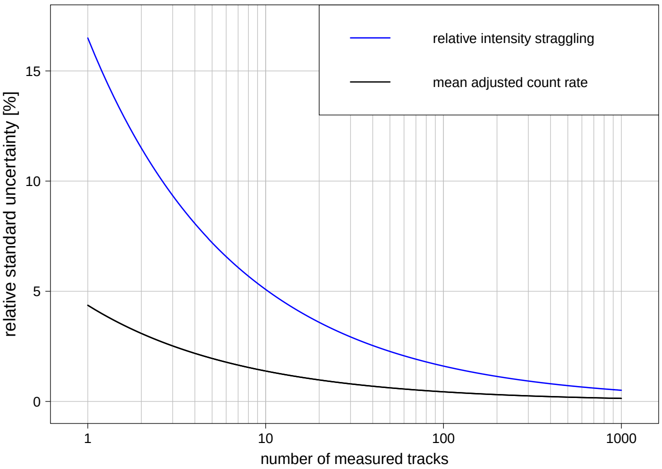

Figure 6.6: *Relative uncertainty comparison between $\sigma_{rel}(\eta_{adj})$ and $\mu(\eta_{adj})$ for $3\,{}^{keV}\!/\!_{\mu m}$ ions with an energy loss spread of 20%; measuring along a single trajectory (visible in 21 image slices) results in relative uncertainties of 4.4% for $\mu(\eta_{adj})$ and 16.5% for $\sigma_{rel}(\eta_{adj})$; averaging results over more than 100 tracks yields uncertainties well below 2% in both cases; calculation according to [49]*

6.4 Detector Sensitivity Quantification

Fluctuations in detector sensitivity cause the largest uncertainties in intensity measurements and hamper comparable, absolute LET assessment. Systematic errors of approximately 10% (cf. table 6.3) are not acceptable in clinical practice. Thus, it is of particular importance to quantify these fluctuations. The calculation of a sensitivity correction factor f_s would, then, allow for scaling detected count rates η_{adj}^{det} and translating the resulting values directly into LET using the inverse calibration function η_{adj}^{-1}:

$$L = \eta_{adj}^{-1}\left(f_s\ \eta_{adj}^{det}\right). \tag{6.3}$$

This section proposes two different approaches to calculating f_s. The first one (6.4.1) exploits energy loss straggling, whereas the second one (6.4.2) uses local background information. Corresponding correction factors are denoted with f_s^{σ} and f_s^{bg}.

6.4.1 Energy loss straggling approach

As already observed in section 5.3.1, $\sigma_{rel}(\eta_{adj})$ is primarily governed by the stochastic energy deposition in each image slice and robust against sensitivity fluctuations. This quantity could, therefore, be used to correct adjusted count rates. This approach is demonstrated by the example of three FNTDs from different batches placed in the same monoenergetic oxygen ion field ($L_{Al_2O_3} = 61\,{}^{\mathrm{keV}}/\mathrm{\mu m}$). The left plot in figure 6.7 emphasizes the large differences in detected count rates. All three FNTDs seem to be less sensitive than the average background-reduced FNTD, since their mean count rates are below η_{adj}^{exp} predicted by the calibration curve.

The calculation of f_s^{σ} follows three simple steps: (1) Measured relative intensity straggling is converted into LET using the inverse of equation 5.4 for each detected track. (2) The mean LET of the particle field L^* is translated into a mean expected count rate $\mu(\eta_{adj}^*)$ using the LET calibration function of equation 5.3. (3) f_s^{σ} is determined by the ratio of $\mu(\eta_{adj}^*)$ to the mean detected count rate $\mu(\eta_{adj}^{det})$.

The right plot in figure 6.7 shows detected count rates after f_s^{σ} scaling. Sensitivity-related differences could be minimized and the mean corrected count rates agree within statistical straggling width. They are, however, significantly lower than the expected count rate for $L_{Al_2O_3} = 61\,{}^{\mathrm{keV}}/\mathrm{\mu m}$. This shift arises from the first step of f_s^{σ} calculation. The inverse straggling curve is unstable for $L_{Al_2O_3} > 10\,{}^{\mathrm{keV}}/\mathrm{\mu m}$ (cf. figure 6.5). Small changes in relative intensity straggling result in large differences in LET. Thus, the proposed method yields accurate results only if $\sigma_{rel}(\eta_{adj}) > 15\%$.

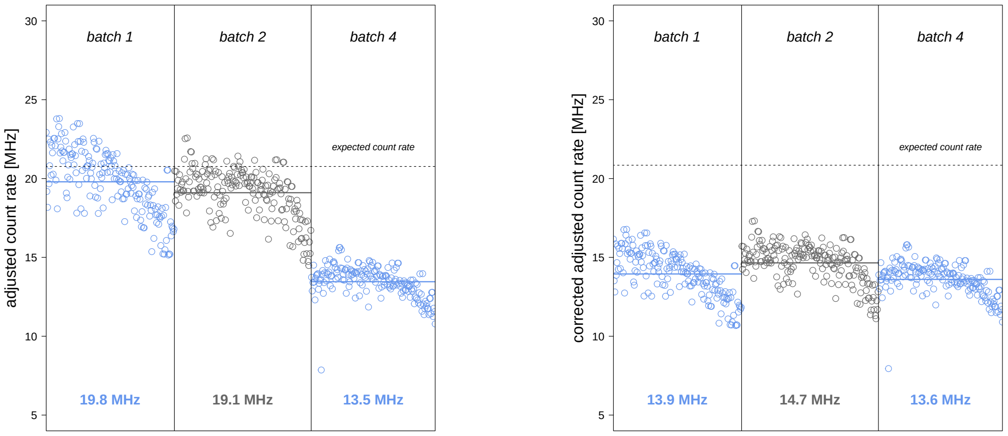

Figure 6.7: *Sensitivity correction based on energy loss straggling measurements for three FNTDs irradiated with a monoenergetic oxygen ion field ($L_{Al_2O_3} = 61\,{}^{\mathrm{keV}}/\mathrm{\mu m}$); detected count rates averaged along single ion tracks (left); count rates after correction with $f_{s,1}^{\sigma} = 0.75\ 0$, $f_{s,2}^{\sigma} = 0.77$ and $f_{s,4}^{\sigma} = 1.01$, respectively (right); uncertainties in the inverse straggling function yield a significant count rate shift equal for all three detectors*

6.4.2 Local background approach

A restriction on sensitivity correction towards larger count rates (or smaller intensity straggling) is unsatisfactory. The second approach is based on the determination of local background values B_i using the MOSAIC background subtractor (cf. section 3.4.2). f_s^{bg} is calculated individually for each ion track:

$$f_{s,i}^{bg} = \bar{B}/B_i \ . \tag{6.4}$$

Thus, it is also able to correct for the microscope flat field yielding decreased illumination at the outer image regions. The calculation requires knowledge on the overall mean detector background $\bar{B}$, which has been measured considering all 64 analyzed background-reduced FNTDs with a final result of $\bar{B} = (458.1 \pm 0.6)\,\mathrm{kHz}$.

Figure 6.8 (left) depicts measured background values B_i averaged along 21 image slices. The decreasing background intensity corresponds to decreasing detector sensitivity observed in figure 6.7. After applying background-based sensitivity correction, count rates on all three detectors have comparable means. Additionally, the influence of the microscope flat field appears to be eliminated in figure 6.8 (right).

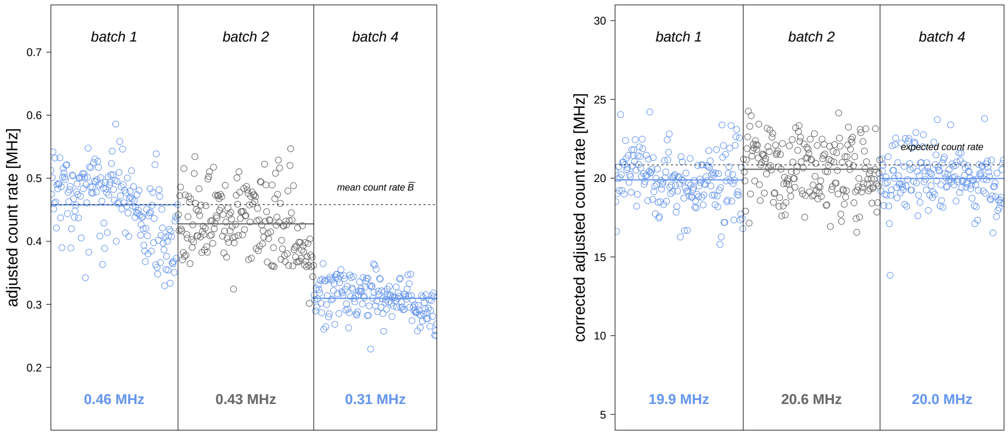

Figure 6.8: *Sensitivity correction based on local background measurements for three FNTDs irradiated with a monoenergetic oxygen ion field* ($L_{Al_2O_3} = 61\,\mathrm{keV}/\mu\mathrm{m}$)*; detected mean background averaged along single ion tracks (left); count rates show high agreement with* η_{adj}^{exp} *after correction with* f_s^{bg} *calculated individually for each ion track (right); influence of microscope flat field is reduced as well*

The presented approach does not show any restrictions on particle LET. However, it requires large signal-to-noise ratios in order to guarantee optimal background subtraction on microscope images. Furthermore, fluences larger than $5 \times 10^6\,1/\mathrm{cm}^2$ might influence the subtraction algorithm yielding falsely increased backgrounds. This assumption must be investigated more thoroughly in future studies.

6.5 Dose Calculation

Both approaches to sensitivity correction have been elaborated on background-reduced FNTDs. Since the Bragg peak irradiation was conducted on a conventional detector, measured LET values have not been corrected in this case. The fluence and LET results for the two subgroups ultimately allow for absorbed dose calculation. The full automated R script on dose assessment in mixed fields can be found in appendix D.5. Table 6.4 shows large agreements with the reference doses calculated from the corresponding SPC file. For the low-LET subgroup, poor tracking efficiency (cf. table 6.2) is compensated by an overestimation of fluence-weighted energy loss (cf. table 6.3).

	$\boldsymbol{\eta_{adj} < 26.2\,\mathrm{MHz}}$	$\boldsymbol{\eta_{adj} > 26.2\,\mathrm{MHz}}$
D [mGy]	$11.2 \pm 0.7 \pm 1.0$	$96.1 \pm 5.4 \pm 10.4$
D_{ref} [mGy]	11.1 ± 0.4	115 ± 10
agreement [%]	$101 \pm 6 \pm 9$	$83 \pm 5 \pm 9$

Table 6.4: *Absorbed dose of low and high-LET subgroups defined by the count rate histogram of figure 6.2; D_{ref} is calculated from the corresponding SPC file with the same charge attribution used for table 6.2; stated agreement errors originate from statistical fluence fluctuations and systematic sensitivity variabilities; both primary and fragment dose are in high agreement with the reference value; for the latter, poor tracking efficiency is compensated by LET overestimation*

Combining both results yields an overall dose agreement of

$$\begin{gathered}\boldsymbol{D/D_{ref} = (85 \pm 3 \pm 9)\,\%} \\ \text{with } D_{ref} = (126 \pm 11)\,\mathrm{mGy}.\end{gathered} \tag{6.5}$$

The high sensitivity-related uncertainty (9%) emphasizes the importance of further studies on the determination of f_s. Such a correction factor would allow for robust LET assessment with minimized inter-detector fluctuations. Apart from that, fluence and LET determination routines established within this study can successfully be applied to measure the dose deposited by mixed heavy ion fields.

7 CONCLUSION

The work presented in this thesis enables fluence and LET determination of complex, heterogeneous particle fields predominant in therapeutically decisive Bragg peak proximity using FNTDs. Furthermore, elaborated routines were successfully combined in a novel fluence-based dosimetry approach. Since FNTDs are biocompatible and autoclavable, they can record spectroscopic particle field information *in vivo*. Thus, findings of this thesis have potential relevance to the improvement of carbon ion therapy as they provide a significant advance towards the application of FNTDs as offline treatment verification tools.

Fluence assessment was realized by trajectory reconstruction through the crystal volume. Deviations from the chosen reference fluence are less than 5% for the multi-directional, high-LET carbon ion field. In contrast, only half of the light fragments predicted by the treatment planning system (TPS) could be outlined on the conventional FNTD lb1006 irradiated just in front of the Bragg peak. Although their contribution to the total absorbed dose is small (less than 10% in this case), an enhanced tracking efficiency for low-LET ions is still desirable. A dedicated FNTD reader with current-mode APDs could solve this issue. It would allow for maximizing the SNR and, thus, optimizing prerequisites for trajectory reconstruction.

LET assessment is hampered by APD saturation as well. Additionally, sensitivity-related track intensity variabilities (nearly 20% for background-reduced FNTDs) challenged reliable energy loss determination. Further studies on this accuracy limiting factor could be performed on the comprehensive set of 90 irradiated FNTDs. A novel method utilizing sensitivity-independent energy loss straggling information along individual ion trajectories to optimize robustness of LET determination was introduced within this thesis. Combining this method with a sensitivity correction factor would enable reliable conversion of track intensities into energy loss using the established LET calibration curve for background-reduced FNTDs.

The ultimate outcome of this study is an automated fluence-based dose assessment routine for mixed heavy ion fields. Without any *a priori* assumptions, the analysis of lb1006 showed an overall dose agreement of 85% with the TPS reference. This agreement is expected to be even larger for the analysis of background-reduced FNTDs, since LET determination could exploit the full potential of the novel calibration curve in that case. Furthermore, charge attribution according to the measured LET spectrum could be demonstrated for a single analyzed readout volume. Such attribution allows for estimating the biological effect of the deposited dose, which is inevitable for the future use of FNTDs in carbon ion therapy verification.

APPENDICES

A Lists

A.1 List of abbreviations

AFP	axial focus position
APD	avalanche photo diode
ASF	axial scaling factor
AU	airy unit
CBG	molecular cell biology and genetics
CI	confidence interval
CLSM	confocal laser scanning microscope
CSDA	continuous slowing down approximation
D	dimension
DIC	differential interference contrast
DKFZ	German Cancer Research Center
ETH	Swiss Federal Institute of Technology
fLET	fluence-weighted linear energy transfer
FNTD	fluorescent nuclear track detector
GEANT	geometry and tracking
HCP	heavy charged particle
HIT	Heidelberg Ion-Beam Therapy Center
ICRU	International Commission on Radiation Units and Measurements
LEM	local effect model
LET	linear energy transfer
LP	longpass
LSM	laser scanning microscope
MBS	multi-band beam splitter
MOSAIC	Models, Simulation and Algorithms for Interdisciplinary Computing
MPI	Max Planck Institute
NFP	nominal focus position
PMMA	poly(methyl methacrylate)
PMT	photomultiplier tube
PPL	portable pack for localization imaging
PSF	point spread function
QA	quality assurance
RBE	relative biological effectiveness
SNR	signal-to-noise ratio
SPC	spectrum
Squassh	segmentation and quantification of subcellular shapes

SRIM	The Stopping and Range of Ions in Matter
T-PMT	transmission photomultiplier tube
TPS	treatment planning system
XML	Extensible Markup Language
ZEN	Zeiss efficient navigation

A.2 List of figures

A.3 List of tables

B Radiochromic Films

B.1 Carbon ions under three angles

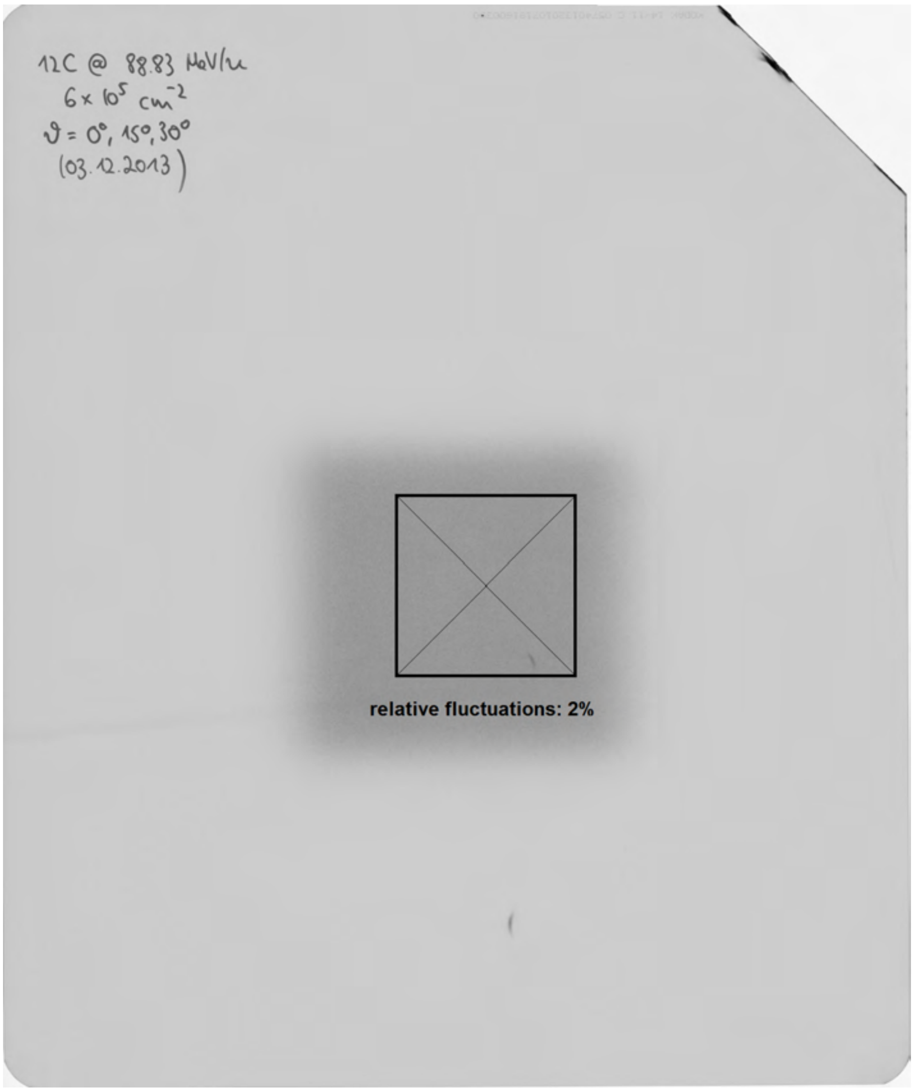

Figure B.1: *Radiochromic film (Kodak PPL) monitoring homogeneity of a* $5 \times 5\,cm^2$ *carbon ion field (black square); detector gk5007 was placed at isocenter (cross) and exposed to three sub-fields under three different polar angles* ($\vartheta = 0^\circ, 15^\circ, 30^\circ$) *accounting for a total particle fluence of* $\Phi = 0.6 \times 10^6\ {}^1\!/_{cm^2}$*; relative intensity fluctuations, which directly relate to fluence inhomogeneities, amount to 2%*

B.2 Helium ions under three angles

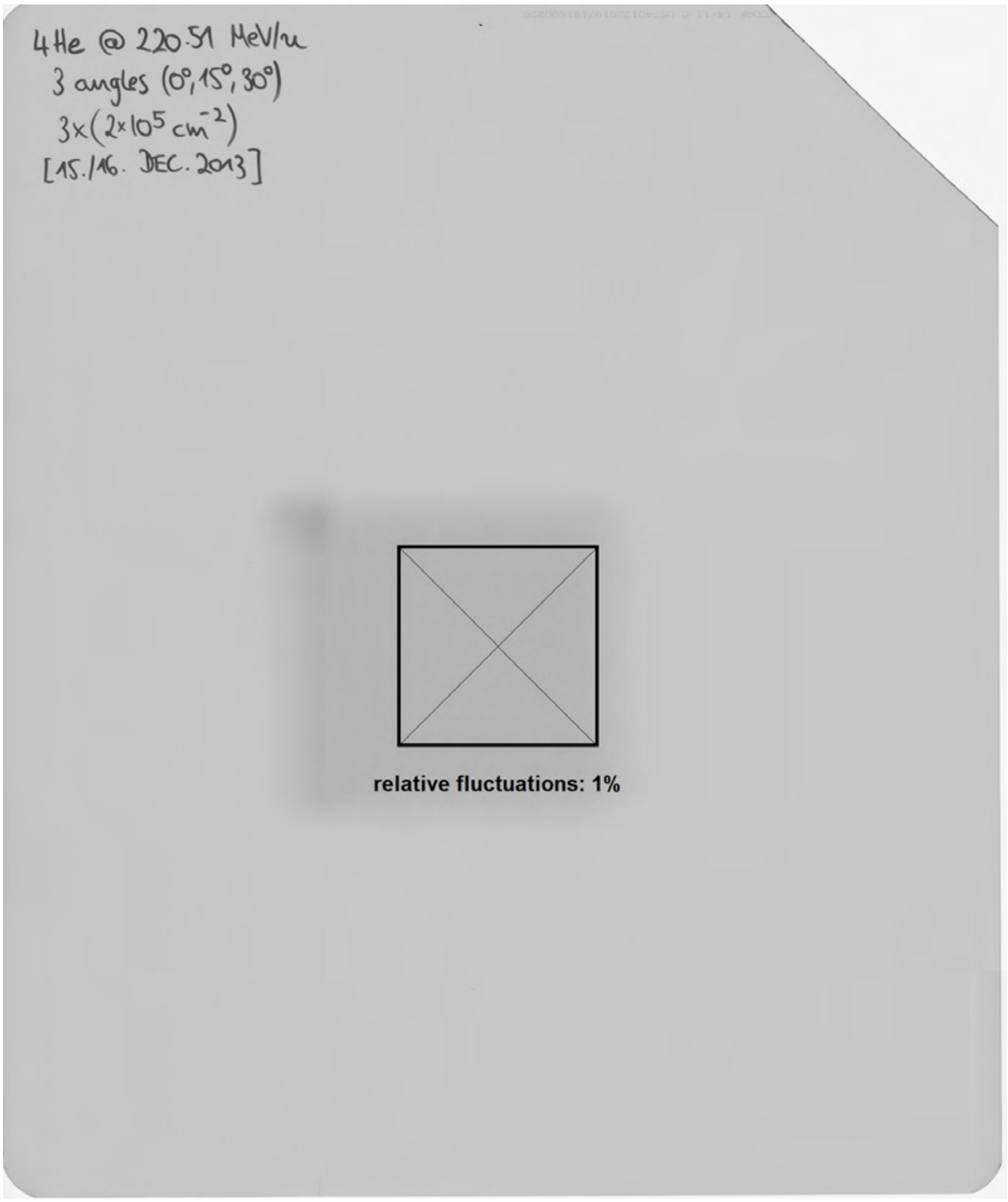

Figure B.2: *Radiochromic film (Kodak PPL) monitoring homogeneity of a* $5 \times 5\,cm^2$ *helium ion field (black square); detector gk5150 was placed at isocenter (cross) and exposed to three sub-fields under three different polar angles* ($\vartheta = 0°, 15°, 30°$) *accounting for a total particle fluence of* $\Phi = 0.6{\times}10^6\ {}^1/_{cm^2}$*; relative intensity fluctuations, which directly relate to fluence inhomogeneities, amount to 1%*

B.3 Carbon ions under six angles

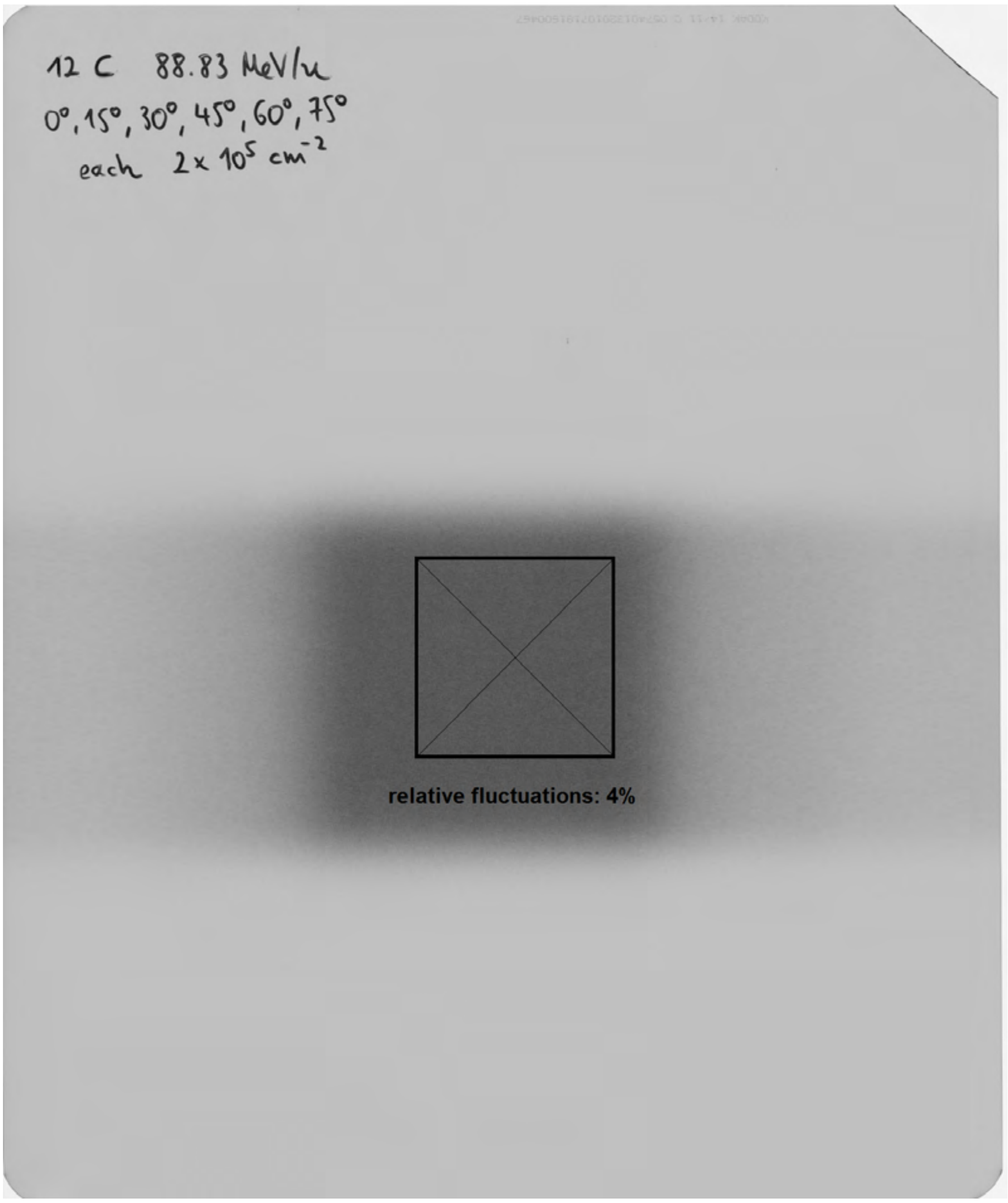

Figure B.3: *Radiochromic film (Kodak PPL) monitoring homogeneity of a* $5 \times 5\,cm^2$ *carbon ion field (black square); detectors gk5003, gk5004, gk5005 and gk5006 were placed at isocenter (cross) and exposed to six sub-fields under six different polar angles* ($\vartheta = 0°, 15°, 30°, 45°, 60°, 75°$) *accounting for a total particle fluence of* $\Phi = 1.2 \times 10^6\ {}^{1}/_{cm^2}$; *relative intensity fluctuations, which directly relate to fluence inhomogeneities, amount to 4%*

C Irradiation Tables

detector ID	**ion type**	**energy [MeV/u]**	**PMMA degradation**	**LET in Al_2O_3 [keV/µm]**	**fluence [1/cm²]**	**date of irradiation**
hm(1,2,4)101	^{1}H	221.06	—	1.39	2×10^6	05/05/2014
hm(1,2,4)102	^{1}H	150.41	—	1.78	2×10^6	05/05/2014
hm(1,2,4)103	^{1}H	100.46	—	2.37	2×10^6	05/05/2014
hm(1,2,4)104	^{1}H	68.08	—	3.18	2×10^6	05/05/2014
hm(1,2,4)105	^{1}H	48.12	—	4.17	2×10^6	05/05/2014
hm(1,2,4)106	^{4}He	216.70	—	5.62	2×10^6	05/05/2014
hm(1,2,4)107	^{4}He	140.14	—	7.49	2×10^6	05/05/2014
hm(1,2,4)108	^{4}He	108.61	—	8.99	2×10^6	08/01/2014
hm(1,2,4)109	^{4}He	93.51	—	10.02	2×10^6	05/05/2014
hm(1,2,4)110	^{4}He	63.93	—	13.38	2×10^6	08/01/2014
hm(1,2,4)111	^{4}He	50.57	—	16.05	2×10^6	08/01/2014
hm(1,2,4)130	^{4}He	220.51	1 cm	5.64 ± 0.01	2×10^6	05/05/2014
hm(1,2,4)131	^{4}He	115.93	1 cm	9.01 ± 0.03	2×10^6	05/05/2014
hm(1,2,4)132	^{4}He	55.30	1 cm	19.14 ± 0.18	2×10^6	08/01/2014
hm(1,2,4)133	^{4}He	61.86	2 cm	23.40 ± 0.29	2×10^6	08/01/2014
hm(1,2,4)134	^{4}He	58.65	2 cm	27.58 ± 0.40	2×10^6	08/01/2014

Table C.1: *Proton and helium ion irradiation parameters for the background-reduced LET calibration curve; three FNTDs indicated by the numbers in brackets were irradiated simultaneously with the same homogeneous and monoenergetic particle field ($5 \times 5\,cm^2$); stated $L_{Al_2O_3}$ values have been obtained from SRIM tables [43] and correspond to the energy-degraded beam*

detector ID	**ion type**	**energy [MeV/u]**	**PMMA degradation**	**LET in Al_2O_3 [keV/µm]**	**fluence [1/cm²]**	**date of irradiation**
hm(1,2,4)112	^{12}C	430.10	—	33.91	2×10^6	05/05/2014
hm(1,2,4)113	^{12}C	281.57	—	42.18	2×10^6	05/05/2014
hm(1,2,4)114	^{12}C	175.10	—	56.70	2×10^6	05/05/2014
hm(1,2,4)115	^{12}C	143.79	—	64.74	2×10^6	05/05/2014
hm(1,2,4)116	^{12}C	118.52	—	74.29	2×10^6	05/05/2014
hm(1,2,4)117	^{12}C	91.14	—	90.16	2×10^6	05/05/2014
hm(1,2,4)118	^{16}O	430.32	—	61.34	1×10^6	20/04/2014
hm(1,2,4)119	^{16}O	384.27	—	64.74	2×10^6	20/04/2014
hm(1,2,4)120	^{16}O	294.58	—	74.49	1×10^6	20/04/2014
hm(1,2,4)122	^{16}O	182.62	—	99.72	2×10^6	20/04/2014
hm(1,2,4)123	^{16}O	156.71	—	110.4	2×10^6	20/04/2014
hm(1,2,4)124	^{16}O	139.09	—	120.0	2×10^6	20/04/2014
hm(1,2,4)125	^{16}O	119.73	—	133.6	2×10^6	20/04/2014
hm(1,2,4)126	^{16}O	103.77	—	148.2	2×10^6	20/04/2014

Table C.2: *Carbon and oxygen ion irradiation parameters for the background-reduced LET calibration curve; three FNTDs indicated by the numbers in brackets were irradiated simultaneously with the same homogeneous and monoenergetic particle field ($5 \times 5\,cm^2$); stated $L_{Al_2O_3}$ values have been obtained from SRIM tables [43]; energy degradation was not required*

D Analysis Scripts (*.R)

D.1 Trajectory reconstruction

```
trajectory.info       <- function(df.total, image.size.um, x.min, x.max,
                                   y.min, y.max, z.min, z.max,
                                   max.rel.track.length.std) {

  ii                   <- unique(df.total$track.no)
  trajectory.info      <- matrix(nrow=length(ii), ncol=20)
  trajectory.info[,1]  <- ii

  for(n in ii) {

    df.tracks                <- subset(df.total, df.total$track.no==n)

    # 1. determine all possible linear fit functions from df.tracks

    x.of.z.fit           <- lm(formula = df.tracks$x ~ df.tracks$z)
    x.of.z.intercept     <- summary(x.of.z.fit)$coefficients[1,1]
    x.of.z.intercept.std <- summary(x.of.z.fit)$coefficients[1,2]
    x.of.z.slope         <- summary(x.of.z.fit)$coefficients[2,1]
    x.of.z.slope.std     <- summary(x.of.z.fit)$coefficients[2,2]
    x.of.z.fun           <- function(z) { x.of.z.intercept + x.of.z.slope * z }

    z.of.x.fit           <- lm(formula = df.tracks$z ~ df.tracks$x)
    z.of.x.intercept     <- summary(z.of.x.fit)$coefficients[1,1]
    z.of.x.intercept.std <- summary(z.of.x.fit)$coefficients[1,2]
    z.of.x.slope         <- summary(z.of.x.fit)$coefficients[2,1]
    z.of.x.slope.std     <- summary(z.of.x.fit)$coefficients[2,2]
    z.of.x.fun           <- function(x) { z.of.x.intercept + z.of.x.slope * x }

    y.of.z.fit           <- lm(formula = df.tracks$y ~ df.tracks$z)
    y.of.z.intercept     <- summary(y.of.z.fit)$coefficients[1,1]
    y.of.z.intercept.std <- summary(y.of.z.fit)$coefficients[1,2]
    y.of.z.slope         <- summary(y.of.z.fit)$coefficients[2,1]
    y.of.z.slope.std     <- summary(y.of.z.fit)$coefficients[2,2]
    y.of.z.fun           <- function(z) { y.of.z.intercept + y.of.z.slope * z }

    z.of.y.fit           <- lm(formula = df.tracks$z ~ df.tracks$y)
    z.of.y.intercept     <- summary(z.of.y.fit)$coefficients[1,1]
    z.of.y.intercept.std <- summary(z.of.y.fit)$coefficients[1,2]
    z.of.y.slope         <- summary(z.of.y.fit)$coefficients[2,1]
    z.of.y.slope.std     <- summary(z.of.y.fit)$coefficients[2,2]
    z.of.y.fun           <- function(y) { z.of.y.intercept + z.of.y.slope * y }
```

```
x.of.y.fit           <- lm(formula = df.tracks$x ~ df.tracks$y)
x.of.y.intercept     <- summary(x.of.y.fit)$coefficients[1,1]
x.of.y.intercept.std <- summary(x.of.y.fit)$coefficients[1,2]
x.of.y.slope         <- summary(x.of.y.fit)$coefficients[2,1]
x.of.y.slope.std     <- summary(x.of.y.fit)$coefficients[2,2]
x.of.y.fun           <- function(y) { x.of.y.intercept + x.of.y.slope * y }

y.of.x.fit           <- lm(formula = df.tracks$y ~ df.tracks$x)
y.of.x.intercept     <- summary(y.of.x.fit)$coefficients[1,1]
y.of.x.intercept.std <- summary(y.of.x.fit)$coefficients[1,2]
y.of.x.slope         <- summary(y.of.x.fit)$coefficients[2,1]
y.of.x.slope.std     <- summary(y.of.x.fit)$coefficients[2,2]
y.of.x.fun           <- function(x) { y.of.x.intercept + y.of.x.slope * x }


# 2. determine the track length inside readout volume

point1       <- c(x.min, 0,
                  y.of.x.fun(x.min),
                  sqrt(x.min^2*y.of.x.slope.std^2+y.of.x.intercept.std^2),
                  z.of.x.fun(x.min),
                  sqrt(x.min^2*z.of.x.slope.std^2+z.of.x.intercept.std^2))
point2       <- c(x.of.y.fun(y.min),
                  sqrt(y.min^2*x.of.y.slope.std^2+x.of.y.intercept.std^2),
                  y.min, 0,
                  z.of.y.fun(y.min),
                  sqrt(y.min^2*z.of.y.slope.std^2+z.of.y.intercept.std^2))
point3       <- c(x.of.z.fun(z.min),
                  sqrt(z.min^2*x.of.z.slope.std^2+x.of.z.intercept.std^2),
                  y.of.z.fun(z.min),
                  sqrt(z.min^2*y.of.z.slope.std^2+y.of.z.intercept.std^2),
                  z.min, 0)
point4       <- c(x.max, 0,
                  y.of.x.fun(x.max),
                  sqrt(x.max^2*y.of.x.slope.std^2+y.of.x.intercept.std^2),
                  z.of.x.fun(x.max),
                  sqrt(x.max^2*z.of.x.slope.std^2+z.of.x.intercept.std^2))
point5       <- c(x.of.y.fun(y.max),
                  sqrt(y.max^2*x.of.y.slope.std^2+x.of.y.intercept.std^2),
                  y.max, 0,
                  z.of.y.fun(y.max),
                  sqrt(y.max^2*z.of.y.slope.std^2+z.of.y.intercept.std^2))
point6       <- c(x.of.z.fun(z.max),
                  sqrt(z.max^2*x.of.z.slope.std^2+x.of.z.intercept.std^2),
                  y.of.z.fun(z.max),
                  sqrt(z.max^2*y.of.z.slope.std^2+y.of.z.intercept.std^2),
                  z.max, 0)

points.df           <- as.data.frame(rbind(point1, point2, point3,
                                           point4, point5, point6))
colnames(points.df) <- c("x", "x.std","y", "y.std", "z", "z.std")
```

```
points.df    <- points.df[ points.df$x >= 0     &
                           points.df$x <= image.size.um, ]
points.df    <- points.df[ points.df$y >= 0     &
                           points.df$y <= image.size.um, ]
points.df    <- points.df[ points.df$z >= z.min &
                           points.df$z <= z.max, ]

if(nrow(points.df)>2) {
  points.df <- points.df[-which(points.df ==
                         max(points.df[,c(2,4,6)]), arr.ind = TRUE)[1,1],]
}

if(nrow(points.df)>2) {
  points.df <- points.df[-which(points.df ==
                         max(points.df[,c(2,4,6)]), arr.ind = TRUE)[1,1],]
}

if(nrow(points.df)>2) {
  points.df <- points.df[-which(points.df ==
                         max(points.df[,c(2,4,6)]), arr.ind = TRUE)[1,1],]
}

if(nrow(points.df)>2) {
  points.df <- points.df[-which(points.df ==
                         max(points.df[,c(2,4,6)]), arr.ind = TRUE)[1,1],]
}

diff     <- c(points.df[1,]$x-points.df[2,]$x,
              points.df[1,]$y-points.df[2,]$y,
              points.df[1,]$z-points.df[2,]$z)
diff.std <- c(sqrt(points.df[1,]$x.std^2+points.df[2,]$x.std^2),
              sqrt(points.df[1,]$y.std^2+points.df[2,]$y.std^2),
              sqrt(points.df[1,]$z.std^2+points.df[2,]$z.std^2))

track.length     <- sqrt( sum(diff^2) )
track.length.std <- sqrt( (2*diff[1]*diff.std[1])^2 +
                          (2*diff[2]*diff.std[2])^2 +
                          (2*diff[3]*diff.std[3])^2 ) / track.length


# 3. determine polar and azimuthal angle [deg]

mean.x.of.z.intercept     <- ( x.of.z.intercept - z.of.x.intercept/
                               z.of.x.slope ) / 2
mean.x.of.z.intercept.std <- sqrt(x.of.z.intercept.std^2 +
                                  z.of.x.intercept.std^2/z.of.x.slope^2 +
                                  z.of.x.intercept^2*z.of.x.slope.std^2/
                                  z.of.x.slope^4) / 2
mean.x.of.z.slope         <- ( x.of.z.slope + (1/z.of.x.slope) ) / 2
mean.x.of.z.slope.std     <- sqrt(x.of.z.slope.std^2 +
                                  z.of.x.slope.std^2/z.of.x.slope^4) / 2
mean.x.of.z.fun           <- function(z) { mean.x.of.z.intercept +
```

```
                                           mean.x.of.z.slope * z }

mean.y.of.z.intercept     <- ( y.of.z.intercept - z.of.y.intercept/
                                 z.of.y.slope ) / 2
mean.y.of.z.intercept.std <- sqrt(y.of.z.intercept.std^2 +
                                    z.of.y.intercept.std^2/z.of.y.slope^2 +
                                    z.of.y.intercept^2*z.of.y.slope.std^2/
                                    z.of.y.slope^4) / 2
mean.y.of.z.slope         <- ( y.of.z.slope + (1/z.of.y.slope) ) / 2
mean.y.of.z.slope.std     <- sqrt(y.of.z.slope.std^2 +
                                    z.of.y.slope.std^2/z.of.y.slope^4) / 2
mean.y.of.z.fun           <- function(z) { mean.y.of.z.intercept +
                                           mean.y.of.z.slope * z }

cos.theta.out             <- 1 / sqrt(mean.x.of.z.slope^2 +
                                        mean.y.of.z.slope^2 + 1)
cos.theta.out.std         <- cos.theta.out^3 * sqrt(mean.x.of.z.slope^2 *
                                                      mean.x.of.z.slope.std^2 +
                                                      mean.y.of.z.slope^2 *
                                                      mean.y.of.z.slope.std^2)

if(mean.x.of.z.slope>0)
{ phi.deg.out <- atan( mean.y.of.z.slope / mean.x.of.z.slope ) * 180 / pi }
if(mean.x.of.z.slope==0)
{ phi.deg.out <- sign(mean.y.of.z.slope)*90 }
if(mean.x.of.z.slope<0 && mean.y.of.z.slope >= 0)
{ phi.deg.out <- atan(mean.y.of.z.slope/mean.x.of.z.slope)*180/pi+180 }
if(mean.x.of.z.slope<0 && mean.y.of.z.slope < 0)
{ phi.deg.out <- atan(mean.y.of.z.slope/mean.x.of.z.slope)*180/pi-180 }


# 4. return calculated information

trajectory.info[trajectory.info[,1]==n,2]   <- nrow(df.tracks)
trajectory.info[trajectory.info[,1]==n,3]   <- track.length
trajectory.info[trajectory.info[,1]==n,4]   <- track.length.std
trajectory.info[trajectory.info[,1]==n,5]   <- cos.theta.out
trajectory.info[trajectory.info[,1]==n,6]   <- cos.theta.out.std
trajectory.info[trajectory.info[,1]==n,7]   <- phi.deg.out
trajectory.info[trajectory.info[,1]==n,8]   <- NA
trajectory.info[trajectory.info[,1]==n,9]   <- points.df$x[1]
trajectory.info[trajectory.info[,1]==n,10]  <- points.df$x.std[1]
trajectory.info[trajectory.info[,1]==n,11]  <- points.df$y[1]
trajectory.info[trajectory.info[,1]==n,12]  <- points.df$y.std[1]
trajectory.info[trajectory.info[,1]==n,13]  <- points.df$z[1]
trajectory.info[trajectory.info[,1]==n,14]  <- points.df$z.std[1]
trajectory.info[trajectory.info[,1]==n,15]  <- points.df$x[2]
trajectory.info[trajectory.info[,1]==n,16]  <- points.df$x.std[2]
trajectory.info[trajectory.info[,1]==n,17]  <- points.df$y[2]
trajectory.info[trajectory.info[,1]==n,18]  <- points.df$y.std[2]
trajectory.info[trajectory.info[,1]==n,19]  <- points.df$z[2]
trajectory.info[trajectory.info[,1]==n,20]  <- points.df$z.std[2]
```

```
    trajectory.info[trajectory.info[,1]==n,]


    # 5. give status information

    cat("... done track", n, "out of", max(ii), "...\n")

  }

  trajectory.info               <- as.data.frame(trajectory.info)
  colnames(trajectory.info)     <- c("track.no", "length.slices", "length.um",
                                     "length.um.std", "cos.theta", "cos.theta.std",
                                     "phi.deg", "phi.deg.std", "x.in", "x.in.std",
                                     "y.in", "y.in.std","z.in", "z.in.std",
                                     "x.out", "x.out.std", "y.out", "y.out.std",
                                     "z.out", "z.out.std")
  trajectory.info$theta.deg     <- acos(trajectory.info$cos.theta) * 180 / pi
  trajectory.info$theta.deg.std <- trajectory.info$cos.theta.std /
                                   sqrt(1-trajectory.info$cos.theta^2)
  trajectory.info               <- trajectory.info[trajectory.info$length.um.std /
                                                   trajectory.info$length.um <
                                                   max.rel.track.length.std,]

  return(trajectory.info)

}
```

D.2 Trajectory filter function

```
trajectory.filter      <- function(df.trajectory, df.measured, no.slices) {

  # 1. determine the differences in track lengths, entrance and exit points

  results.list <- vector(mode="list", length=(nrow(df.trajectory)-1))

  for(n in 1:(nrow(df.trajectory)-1)) {

    results <- matrix(nrow=(nrow(df.trajectory)-n), ncol=20)
    for(m in (n+1):nrow(df.trajectory)) {

      diff.length     <- df.trajectory$length.um[n]-df.trajectory$length.um[m]
      diff.length.std <- sqrt(df.trajectory$length.um.std[n]^2 +
                              df.trajectory$length.um.std[m]^2)
      diff.theta      <- df.trajectory$cos.theta[n]-df.trajectory$cos.theta[m]
      diff.theta.std  <- sqrt(df.trajectory$cos.theta.std[n]^2 +
                              df.trajectory$cos.theta.std[m]^2)
      diff.x.in       <- df.trajectory$x.in[n]-df.trajectory$x.in[m]
      diff.x.in.std   <- sqrt(df.trajectory$x.in.std[n]^2 +
                              df.trajectory$x.in.std[m]^2)
      diff.y.in       <- df.trajectory$y.in[n]-df.trajectory$y.in[m]
```

```
    diff.y.in.std   <- sqrt(df.trajectory$y.in.std[n]^2 +
                            df.trajectory$y.in.std[m]^2)
    diff.z.in       <- df.trajectory$z.in[n]-df.trajectory$z.in[m]
    diff.z.in.std   <- sqrt(df.trajectory$z.in.std[n]^2 +
                            df.trajectory$z.in.std[m]^2)
    diff.x.out      <- df.trajectory$x.out[n]-df.trajectory$x.out[m]
    diff.x.out.std  <- sqrt(df.trajectory$x.out.std[n]^2 +
                            df.trajectory$x.out.std[m]^2)
    diff.y.out      <- df.trajectory$y.out[n]-df.trajectory$y.out[m]
    diff.y.out.std  <- sqrt(df.trajectory$y.out.std[n]^2 +
                            df.trajectory$y.out.std[m]^2)
    diff.z.out      <- df.trajectory$z.out[n]-df.trajectory$z.out[m]
    diff.z.out.std  <- sqrt(df.trajectory$z.out.std[n]^2 +
                            df.trajectory$z.out.std[m]^2)
    track.1         <- df.trajectory[n,]$track.no
    track.2         <- df.trajectory[m,]$track.no
    length.1        <- df.trajectory[n,]$length.slices
    length.2        <- df.trajectory[m,]$length.slices
    results[m-n,]   <- c(track.1, length.1, track.2, length.2, diff.length,
                         diff.length.std, diff.theta, diff.theta.std,
                         diff.x.in, diff.x.in.std, diff.y.in, diff.y.in.std,
                         diff.z.in, diff.z.in.std, diff.x.out, diff.x.out.std,
                         diff.y.out, diff.y.out.std, diff.z.out, diff.z.out.std)

  }
  results.list[[n]] <- results
  cat("... done track comparison", n, "out of", nrow(df.trajectory)-1, "...\n")
}

df.track.comparison            <- as.data.frame(do.call("rbind", results.list))
colnames(df.track.comparison)  <- c("track.1", "length.1", "track.2",
                                    "length.2", "diff.length", "diff.length.std",
                                    "diff.theta", "diff.theta.std", "diff.x.in",
                                    "diff.x.in.std", "diff.y.in", "diff.y.in.std",
                                    "diff.z.in", "diff.z.in.std", "diff.x.out",
                                    "diff.x.out.std", "diff.y.out",
                                    "diff.y.out.std", "diff.z.out",
                                    "diff.z.out.std")
df.track.comparison$length.sum <- df.track.comparison$length.1 +
                                  df.track.comparison$length.2
df.track.comparison            <- df.track.comparison
                                  [df.track.comparison$length.sum<=no.slices,]


# 2. filter out track pairs that are visible in the same slice

filter <- vector(mode="list", length=nrow(df.track.comparison))
for(n in 1:nrow(df.track.comparison)) {

  slices.1 <- df.measured[df.measured$track.no==
                          df.track.comparison[n,]$track.1,]$slice.no
  slices.2 <- df.measured[df.measured$track.no==
```

```
                          df.track.comparison[n,]$track.2,]$slice.no
  if(length(intersect(slices.1,slices.2))==0) {
    filter[[n]] <- TRUE
  } else {
    filter[[n]] <- FALSE
  }
}
df.track.comparison <- df.track.comparison[as.logical(filter),]
cat("... done filter 1 out of 4 (visibility in same slice) ...\n")


# 3. filter out track pairs with significantly different track
#    lengths and polar angles

filter <- vector(mode="list", length=nrow(df.track.comparison))
for(n in 1:nrow(df.track.comparison)) {

  if( abs(df.track.comparison$diff.length[n]) <
      3 * df.track.comparison$diff.length.std[n] &&
      abs(df.track.comparison$diff.theta[n])  <
      3 * df.track.comparison$diff.theta.std[n] ) {
    filter[[n]] <- TRUE
  } else {
    filter[[n]] <- FALSE
  }
}
df.track.comparison <- df.track.comparison[as.logical(filter),]
cat("... done filter 2 out of 4 (track lengths and angles) ...\n")


# 4. filter out track pairs with significantly different slopes x(z) and y(z)

filter <- vector(mode="list", length=nrow(df.track.comparison))
for(n in 1:nrow(df.track.comparison)) {

  sub.track.1 <- df.measured[df.measured$track.no==
                             df.track.comparison[n,]$track.1,]
  sub.track.2 <- df.measured[df.measured$track.no==
                             df.track.comparison[n,]$track.2,]

  lin.fit.x.1 <- summary(lm(sub.track.1$x ~ sub.track.1$slice.no))$coefficients
  lin.fit.x.2 <- summary(lm(sub.track.2$x ~ sub.track.2$slice.no))$coefficients
  lin.fit.y.1 <- summary(lm(sub.track.1$y ~ sub.track.1$slice.no))$coefficients
  lin.fit.y.2 <- summary(lm(sub.track.2$y ~ sub.track.2$slice.no))$coefficients

  if( abs(lin.fit.x.1[2,1] - lin.fit.x.2[2,1]) <
      3 * sqrt(lin.fit.x.1[2,2]^2 + lin.fit.x.2[2,2]^2) &&
      abs(lin.fit.y.1[2,1] - lin.fit.y.2[2,1]) <
      3 * sqrt(lin.fit.y.1[2,2]^2 + lin.fit.y.2[2,2]^2) ) {
    filter[[n]] <- TRUE
  } else {
    filter[[n]] <- FALSE
```

```
    }

  }
  df.track.comparison <- df.track.comparison[as.logical(filter),]
  cat("... done filter 3 out of 4 (regression line slopes) ...\n")


  # 5. filter out track pairs with significantly different x,y positions

  filter <- vector(mode="list", length=nrow(df.track.comparison))
  for(n in 1:nrow(df.track.comparison)) {

    sub.track.1 <- df.measured[df.measured$track.no==
                               df.track.comparison[n,]$track.1,]
    sub.track.2 <- df.measured[df.measured$track.no==
                               df.track.comparison[n,]$track.2,]

    if( abs(max(sub.track.1$slice.no) - min(sub.track.2$slice.no)) <
        abs(min(sub.track.1$slice.no) - max(sub.track.2$slice.no)) ) {

      last.x      <- sub.track.1$x[which.max(sub.track.1$slice.no)]
      last.y      <- sub.track.1$y[which.max(sub.track.1$slice.no)]
      last.slice  <- sub.track.1$slice.no[which.max(sub.track.1$slice.no)]
      first.x     <- sub.track.2$x[which.min(sub.track.2$slice.no)]
      first.y     <- sub.track.2$y[which.min(sub.track.2$slice.no)]
      first.slice <- sub.track.2$slice.no[which.min(sub.track.2$slice.no)]

      if( abs(last.x + mean(c(diff(sub.track.1$x),diff(sub.track.2$x))) *
          abs(last.slice-first.slice) - first.x) <
          3 * sd(c(diff(sub.track.1$x),diff(sub.track.2$x))) *
          abs(last.slice-first.slice) &&
          abs(last.y + mean(c(diff(sub.track.1$y),diff(sub.track.2$y))) *
          abs(last.slice-first.slice) - first.y) <
          3 * sd(c(diff(sub.track.1$y),diff(sub.track.2$y))) *
          abs(last.slice-first.slice) ) {
        filter[[n]] <- TRUE
      } else {
        filter[[n]] <- FALSE
      }

    } else {

      last.x      <- sub.track.1$x[which.min(sub.track.1$slice.no)]
      last.y      <- sub.track.1$y[which.min(sub.track.1$slice.no)]
      last.slice  <- sub.track.1$slice.no[which.min(sub.track.1$slice.no)]
      first.x     <- sub.track.2$x[which.max(sub.track.2$slice.no)]
      first.y     <- sub.track.2$y[which.max(sub.track.2$slice.no)]
      first.slice <- sub.track.2$slice.no[which.max(sub.track.2$slice.no)]

      if( abs(last.x + mean(c(diff(sub.track.1$x),diff(sub.track.2$x))) *
          abs(last.slice-first.slice) - first.x) <
          3 * sd(c(diff(sub.track.1$x),diff(sub.track.2$x))) *
```

```
          abs(last.slice-first.slice) &&
          abs(last.y + mean(c(diff(sub.track.1$y),diff(sub.track.2$y))) *
          abs(last.slice-first.slice) - first.y) <
          3 * sd(c(diff(sub.track.1$y),diff(sub.track.2$y))) *
          abs(last.slice-first.slice) ) {
        filter[[n]] <- TRUE
      } else {
        filter[[n]] <- FALSE
      }

    }

  }
  df.track.comparison <- df.track.comparison[as.logical(filter),]
  cat("... done filter 4 out of 4 (x,y positions) ...\n")

  return(df.track.comparison)

}
```

D.3 Track spot reconstruction

```
track.spot.reconstruction      <- function(df.trajectory, z.um, no.slices) {

  slices <- c(1:no.slices)
  df     <- vector(mode="list", length=nrow(df.trajectory))

  for(n in 1:nrow(df.trajectory)) {

    z.in  <- df.trajectory[n,]$z.in
    z.out <- df.trajectory[n,]$z.out

    if(length(z.um[z.um==z.in])==1 && length(z.um[z.um==z.out])==1) {
      z.first <- z.in
      z.last  <- z.out
    } else if(length(z.um[z.um==z.in])==1 && length(z.um[z.um==z.out])==0) {
      z.first <- z.in
      z.last  <- z.um[which(order(c(z.um,z.out))==(length(z.um)+1))-1]
    } else if(length(z.um[z.um==z.in])==0 && length(z.um[z.um==z.out])==1) {
      z.first <- z.um[which(order(c(z.um,z.in))==(length(z.um)+1))]
      z.last  <- z.out
    } else if(length(z.um[z.um==z.in])==0 && length(z.um[z.um==z.out])==0) {
      z.first <- z.um[which(order(c(z.um,z.in))==(length(z.um)+1))]
      z.last  <- z.um[which(order(c(z.um,z.out))==(length(z.um)+1))-1]
    }

    if(z.first<z.last) {
      depths   <- z.um[z.um>=z.first & z.um<=z.last]
      slice.no <- slices[z.um>=z.first & z.um<=z.last]
      steps    <- c(0:(length(depths)-1))*diff(z.um)[1]
      theta    <- df.trajectory[n,]$theta.deg*pi/180
```

```
      phi      <- df.trajectory[n,]$phi.deg*pi/180
      offset   <- (z.first-z.in)/cos(theta)
      x.first  <- df.trajectory[n,]$x.in + offset * sin(theta) * cos(phi)
      y.first  <- df.trajectory[n,]$y.in + offset * sin(theta) * sin(phi)
      z.seq    <- z.first + steps
    } else {
      depths   <- z.um[z.um>=z.last & z.um<=z.first]
      slice.no <- slices[z.um>=z.last & z.um<=z.first]
      steps    <- c(0:(length(depths)-1))*diff(z.um)[1]
      theta    <- df.trajectory[n,]$theta.deg*pi/180
      phi      <- df.trajectory[n,]$phi.deg*pi/180
      offset   <- (z.first-z.in)/cos(theta)
      x.first  <- df.trajectory[n,]$x.out + offset * sin(theta) * cos(phi)
      y.first  <- df.trajectory[n,]$y.out + offset * sin(theta) * sin(phi)
      z.seq    <- z.last + steps
    }

    x.seq    <- x.first + steps * tan(theta) * cos(phi)
    y.seq    <- y.first + steps * tan(theta) * sin(phi)

    df[[n]]               <- as.data.frame(cbind(slice.no, x.seq, y.seq, z.seq))
    colnames(df[[n]])     <- c("slice.no", "x", "y", "z")
    df[[n]]$track.no      <- df.trajectory[n,]$track.no
    df[[n]]$cos.theta     <- df.trajectory[n,]$cos.theta
    df[[n]]$cos.theta.std <- df.trajectory[n,]$cos.theta.std

  }

  df.final <- do.call("rbind", df)
  return(df.final)

}
```

D.4 Delta method

```
CI.delta.function <- function(count.rate, no.data.points, fit, quantile) {

  deriv.fun <- deriv(x ~ 10^((y-c)/a)-b, c("y", "a", "b", "c"), func=T)

  h.vect    <- c( as.numeric(attr(deriv.fun(count.rate,
                                            summary(fit)$parameters[1,1],
                                            summary(fit)$parameters[2,1],
                                            summary(fit)$parameters[3,1]),
                                            "gradient")[1,2]),
                  as.numeric(attr(deriv.fun(count.rate,
                                            summary(fit)$parameters[1,1],
                                            summary(fit)$parameters[2,1],
                                            summary(fit)$parameters[3,1]),
                                            "gradient")[1,3]),
                  as.numeric(attr(deriv.fun(count.rate,
                                            summary(fit)$parameters[1,1],
```

```
                                                   summary(fit)$parameters[2,1],
                                                   summary(fit)$parameters[3,1]),
                                                   "gradient")[1,4]) )

  var       <- as.numeric( h.vect %*% vcov(fit) %*% h.vect )

  # 1 sigma: quantile = 0.682689492
  # 2 sigma: quantile = 0.954499736
  # 3 sigma: quantile = 0.997300204

  return(qt(quantile, no.data.points-nrow(summary(fit)$parameters)) * sqrt(var))

}
```

D.5 Dose calculation

```
######################################
######################################
###                                ###
###                                ###
###        DOSE CALCULATION        ###
###                                ###
###     for conventional FNTDs     ###
###  (lp correction not included)  ###
###                                ###
###                                ###
######################################
######################################



source("FNTD.Cube.Functions.R")
require(FNTD)
require(libamtrack)



####################
# input parameters #
####################

image.size.um   <- 134.95
image.size.px   <- 1280
image.cutoff.px <- 40
no.slices       <- 21
start.depth.um  <- 30
dz.um           <- 2
dwell.time.us   <- 40.34
laser.power     <- 0.08
end.depth.um    <- start.depth.um + (no.slices-1) * dz.um
px.in.um        <- image.size.um / image.size.px
```

```
detector.id     <- "lb1006"



###############
# input files #
###############

image.stack    <- "./APD stacks/lb1006_intensity_lp8.tif"
image.means    <- "./APD tables/lb1006_intensity_lp8.xls"
BG.stack       <- "./BG stack/lb1006_intensity_lp8.tif"
track.data     <- "./track data/lb1006_lp8.txt"



#############################
# measure track intensities #
#############################

df.tracks.temp            <- read.table(track.data, header=TRUE)
df.tracks.temp            <- df.tracks.temp[df.tracks.temp$x>image.cutoff.px &
                                         df.tracks.temp$x<(image.size.px-
                                                           image.cutoff.px),]
df.tracks.temp            <- df.tracks.temp[df.tracks.temp$y>image.cutoff.px &
                                         df.tracks.temp$y<(image.size.px-
                                                           image.cutoff.px),]

write.table(df.tracks.temp, "df.tracks.temp.txt")

image                     <- FNTD.read.image(image.stack)
image@tracks              <- FNTD.read.tracks("df.tracks.temp.txt")
df.measured.tracks        <- FNTD.measure.tracks(jimg=image, radius=5,
                                                 critical.distance=3,
                                                 do.Gaussian=FALSE)

image                     <- FNTD.read.image(BG.stack)
image@tracks              <- FNTD.read.tracks("df.tracks.temp.txt")
df.measured.backgrounds   <- FNTD.measure.tracks(jimg=image, radius=15,
                                                 critical.distance=3,
                                                 do.Gaussian=FALSE)

rm(image)
gc()



################################################
# combine background means and measured tracks #
################################################

df.measured.tracks$mean.bg         <- df.measured.backgrounds$mean
df.measured.tracks                 <- df.measured.tracks
```

```
                                    [df.measured.tracks$area>0,]
df.measured.tracks$max.corr        <- df.measured.tracks$max -
                                    df.measured.tracks$mean.bg
df.measured.tracks                 <- df.measured.tracks
                                    [order(df.measured.tracks$track.no,
                                     decreasing=FALSE),]
df.measured.tracks$x               <- df.measured.tracks$x * px.in.um
df.measured.tracks$y               <- df.measured.tracks$y * px.in.um
df.measured.tracks$z               <- (start.depth.um +
                                     (df.measured.tracks$slice.no-1)*dz.um)*1.20


###########################################
# select tracks through at least 3 slices #
###########################################

track.lengths                   <- as.numeric(tapply(df.measured.tracks$track.no,
                                                     df.measured.tracks$track.no,
                                                     length))
df.measured.tracks$track.length <- rep(track.lengths, track.lengths)
df.sub.measured.tracks          <- df.measured.tracks
                                   [df.measured.tracks$track.length>=3,]



########################
# intensity correction #
########################

# 1. read in mean image intensities in each stack

mean.image.int <- read.table(image.means, header=TRUE)$Mean
mean.image.int <- mean.image.int / max(mean.image.int)


# 2. apply intensity-depth correction for each detetcor

df.int.corr.measured.tracks <- df.sub.measured.tracks

for(n in 1:no.slices){
  #n<-2
  ii                                        <-
    df.int.corr.measured.tracks$slice.no == n
  df.int.corr.measured.tracks$max[ii]       <-
    df.int.corr.measured.tracks$max[ii] /
    (dwell.time.us * laser.power * mean.image.int[n])
  df.int.corr.measured.tracks$mean[ii]      <-
    df.int.corr.measured.tracks$mean[ii] /
    (dwell.time.us * laser.power * mean.image.int[n])
  df.int.corr.measured.tracks$max.corr[ii]  <-
    df.int.corr.measured.tracks$max.corr[ii] /
    (dwell.time.us * laser.power * mean.image.int[n])
```

```
  df.int.corr.measured.tracks$mean.bg[ii]      <-
    df.int.corr.measured.tracks$mean.bg[ii] /
    (dwell.time.us * laser.power * mean.image.int[n])
}



###################################
# analyze track behavior in depth #
###################################

df.res <- data.frame(

  track.no              = unique(df.int.corr.measured.tracks$track.no),

  mean.max.MHz          = tapply(df.int.corr.measured.tracks$max,
                                 df.int.corr.measured.tracks$track.no, mean),
  mean.max.bg.corr.MHz  = tapply(df.int.corr.measured.tracks$max.corr,
                                 df.int.corr.measured.tracks$track.no, mean),
  sd.max.bg.corr.MHz    = tapply(df.int.corr.measured.tracks$max.corr,
                                 df.int.corr.measured.tracks$track.no, sd)

)

df.res$sigma.rel <- 100 * df.res$sd.max.bg.corr.MHz / df.res$mean.max.bg.corr.MHz



##################################################
# trajectory reconstruction by linear regression #
##################################################

df.trajectory       <- trajectory.info(df.total      = df.int.corr.measured.tracks,
                                       image.size.um = image.size.um,
                                       x.min         = image.cutoff.px*px.in.um,
                                       x.max         = image.size.um -
                                                         image.cutoff.px*px.in.um,
                                       y.min         = image.cutoff.px*px.in.um,
                                       y.max         = image.size.um -
                                                         image.cutoff.px*px.in.um,
                                       z.min = min(df.int.corr.measured.tracks$z),
                                       z.max = max(df.int.corr.measured.tracks$z),
                                       max.rel.track.length.std = 0.5)

df.track.comparison <- trajectory.filter(df.trajectory = df.trajectory,
                                         df.measured   = df.measured.tracks,
                                         no.slices     = no.slices)

for(n in 1:nrow(df.track.comparison)){
  #n<-1
  if(df.track.comparison[n,]$length.1 >= df.track.comparison[n,]$length.2) {
    df.trajectory <- df.trajectory[df.trajectory$track.no!=
```

```
                                 df.track.comparison[n,]$track.2,]
  } else {
    df.trajectory <- df.trajectory[df.trajectory$track.no!=
                                 df.track.comparison[n,]$track.1,]
  }
}

df.res$track.length.um <- NA
df.res$cos.theta       <- NA

for(n in 1:nrow(df.trajectory)) {
  # n<-7
  track.no                                         <- df.trajectory$track.no[n]
  df.res[df.res$track.no==track.no,]$track.length.um <- df.trajectory$length.um[n]
  df.res[df.res$track.no==track.no,]$cos.theta       <- df.trajectory$cos.theta[n]
}

df.res               <- na.omit(df.res)
df.res$length.slices <- df.trajectory$length.slices



#####################################
# LET, fluence and dose calculation #
#####################################

# 1. fluence calculation

df.res$fluence.cm2    <- (1E8) * df.res$track.length.um /
                         ((image.size.um-2*image.cutoff.px*px.in.um)^2 *
                          dz.um * (no.slices-1) * 1.2)
fluence.cm2.out       <- sum(df.res$fluence.cm2)
fluence.cm2.error     <- fluence.cm2.out / sqrt(nrow(df.trajectory))
fluence.agreement     <- 100 * fluence.cm2.out / fluence.cm2



# 2. LET calculation

inv.fit                  <- function(y) { 10^((y+15.1245)/35.99146)-2.608206 }
df.res$LET.H2O.keV.um    <- inv.fit(df.res$mean.max.bg.corr.MHz)
df.res$fLET.H2O.keV.um   <- df.res$LET.H2O.keV.um * df.res$fluence.cm2 /
                            fluence.cm2.out


# 3. dose calculation

dose.phys.Gy.out         <- (1.602E-6) * sum(df.res$LET.H2O.keV.um *
                                             df.res$fluence.cm2) / 999.97
sigma.dose.fluence       <- (1.602E-6) * sum(df.res$fLET.H2O.keV.um) *
                            fluence.cm2.error / 999.97
# this step assumes intensity variabilities of 3.9% on average
```

```
sigma.dose.fLET          <- (1.602E-6) * mean(log(10)/41.80138 *
                            (df.res$LET.H2O.keV.um+3.951503) * 0.039 *
                             df.res$mean.max.MHz) * fluence.cm2.out / 999.97
```

E Acknowledgments

I would like to express my gratitude to Prof. Dr. Oliver Jäkel for giving me the opportunity to carry out my Master's thesis in the Department of Medical Physics in Radiation Oncology at the German Cancer Research Center and for providing a deep insight into the field of heavy ion therapy. Furthermore, I wish to thank Prof. Dr. Peter Bachert for being the referee of this thesis and the representative of the Department of Physics and Astronomy.

I wish to express my very great appreciation to the University of Heidelberg, the German Academic Exchange Service, the Particle Therapy Co-Operative Group and the German Cancer Research Center for their financial support concerning medical physics conferences in Mainz, Athens and Shanghai. Presenting research results to the particle therapy community would not have been possible without their generous sponsorship.

I am particularly grateful for the outstanding supervision and helpful guidance of Dr. Steffen Greilich. His incomparable commitment created more than just the necessary prerequisites for a successful thesis. Additionally, I would like to thank Henning Mescher for an excellent cooperation on LET investigations and the entire research group for fruitful discussions in a very pleasant working atmosphere.

My special thanks are extended to Dr. Mark S. Akselrod from Landauer Inc. for supplying me with FNTDs, to Dr. Felix Bestvater from the Light Microscopy Facility for plenty of readout time and to Dr. Stephan Brons from the Heidelberg Ion-Beam Therapy Center for technical support during generously provided beam time. Assistance on image segmentation and trajectory generation by Pietro Incardona from the MOSAIC Group at the Max Planck Institute of Molecular Cell Biology and Genetics was very helpful and is greatly appreciated.

Finally, I wish to thank my family and friends for their support and encouragement throughout my study.

F Bibliography

[1] M. Scholz. Heavy ion tumour therapy. *Nuclear Instruments and Methods in Physics Research Section B: Beam Interactions with Materials and Atoms*, 161–163:76–82, 2000. ISSN 0168-583X. doi: 10.1016/S0168-583X(99)00669-2. URL `http://www.sciencedirect.com/science/article/pii/S0168583X99006692`. (cited on page 1)

[2] International Atomic Energy Agency. *Relative Biological Effectiveness in Ion Beam Therapy.* Technical reports series. International Atomic Energy Agency, 2008. ISBN 9789201078070. URL `http://www-pub.iaea.org/books/IAEABooks/7682/Relative-Biological-Effectiveness-in-Ion-Beam-Therapy`. (cited on page 1)

[3] D. Schardt, T. Elsässer, and D. Schulz-Ertner. Heavy-ion tumor therapy: Physical and radiobiological benefits. *Reviews od Modern Physics*, 82:383–425, 2010. doi: 10.1103/RevModPhys.82.383. URL `http://link.aps.org/doi/10.1103/RevModPhys.82.383`. (cited on pages 1, 6, 9 and 10)

[4] G.M. Akselrod, M.S. Akselrod, E.R. Benton, and N. Yasuda. A novel Al_2O_3 fluorescent nuclear track detector for heavy charged particles and neutrons. *Nuclear Instruments and Methods in Physics Research Section B: Beam Interactions with Materials and Atoms*, 247(2):295–306, 2006. ISSN 0168-583X. doi: 10.1016/j.nimb.2006.01.056. URL `http://www.sciencedirect.com/science/article/pii/S0168583X06001315`. (cited on pages 1 and 13)

[5] G.J. Sykora, M.S. Akselrod, E.R. Benton, and N. Yasuda. Spectroscopic properties of novel fluorescent nuclear track detectors for high and low LET charged particles. *Radiation Measurements*, 43(2–6):422–426, 2008. ISSN 1350-4487. doi: 10.1016/j.radmeas.2007.11.009. URL `http://www.sciencedirect.com/science/article/pii/S135044870700457X`. (cited on pages 1, 15, 16, 28 and 47)

[6] M.S. Akselrod, R.C. Yoder, and G.M. Akselrod. Confocal fluorescent imaging of tracks from heavy charged particles utilising new Al_2O_3:C,Mg crystals. *Radiation Protection Dosimetry*, 119(1–4):357–362, 2006. doi: 10.1093/rpd/nci664. URL `http://rpd.oxfordjournals.org/content/119/1-4/357.abstract`. (cited on page 1)

[7] J.-M. Osinga, M.S. Akselrod, R. Herrmann, V. Hable, G. Dollinger, O. Jäkel, and S. Greilich. High-accuracy fluence determination in ion beams using fluorescent nuclear track detectors. *Radiation Measurements*, 56:294–298, 2013. ISSN 1350-4487. doi: 10.1016/j.radmeas.2013.01.035. URL `http://www.sciencedirect.com/science/article/pii/S1350448713000589`. (cited on pages 1 and 16)

[8] M. Niklas, C. Melzig, A. Abdollahi, J. Bartz, M.S. Akselrod, J. Debus, O. Jäkel, and S. Greilich. Spatial correlation between traversal and cellular response in ion radiotherapy – Towards single track spectroscopy. *Radiation Measurements*, 56:285–289, 2013. ISSN 1350-4487. doi: 10.1016/j.radmeas.2013.01.060. URL `http://www.sciencedirect.com/science/article/pii/S1350448713000838`. (cited on pages 1, 28, 47 and 52)

[9] International Commission on Radiation Units and Measurements. Fundamental quantities and units for ionizing radiation (revised) – ICRU report no. 85. *Journal of the ICRU*, 11(1):7–28, 2011. doi: 10.1093/jicru/ndr012. URL `http://jicru.oxfordjournals.org/content/11/1/NP.2.short`. (cited on pages 3 and 9)

[10] F.H. Attix. *Introduction to Radiological Physics and Radiation Dosimetry*. Wiley, 1986. ISBN 9780471011460. URL `http://eu.wiley.com/WileyCDA/WileyTitle/productCd-0471011460.html`. (cited on page 4)

[11] International Commission on Radiation Units and Measurements. *Stopping powers and ranges for protons and alpha particles – ICRU report no. 49*. International Commission on Radiation Units and Measurements, 1993. (cited on pages 4 and 5)

[12] R.D. Evans. *The atomic nucleus*. International series in pure and applied physics. McGraw-Hill, 1955. URL `https://archive.org/details/atomicnucleus032805mbp`. (cited on page 6)

[13] J.-J. Gaimard and K.-H. Schmidt. A reexamination of the abrasion-ablation model for the description of the nuclear fragmentation reaction. *Nuclear Physics A*, 531(3–4):709–745, 1991. ISSN 0375-9474. doi: 10.1016/0375-9474(91)90748-U. URL `http://www.sciencedirect.com/science/article/pii/037594749190748U`. (cited on page 6)

[14] A.J.J. Bos. Fundamentals of radiation dosimetry. *AIP Conference Proceedings*, 1345:5–23, 2011. doi: 10.1063/1.3576156. URL `http://scitation.aip.org/content/aip/proceeding/aipcp/10.1063/1.3576156`. (cited on pages 7 and 8)

[15] L. Papiez and J.J. Battista. Radiance and particle fluence. *Physics in Medicine and Biology*, 39(6):1053–1062, 1994. doi: 10.1088/0031-9155/39/6/011. URL `http://stacks.iop.org/0031-9155/39/i=6/a=011`. (cited on pages 7 and 8)

[16] L. Papiez and J.J. Battista. Relpy to the comment by de Gruijl. *Physics in Medicine and Biology*, 40(10):1732, 1995. doi: 10.1088/0031-9155/40/10/013. URL `http://stacks.iop.org/0031-9155/40/i=10/a=013`. (cited on page 7)

[17] W.K. Weyrather and G. Kraft. RBE of carbon ions: Experimental data and the strategy of RBE calculation for treatment planning. *Radiotherapy and Oncology*, 73, Supplement 2:161–169, 2004. ISSN 0167-8140. doi: 10.1016/S0167-8140(04)80041-0. URL `http://www.sciencedirect.com/science/article/pii/S0167814004800410`. (cited on page 10)

[18] R. Brun and F. Carminati. GEANT – Detector description and simulation tool. *CERN Programming Library Long Writeup*, W5013:267–274, 1993. URL `https://wwwasdoc.web.cern.ch/wwwasdoc/pdfdir/geant.pdf`. (cited on pages 10 and 11)

[19] M.S. Akselrod and G.J. Sykora. Fluorescent nuclear track detector technology – a new way to do passive solid state dosimetry. *Radiation Measurements*, 46(12):1671–1679, 2011. ISSN 1350-4487. doi: 10.1016/j.radmeas.2011.06.018. URL `http://www.sciencedirect.com/science/article/pii/S135044871100271X`. (cited on pages 14, 15 and 16)

[20] S. Sanyal and M.S. Akselrod. Anisotropy of optical absorption and fluorescence in Al_2O_3:C,Mg crystals. *Journal of Applied Physics*, 98(3):033518, 2005. doi: 10.1063/1.1999032. URL `http://scitation.aip.org/content/aip/journal/jap/98/3/10.1063/1.1999032`. (cited on page 14)

[21] H. Mescher. Evaluation of uncertainty in linear energy transfer calibration of Al_2O_3:C,Mg-based fluorescent nuclear track detectors. Bachelor's thesis, University of Heidelberg, 2014. URL `http://www.ub.uni-heidelberg.de/archiv/17370`. (cited on pages 14, 21, 39 and 48)

[22] S.E. Combs, O. Jäkel, T. Haberer, and J. Debus. Particle therapy at the Heidelberg Ion Therapy Center (HIT) – Integrated research-driven university-hospital-based radiation oncology service in Heidelberg, Germany. *Radiotherapy and Oncology*, 95(1):41–44, 2010. ISSN 0167-8140. doi: 10.1016/j.radonc.2010.02.016. URL `http://www.sciencedirect.com/science/article/pii/S016781401000109X`. (cited on page 17)

[23] S. Greilich and the libamtrack team. *libamtrack: Computational routines for proton and ion radiotherapy*, 2013. URL `http://libamtrack.dkfz.org`. R package version 0.5.5. (cited on page 17)

[24] Carl Zeiss Microscopy. *LSM 710 and ConfoCor 3 – Operating manual*, 2009. URL `http://www.hawaii.edu/himb/docs/Facilities/manual_lsm_710.pdf`. (cited on pages 17, 19 and 24)

[25] S. Greilich, J.-M. Osinga, M. Niklas, F.M. Lauer, G. Klimpki, F. Bestvater, J.A. Bartz, M.S. Akselrod, and O. Jäkel. Fluorescent nuclear track detectors as a tool for ion-beam therapy research. *Radiation Measurements*, 56:267–272, 2013. ISSN 1350-4487. doi: 10.1016/j.radmeas.2013.01.033. URL `http://www.sciencedirect.com/science/article/pii/S1350448713000565`. (cited on pages 17 and 23)

[26] Carl Zeiss Microscopy. IC^{2}S high performance objectives, 2010. URL `http://www.zeiss.com/sensitivity`. (cited on page 18)

[27] Carl Zeiss Microscopy. LSM 710 – The power of sensitivity, 2009. URL `http://www.zeiss.com/sensitivity`. (cited on page 18)

[28] B. Zhang, J. Zerubia, and J.-C. Olivo-Marin. Gaussian approximations of fluorescence microscope point-spread function models. *Applied Optics*, 46(10): 1819–1829, 2007. doi: 10.1364/AO.46.001819. URL `http://ao.osa.org/abstract.cfm?URI=ao-46-10-1819`. (cited on pages 19 and 50)

[29] S. Hell, G. Reiner, C. Cremer, and E.J.K. Stelzer. Aberrations in confocal fluorescence microscopy induced by mismatches in refractive index. *Journal of Microscopy*, 169(3):391–405, 1993. ISSN 1365-2818. doi: 10.1111/j.1365-2818.1993.tb03315.x. URL `http://onlinelibrary.wiley.com/doi/10.1111/j.1365-2818.1993.tb03315.x/abstract`. (cited on page 20)

[30] H.J. van Elburg, L.C. Kuypers, W.F. Decreamer, and J.J.J. Dirckx. Improved correction of axial geometrical distortion in index-mismatched fluorescent confocal microscopic images using high-aperture objective lenses. *Journal of Microscopy*, 228(1):45–54, 2007. ISSN 1365-2818. doi: 10.1111/j.1365-2818.2007.01822.x. URL `http://onlinelibrary.wiley.com/doi/10.1111/j.1365-2818.2007.01822.x/abstract`. (cited on page 20)

[31] S. Greilich, J.-M. Osinga, M. Niklas, F.M. Lauer, F. Bestvater, and O. Jäkel. Quantitative read-out of Al_2O_3:C,Mg-based fluorescent nuclear track detectors using a commercial confocal microscope. Instrumentation and Detectors (physics.ins-det), 2014. URL `http://arxiv.org/abs/1407.0986`. (cited on pages 21 and 40)

[32] W. Rasband. ImageJ – Image processing and analysis in Java, 2013. URL `http://imagej.nih.gov/ij`. Version 1.47. (cited on page 24)

[33] MOSAIC Group (MPI-CBG). MosaicSuite for ImageJ andFiji – Models, simulation and algorithms for interdisciplinary computing, 2013. URL `http://mosaic.mpi-cbg.de`. Version lines and rt. (cited on page 24)

[34] J. Cardinale. *Histogram-based background subtractor for ImageJ.* MOSAIC Group, 2008 (revised 2010). URL `http://mosaic.mpi-cbg.de/Downloads/BGS_manual.pdf`. (cited on page 24)

[35] G. Levy. ParticleTracker 2D and 3D, 2014. URL `http://mosaic.mpi-cbg.de/ParticleTracker`. (cited on page 24)

[36] I.F. Sbalzarini and P. Koumoutsakos. Feature point tracking and trajectory analysis for video imaging in cell biology. *Journal of Structural Biology*, 151(2): 182–195, 2005. ISSN 1047-8477. doi: 10.1016/j.jsb.2005.06.002. URL `http://www.sciencedirect.com/science/article/pii/S1047847705001267`. (cited on page 25)

[37] A. Rizk, G. Paul, P. Incardona, M. Bugarski, M. Mansouri, A. Niemann, U. Ziegler, P. Berger, and I.F. Sbalzarini. Segmentation and quantification of subcellular structures in fluorescence microscopy images using Squassh. *Nature protocols*, 9(3):586–596, 2014. doi: 10.1038/nprot.2014.037. URL `http://www.nature.com/nprot/journal/v9/n3/full/nprot.2014.037.html`. (cited on page 25)

[38] The R Foundation. The R project for statistical computing, 2013. URL `http://www.r-project.org`. Version 3.0.2. (cited on page 25)

[39] J.J. Allaire. RStudio: Integrated development environment for R, 2013. URL `http://www.rstudio.org`. Version 0.97 and later. (cited on page 25)

[40] S. Greilich and the FNTD group. *FNTD: FNTD related R routines*, 2013. URL `https://r-forge.r-project.org/projects/fntd`. R package version 0.5.3. (cited on page 25)

[41] S. Greilich and S. Stefanowicz. *HITXML: XML plan generator for HIT*, 2013. URL `https://r-forge.r-project.org/projects/hitxml`. R package version 0.7.0. (cited on page 26)

[42] D. Sarkar. *Lattice: Multivariate Data Visualization with R.* Springer, New York, 2008. URL `http://lmdvr.r-forge.r-project.org`. ISBN 978-0-387-75968-5. (cited on page 26)

[43] J.F. Ziegler, J.P Biersack, and M.D. Ziegler. SRIM – The stopping and range of ions in matter, 2013. URL `http://www.srim.org`. Version 2013.00. (cited on pages 26, ix and x)

[44] J.A. Bartz, S. Kodaira, M. Kurano, N. Yasuda, and M.S. Akselrod. High resolution charge spectroscopy of heavy ions with FNTD technology. *Nuclear Instruments and Methods in Physics Research Section B: Beam Interactions with Materials and Atoms*, 335:24–30, 2014. ISSN 0168-583X. doi: 10.1016/j.nimb.2014.05.019. URL `http://www.sciencedirect.com/science/article/pii/S0168583X1400562X`. (cited on pages 32, 50 and 58)

[45] W.H. Press, S.A. Teukolsky, W.T. Vetterling, and B.P. Flannery. *Numerical Recipes in C: The Art of Scientific Computing.* Cambridge University Press,

New York, NY, USA, 2 edition, 1992. ISBN 0-521-43108-5. URL `http://www2.units.it/ipl/students_area/imm2/files/Numerical_Recipes.pdf`. (cited on pages 32 and 33)

[46] Y.M. Bishop, R.J. Light, F. Mosteller, S.E. Fienberg, and P.W. Holland. *Discrete Multivariate Analysis: Theory and Practice.* Springer, 2007. ISBN 9780387728063. URL `http://www.springer.com/mathematics/probability/book/978-0-387-72805-6`. (cited on page 34)

[47] X. Jiang. *Estimation of effective concentrations from in vitro dose-response data using the log-logistic model.* PhD thesis, University of Heidelberg, 2013. (cited on page 34)

[48] L. Brachtendorf. Detection of protons and carbon ions with depth using Al_2O_3:C,Mg-based fluorescent nuclear track detectors. Bachelor's thesis, University of Heidelberg, 2013. URL `http://www.ub.uni-heidelberg.de/archiv/15693`. (cited on pages 38, 39 and 55)

[49] S. Ahn and F.A. Fessler. Standard errors of mean, variance, and standard deviation estimators. University of Michigan (EECS Department), 2003. URL `http://web.eecs.umich.edu/~fessler/papers/files/tr/stderr.pdf`. (cited on pages 64 and 65)

G Declaration

I hereby certify that I am the sole author of this thesis and that I have not used any sources or aids other than those cited.

Heidelberg, August 29, 2014 ....

Grischa M. Klimpki